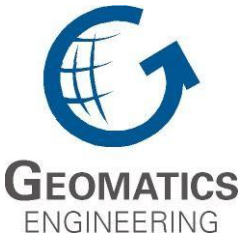

UCGE Reports
Number 20377

Department of Geomatics Engineering

Dynamic Structural Deflection Measurement with Range Cameras

(URL: http://www.geomatics.ucalgary.ca/graduatetheses)

by

Xiaojuan Qi

April, 2013

UNIVERSITY OF CALGARY

Dynamic Structural Deflection Measurement with Range Cameras

by

Xiaojuan Qi

A THESIS

SUBMITTED TO THE FACULTY OF GRADUATE STUDIES

IN PARTIAL FULFILLMENT OF THE REQUIREMENTS FOR THE

DEGREE OF MASTER OF SCIENCE

DEPARTMENT OF GEOMATICS ENGINEERING

CALGARY, ALBERTA

April, 2013

Abstract

Concrete beams are used to construct bridges and other structures. Years of traffic overloading and insufficient maintenance have left civil infrastructure such as bridges in a poor state of repair. Therefore, the structures have to be strengthened. Many options for the reinforcement exist such as fibre-reinforced polymer composites and steel plates can be added. The efficacy of such methods can be effectively evaluated through fatigue load testing in which cyclic loads are applied to an individual structural member under laboratory conditions. During the fatigue test, the deflection of concrete beam is very important parameter to evaluate the concrete beam. This testing requires the measurement of deflection in response to the applied loads. Many imaging techniques such as digital cameras, laser scanners and range cameras have been proven to be accurate and cost-effective methods for large-area measurement of deflection under static loading conditions. However, in order to obtain useful information about behaviour of the beams or monitoring real-time bridge deflection, the ability to measure deflection under dynamic loading conditions is also necessary. This thesis presents a relatively low-cost and high accuracy imaging technique to measure the deflection of concrete beams in response to dynamic loading with different range cameras such as time-of-flight range cameras and light coded range cameras.

Due to the time-of-flight measurement principle, even though target movement could lead to motion artefacts that degrade range measurement accuracy, the appropriate sampling frequency can be used to compensate the motion artefacts. The results of simulated and real-data investigation into the motion artefacts show that the lower sampling frequency results in the more significant motion artefact. The results from the data analysis of the deflection measurement derived from time-of-fight range cameras have been indicated that periodic deflection can be recovered with half-millimetre accuracy at 1 Hz and 3 Hz target motion. A preliminary analysis for light coded range cameras is conducted on dynamic

deflection measurement. The results demonstrate that the depth measurements of Kinect light coded range cameras are unstable, which implied that it is not sufficient to meet the accuracy required for the dynamic structural deflection measurement.

Acknowledgements

I would like to express my gratitude to my supervisor Dr. Derek Lichti who is an Associate Professor in Department of Geomatics Engineering, University of Calgary. This thesis would have never been accomplished without his generous support and his excellent supervision. During the study at University of Calgary, Dr. Lichti always provides valuable research guidance, enlightenment and encouragement to me. He is always patient to modify the same material over and over again. I really appreciate him for providing the Graduate Research Scholarship (Natural Sciences and Engineering Research Council of Canada and the Canada Foundation for Innovation fund).

I would like to appreciate Dr. Ayman Habib for his support for the dynamic structural deflection experiment. I really appreciate Dr. Mamdouh El-Badry (Department of Civil Engineering) for designing the structrual experiments and provided the laser displacement sensor data. I am also thankful to Mr. Dan Tilleman and other technicians for technical support during the two times dynamic structural deflection experiment.

I would like thank the group members of the Imaging Metrology Group, Sherif Halawany, Herve Lahamy, Kristian Morin, Ting On Chan, Jacky Chow, Kathleen Ang, Tanvir Ahmed and Jeremy to offer kind help for different expeiments such as range camera calibration and dynamic concrete beam experiment. It is my pleasure to thank Ivan Detchev and Sibel Canaz for helping me during my studies in Department of Geomatics Engineering.

At last, I would like to give my thanks to my husband Long Yu for his support and help.

Table of Contents

List of Tables

List of Figures and Illustrations

List of Symbols, Abbreviations and Nomenclature

Symbol	Definition
RC	Range camera
TOF-RC	Time-of-flight range camera
LC-RC	Light coded range camera
CCD	Charge-coupled device
CMOS	Complementary metal-oxide-semiconductor
TLS	Terrestrial laser scanner
FRP	Fibre-reinforced polymer
LDS	Laser displacement sensor
2D	Two dimensional
3D	Three dimensional
NAR	Non ambiguity range
MF	Modulation frequency
SF	Sampling frequency
IR	Infrared
TNC	The number of cycles

Chapter 1

Introduction

1.1 Motivation

Concrete beams are used to construct bridges and other structures. Due to traffic overloading or decaying state of structures, deflection occurs all the time. In addition, insufficient maintenance has left civil infrastructure such as bridges or other structures in a poor state of repair. In order to prevent bridge collapse and to strengthen the bridges, an accurate structure deflection monitoring system is desired. The requirement to measure deflection in concrete beams, as integral components of bridges and other of structures, has been well recognized. However, the deflection of the bridge varies because of different traffic loads. To effectively monitor the changing deflection, a dynamic imaging technique is necessary to measure an entire structure in situ. Accurate deflection measurements can be used to determine whether the bridges require rehabilitation. If the bridge deflection can be identified in its early stage and some effective methods can be used to strengthen the old bridges, disaster can be avoided.

Accurate concrete beam deflection measurement can be performed with different sensors such as dial gauges, linear-variable differential transformers and laser displacement sensors (LDSs). Maas and Hampel (2006) reported that these sensors provide high geometric precision, accuracy and reliability for measuring deflection. However, since they are point-wise devices, they can only measure the deflection in one dimension. Therefore, if two- or three-dimensional (3D) measurements are required, those sensors are not suitable. The range cameras (RCs) can provide dense point cloud of the entire surface, unlike the point based measurement system of the LDSs. The point cloud is a set of vertices in a three-dimensional coordinate system.

So far, the static deflection of structures has been measured by using traditional photogrammetric methods and terrestrial laser scanner (TLS) systems. In this thesis, the target object was subjected to periodic loads and its deflection was not static. However, TLS can only be used for static deflection measurement due to its sequential data collection. The traditional photogrammetric methods can measure dynamic deflection of structures. However, 3D point cloud reconstruction from different exposure locations is time consuming. In addition, several traditional digital cameras should be synchronized.

Three-dimensional RCs are a new generation of active cameras that provide range measurements by the time-of-flight principle or light coded principle. The reasons for using the range cameras for structural measurement are as follows:

First, RCs can perform video rate 3D measurement of entire surfaces of extended structures such as concrete beams. Second, RCs are much more compact in size so that they can be mounted easily when compared with TLS, which are rather more bulky and usually mounted on tripods. Third, the cost of RCs is about an order of magnitude lower than TLSs.

Therefore, based on the advantages of RCs, this thesis focuses on using 3D range cameras to monitor dynamic deflection of a concrete beam subjected to periodic loads in a laboratory, which is basically a simulation of the traffic loads for bridges.

1.2 Background

Three-dimensional range imaging camera systems, which are active sensors have been recently developed for close range photogrammetric applications, and can be classified into two categories: time-of-flight range cameras (TOF-RCs) and light coded range cameras (LC-RCs).

1.2.1 Introduction to time-of-flight range cameras

The continuous-wave modulation of near-infrared light is the active light source for TOF-RCs. By calculating phase difference between emitted and reflected signals, ranges between a camera and a target object can be derived. A two-dimensional (2D) array of lock-in pixels (Lange and Seitz, 2001) in a charge-coupled device is used to detect and demodulate the reflected light. Each pixel determines the distance and amplitude information of the illuminated scene (Lange and Seitz, 2001). The range and the amplitude information are obtained simultaneously by sampling the reflected modulated optical signal at each pixel location of the solid-state sensor. Accordingly, RCs can capture co-located range and amplitude images simultaneously at video rates. The traditional pin-hole model can be used as a physical model of the optical system for the range cameras, due to their similar structure to traditional cameras.

TOF-RCs have been used in various applications. For example, mobile robotic search and rescue (Bostelman et al., 2005; Bostelman and Albus, 2007) have been studied. Gesture recognition with TOF-RCs has been recently investigated by Li and Jarvis (2009); Lahamy and Lichti (2010, 2012). The TOF-RCs have also been applied to automatic vehicle guidance and safety systems such as wheelchair assistance. TOF-RCs have been used for outdoor surveillance as well. For example, Gonsalves and Teizer (2009) investigated detecting and tracking of human targets with a TOF-RC for outdoor surveillance in order to ensure the safety of construction workers and also to monitor their posture and movements for health related purposes in the workplace. Ray and Teizer (2012) demonstrated a real-time construction worker posture analysis for ergonomics training using 3D TOF-RCs.

1.2.2 Introduction to light coded range cameras

A light-coded range camera has an ability to estimate 3D geometry of the acquired scene at video rates as well. It is based on structured light imaging and stereo vision principle.

In general, it comprises an infrared (IR) projector, an RGB camera and an infrared depth camera. LC-RCs are based on the Primesensor chip produced by Primesense (Primesense, 2012). Currently, there are several predominant LC-RCs such as Kinect, Asus X-tion Pro and X-tion all using this chip. Kinect is one of the most popular products due to its low cost.

LC-RCs can be used in the field of computer vision for applications such as object tracking, interaction comprising gesture-based user interfaces and gaming character animation and medical applications comprising respiratory gating and ambulatory motion analysis. Xia et al. (2011) presented a human detection method using the depth information of Kinect. They used a two-step head detection and then a region growing algorithm to find the whole human body. Li (2012) used the Kinect range camera to track hand-gestures. Jia et al. (2012) discussed 3D image reconstruction and human body tracking using stereo vision and Kinect technology.

1.3 Research objectives

The main objective of this thesis develops a range camera image system to monitor dynamic deflections of individual members of structures subjected to periodic loads under laboratory conditions. In particular, the use of TOF-RCs was investigated for precise dynamic structure measurement. A post-processing method for two TOF-RCs was used to obtain dynamic measurement. A real-time target extraction method was used to obtain dynamic deflection measurement from TOF-RCs, which was the first step for realizing real time monitoring of the dynamic deflection of the concrete beam. A Kinect LC-RC was also tested for the dynamic deflection measurement of the concrete beam. As far as the author is aware, there have not been any prior publications on measuring the dynamic deflection using 3D RCs. This thesis has the following objectives:

- To develop a range camera system to measure 3D displacements of a concrete

beam subjected to periodic loads in laboratory conditions

- To develop automatic point cloud processing methods for TOF-RC data processing with 2D and 3D image processing techniques.
- To develop a system to extract targets automatically to record the concrete beam dynamic deflection in real time which can be used to detect the real-time deflection of the concrete beam in future projects.
- To create a co-located binary image and depth image for LC-RCs for developing automatic point cloud processing methods with the 2D and 3D image algorithms.
- To achieve a half-millimetre absolute accuracy of the concrete beam deflection by comparing the results of RCs and the LDSs.

1.4 New contributions

This section provides an overview of the scientific contributions.

- A system for TOF-RCs to extract the target object automatically in real time to record the concrete beam dynamic deflection has been developed, which can be used to monitor the dynamic deflection real time in future projects. To the author's knowledge, no previous work has been reported.
- A simulation method to analyze motion artefacts of TOF-RCs has been investigated. Motion artefacts of TOF-RCs were shown to be less significant for higher sampling frequency (SF).
- The deflection measurement of a concrete beam subjected to periodic loads has been successfully made using TOF-RCs with half-millimetre accuracy. To

the author's knowledge, the work is the first publication concerning the use of TOF-RCs in the dynamic deflection of the concrete beam.

- The deflection measurement of a concrete beam subjected to periodic loads has been made using LC-RCs. The raw data of LC-RCs are unstable. The LC-RCs cannot be used for the high accuracy deflection measurement unless the instability problem is solved.

1.5 Outline

Chapter 2 gives the literature review of structural deflection measurement. It includes a review of methods such as TLSs, traditional photogrammetric methods and 3D RCs which were used to measure the structure deflection measurement by other researchers. The chapter ends with a short comparison of the current literature to conclude that there are not many publications existing on the dynamic deflection of the structures with 3D RCs.

Chapter 3 discusses the background information of 3D RCs such as demodulation pixels in CCD and CMOS technologies for time-of-flight technology. Then, error sources of TOF-RCs are discussed. Furthermore, 3D coordinate derivation from range measurements of TOF-RCs is discussed. In addition, technologies of LC-RCs are discussed including active triangulation principle and error sources of LC-RCs. Finally, 3D coordinate derivation from range measurements obtained from LC-RCs is investigated.

Chapter 4 presents the experiment design and setup of the dynamic structural deflection measurement firstly. Then the sensors for the data capture during the fatigue loading tests are reported. Then, the experimental data capture with different RCs is discussed. The raw data shown in this chapter is the basis for range camera data processing in Chapter 5, which will allow readers to clearly understand the methodologies presented in Chapter 5.

Chapter 5 investigates RC data processing. This section mainly discusses methodologies for analyzing the deflection of the concrete beam. First, automatic target extraction for

SR4000 TOF-RCs is presented. Second, automatic target segmentation for Kinect LC-RCs is described. Third, displacement measurement from range camera data and time series analysis for the beam motion trajectory are discussed. Finally, the effects of motion artefacts with TOF-RCs are demonstrated.

Chapter 6 discusses results and analysis of the deflection of the individual structural members from two experimental tests. First, the simulation data of the TOF-RCs are presented and analyzed. The simulation data analysis is used to study motion artefacts of the TOF-RCs. Second, the results and analysis of Experiment I are described such as the dynamic deflection of the concrete beam estimated from SR4000 measurements at different loading frequencies. Third, the amplitudes and motion frequencies of the concrete beam motion derived from SR4000 and Kinect measurements of Experiment II are illustrated.

In addition, the results of the deflection estimates and recovered loading frequencies with the different RCs are compared with the results of LDSs. LDS technology has been well adopted for measuring the beam deflections. Therefore, it is as benchmark to analyze absolute accuracy of the other sensors.

Chapter 7 presents conclusions and recommendations for future work. The important outcome of this work is summarized. Some recommendations for the future development of this research are briefly elucidated.

Chapter 2

Literature review

Many devices can be used to measure structural deflection. There are two categories, point-wise devices and photogrammetric devices. Point-wise devices comprise dial gauges, linear-variable differential transformer displacement transducers and LDSs. These point-wise devices can measure with high accuracy but they are only able to obtain one dimensional measurement, which is a drawback (Maas and Hampel, 2006). In addition, most point-wise devices are contact sensors, which is considerable risk. If the structure is deformed, the contact sensors can be destroyed. Therefore, many researchers focus on non-contact optical sensors, acquiring 2D and 3D measurement for monitoring the structural deflection measurement. Photogrammetric methods can be used to obtain large-area, three-dimensional coverage. Therefore, recently, a great deal of research has concentrated on the deflection measurement with photogrammetric methods. Photogrammetric methods comprise TLS, traditional photogrammetric method with several passive digital cameras and RCs.

2.1 Terrestrial laser scanners for structure deflection measurements

Gordon and Lichti (2007) comprehensively discussed using TLSs for precisely measuring the structural deflection of concrete beams. Two different models of the loaded beams were described. One is single point load model, while the other one is double point load model. The two models were developed from the fundamental beam-deflection equations and implemented using a weighted-constraint, least-squares curve-fitting approach. Even though the TLS is a coarse precision instrument, sub-millmetre accuracy was obtained with the TLS point cloud when compared with a traditional photogrammetric method.

Park and Lee (2007) presented a new approach that shows the usability of a TLS for health monitoring of the structures. The TLS allows measurement of the 3D displacement of any particular shape in a structure as well as the static deformed shape of the structure. They presented four steps for measuring the displacement. The first step is the acquisition of shape information using the TLS. The second step is the generation of base vectors using least squares. The third step is the transformation from the TLS coordinate system to the structural coordinate system using the base vector derived from the second step. The fourth step is estimating the displacement within the structural coordinate system.

2.2 Traditional photogrammetric method for structure deflection measurements

Fraser and Riedel (2000) conducted research on monitoring thermal deflections of steel beams. Two groups of signalized targets such as stable reference targets and beam targets were utilized. An on-line configuration of three CCD cameras was established to measure both the stable reference points and the beam targets located at the steel beam subjected to positional displacement. During the experiment, the measurements were acquired during 70-80 epochs over two hours when the temperature of the steel beam was decreased from 1100 °C to room temperature.

Whiteman et al. (2002) discussed an experiment for measuring concrete beam deflections by using digital photogrammetry during destructive testing. They used a two-video camera system to measure vertical deflections with half-millimetre precision. They also highlighted drawbacks of the one dimensional instrument linear-variable-differential transformers to measure the beam deflections.

Maas and Hampel (2006) discussed the hardware and software modules of photogrammetric methods for civil engineering material testing and large structure monitoring. The function of the modules basically includes data acquisition and data processing. There are

several application examples: load tests on road pavement during long-term experiment, detection of cracks and measurement of crack width, bridge measurement and water reservoir wall deflection measurement.

Ronnholm et al. (2009) utilized four different sensors including TLSs, off-the-shelf digital cameras, total station and dial gauges to determine T-beam deflection and rectangular beam deflection under the different load conditions. The accuracy of the dial gauges was superior to other methods from theoretical and practical data processing, which was used as a benchmark. The absolute accuracy of TLSs, digital cameras and total station was at the half-millimetre level by comparing the estimated deflection observed by TLSs, digital cameras and total station with the dial gauges. They mentioned that using attached targets was more time consuming with photogrammetric methods. The total station is the most time consuming among the four different methods, but it is the most suitable for creating the coordinate frame over any other method. TLS have the highest resolution as compared with other three sensors.

Ye et al. (2011) proposed a new close-range digital photogrammetric system based on edge detection to estimate structural deflection displacement. The method is different from the traditional photogrammetric applications that use discrete points, signal targets. However, they used continuous edges as the controlled features to be processed in their deflection measurement system.

Detchev et al. (2012) presented a low-cost setup of multiple off-the-shelf digital cameras and projectors used for three-dimensional photogrammetric reconstruction for the purpose of measuring deflection of the concrete beam. This photogrammetric system setup was used in an deflection experiment, where a concrete beam was being deformed by a hydraulic actuator. Both static and dynamic loading conditions were measured. The system were using pattern features to reconstruct the beam deflections. Sub-millimetre level deflections could be detected by using digital cameras.

2.3 Range cameras for structure deflection measurements

Lichti et al. (2012) discussed a study on monitoring static deflection of concrete beam using a TOF-RC. They illustrated the limitations of RCs, such as deflection measurement include high (centimeter level) noise level and scene-dependent errors. They proposed models and methodologies to overcome these limitations. They reported the use of a SR4000 TOF-RC for the measurement of deflections in concrete beams subjected to flexural load-testing. Results from three separate tests showed that sub-millimeter precision and accuracy can be realized by the comparison with estimates derived from TLS data.

Zero-load tests were conducted to quantify both accuracy and repeatability of TOF-RCs. The expected null deflection and sub-milletre repeatability were realized. The concrete beam zero-state measurement mean and standard deviation (STD) were 0.00 mm and 0.21 mm respectively. Sub-millimetre accuracy was achieved for measuring the concrete beam deflection subjected to flexural load-testing by eliminating the systematic, scene-dependent bias of internal scattering through measurement differences. The influence of random errors can be reduced with temporal and spatial filtering strategies. In this paper, the authors also used the TLS to validate the results derived from the TOF-RCs. The TLS was validated with LDS measurements. They suggested that an advantage of a TOF-RC over other method is the potential to measure dynamic structural behavior at high rates with no data latency issues.

2.4 Summary

Up to now, most of the literature involving the structure deflection discussed the use of TLSs or close range photogrammetry with digital cameras for structural deflection measurement. Point devices were always used as a bench-mark to evaluate absolute accuracy derived from the photogrammetric method or TLSs. However, minor research has been devoted to measure the structural deflection with 3D RCs. No publications involved dynamic structure deflection

measurement with 3D RCs. Since the RCs have many advantages for the structural deflection measurements, technologies of RCs will be explored in Chapter 3.

Chapter 3

Range camera technologies

Range cameras are a new generation of active cameras. They allow the acquisition of 3D point cloud at video frame rates without any scanning mechanism from just one location. In this thesis, two types of RCs are studied: TOF-RCs and LC-RCs. Currently, the SR4000 TOF-RCs and the Kinect LC-RCs are the most popular RCs. The SR4000 TOF-RCs are the fourth generation TOF-RC provided by MESA Imaging AG in Switzerland. The Kinect LC-RCs were launched by Microsoft on November 4, 2010. TOF-RCs are based on the charge-coupled device /complementary metal-oxide-semiconductor (CCD/CMOS) demodulation pixel technology, while LC-RCs are based on the active triangulation principle with coded light.

This chapter mainly focuses on technologies of RCs. Section 3.1 describes the technologies of TOF-RCs such as time-of-flight range measurement principle, demodulation pixels in CCD/CMOS, demodulation and sampling to estimate ranges and their error sources. Furthermore, Section 3.2 investigates how to derive 3D coordinates of an object target from the range measurements obtained from TOF-RCs. Section 3.3 investigates the technologies of LC-RCs such as triangulation algorithm, light coded-word technologies and conjugate point identification. Error sources of LC-RCs are also described. Lastly, Section 3.4 illustrates how to obtain 3D coordinates from the light coded range measurements.

3.1 Time-of-flight range camera technology

3.1.1 Time-of-flight range camera measurement principle

Range measurements can be derived by the time-of-flight principle, which means that it is possible to measure the absolute depth by calculating the time delay or the phase shift

between emitted light and reflected light if the speed of light is precisely known (Lange and Seitz, 2001). By calculating the phase shift between an emitted and its reflected signal, range measurements can be derived if modulation frequency (MF) is known. This measured phase directly corresponds to the time-of-flight.

There are three different modulation methods for time-of-flight technology (Lange, 2000). They are pulsed modulation, continuous wave modulation and pseudo-noise modulation. Most TOF-RCs are based on the first two modulation methods.

SR4000 TOF-RCs are based on the continuous wave modulation time-of-flight technology with known MFs, demodulation and detection method (Lange, 2000). Figure 3.1 shows a SR4000 TOF-RC.

Figure 3.1: A SR4000 TOF-RC

A TOF-RC illuminates the entire scene with modulated light cone, which is illustrated in Figure 3.2. The reflected signal is demodulated and sampled by using a 2D electric optical demodulator and detector in the receiver. The distance between a camera and a target object at each pixel is estimated as a fraction of one full cycle of the modulated signal, where the distance corresponding to one full cycle, which is called non-ambiguity range is given by Equation 3.1 (MESA-Imaging, 2012).

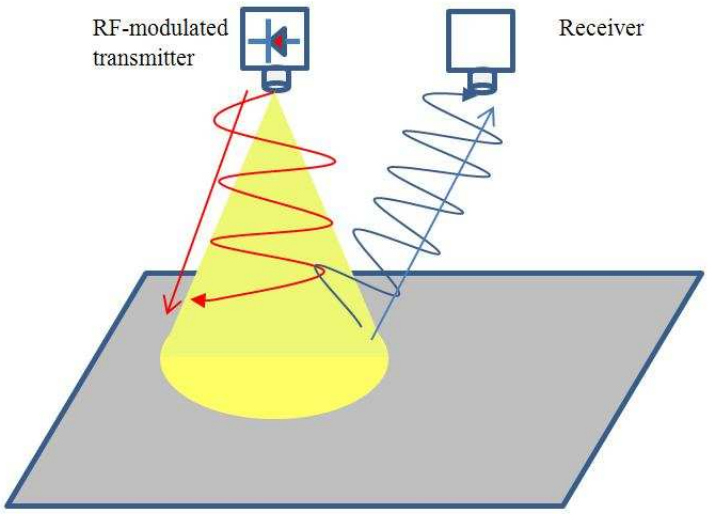

Figure 3.2: Continuous-wave time-of-flight phase-measurement principle

$$D = \frac{c}{2f_m} \tag{3.1}$$

where c is speed of light and f_m is the MF. Table 3.1 shows the non-ambiguity range (NAR) of TOF-RCs with different MFs and speed of light 299792458 m/s.

Table 3.1: Non-ambiguity range of TOF-RC

f_m (MHz)	29	30	31
NAR (m)	5.169	4.997	4.835

3.1.2 Demodulation and sampling for range estimation

The range measurements of TOF-RCs are derived by calculating the phase difference between the emitted light and the received light. The reflected signal is demodulated by using the cross-correlation method (Lange et al., 2000), which means that the demodulation of a received modulated signal can be calculated by using the correlation between the received modulated signal and the original modulated signal. The reflected modulated signal

$s(t)$ (Equation3.2) (with amplitude K and phase φ) and the original modulated signal $g(t)$ (Equation 3.3) are utilized to calculate the cross-correlation function $c(\tau)$ (Equation 3.4, (Lange and Seitz, 2001)).

$$s(t) = 1 + K \cdot \cos(\varpi t - \varphi) \tag{3.2}$$

$$g(t) = \cos(\varpi t) \tag{3.3}$$

$$c(\tau) = s(t) \bigotimes g(t) = \frac{K}{2} \cdot \cos(\varphi + \tau) \tag{3.4}$$

The cross-correlation function is sampled four times at different moments as shown in Figure 3.3. As can be seen, the four discrete sampling measurements are provided. The wave is sampled with four equally spaced sampling points of duration Δt. $\tau_0 = 0°$, $\tau_1 = 90°$, $\tau_2 = 180°$ and $\tau_3 = 270°$ are chosen. By considering the received signal is often superimposed onto a background image, we have to add an offset value B to obtain the practical measured values.

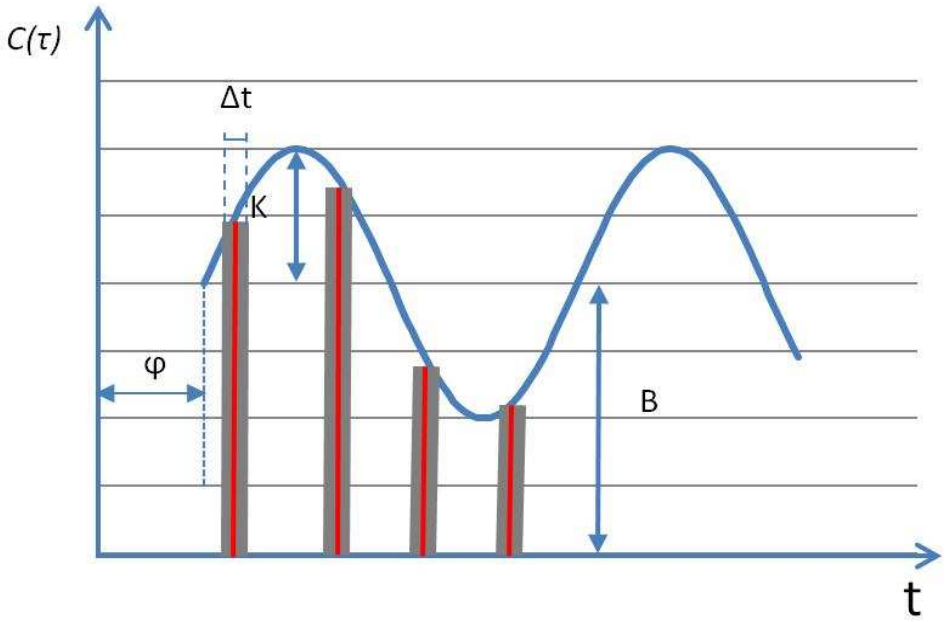

Figure 3.3: The time-of-flight sampling of cross-correlation

The four discrete sample measurements are given by Equations 3.5 (Lange and Seitz, 2001).

$$\begin{cases} C(\tau_0) = \dfrac{K}{2} \cdot \cos(\varphi) + B \\ C(\tau_1) = -\dfrac{K}{2} \cdot \sin(\varphi) + B \\ C(\tau_2) = -\dfrac{K}{2} \cdot \cos(\varphi) + B \\ C(\tau_3) = \dfrac{K}{2} \cdot \sin(\varphi) + B \end{cases} \tag{3.5}$$

According to the four sample measurements, the phase φ and amplitude K of the reflected optical signal can be recovered from Equations 3.7 and 3.8 (Lange and Seitz, 2001). Then, the range measurement (Equation 3.8) can be derived by scaling the phase difference (Equation 3.7) (Lange and Seitz, 2001) as follows:

$$K = \frac{\sqrt{[C(\tau_0) - C(\tau_2)]^2 + [C(\tau_1) - C(\tau_3)]^2}}{2} \tag{3.6}$$

$$\varphi = \arctan(\frac{C(\tau_3) - C(\tau_1)}{C(\tau_0) - C(\tau_2)}) \tag{3.7}$$

$$\rho = \frac{\varphi c}{4\pi f_m} \tag{3.8}$$

where ρ is the range from the TOF-RCs to the target; c is the speed of light and f_m is the MF.

3.1.3 Time-of-flight range camera error sources

Many factors influence the geometric measurement accuracy of TOF-RCs and a lot of research has been focused on them.

The first category is noise comprising signal noise, time variant noise and time invariant noise which have an effect on captured measurement data of TOf-RCs. Generally, the noise can be deducted by either averaging the multiple image frames or using temporal and spatial

smoothing filtering strategies such as simple Gauss and edge preserving bilateral (Lindner et al., 2010).

The second category is composed of systematic artefacts which depend on system environment such as ambient imaging conditions and object scene structure. For example, external experiment environment temperature, sensor internal temperature, multi-path, and scattering effect. Multi-path is caused by multiple reflection of the signal. TOF-RC geometric measurements are affected significantly due to the scattering artefacts caused by secondary reflections occurring between the lens and the image plane (Jamtsho and Lichti, 2010; Foix et al., 2011; Lichti et al., 2012). Jamtsho and Lichti (2010) investigated the scattering-caused range measurement error to SR3000 and SR4000 TOF-RCs. The effects of scattering error caused by SR4000 are much smaller than for the scattering error caused by SR3000. Lichti et al. (2012) discussed an empirical scattering error compensation model. The model was implemented in the integrated self-calibration bundle adjustment for TOF-RCs. It was illustrated to be effective in removing the systematic error trends in background target range residuals and results in measurable statistical improvement.

The third group of factors is scene-independent systematic artefacts caused by camera operating conditions. Chiabrando et al. (2009) estimated that warm-up time was at least forty minutes to achieve stable geometric measurements. In addition, Piatti and Rinaudo (2012) investigated the scene-independent systematic artefacts of SR4000 TOF-RCs and the CamCube3.0 TOF-RCs provided by PMD technologies. Over forty minutes warm-up time was suggested to obtain stable measurements as well. The warm-up time affects the geometric measurement accuracy of TOF-RC. For the CamCube3.0, the range measurement accuracy variations are over centimeters during warming-up time. The integration time is the length of time that pixels are allowed to collect light. The integration time impacts the range camera geometric measurement (Piatti and Rinaudo, 2012). The higher integration time is set, the higher measurement precision is obtained. It is necessary to properly adjust

the integration time.

The fourth important group comprises scene-independent instrumental systematic errors which are due to each of the individual components and assembly errors (Lichti and Kim, 2011). This group also includes lens distortion (radial and decentring) which is the same as for the traditional digital cameras. The range error is another type of systematic error source containing rangefinder offset, scale error, cyclic error and clock-skew or latency error. The rangefinder offset is an offset of the range measurement originating from the perspective centre. The scale error is caused by incorrect MF. The cyclic error stems from asymmetric response of the near infrared LED signal. This asymmetric response causes a non-harmonic sinusoidal illumination. Since a standard sinusoidal illumination is a basic assumption, the computed phase-delay and distance are inaccurate. The phase-delay partially comes from the latencies on the CCD or CMOS sensors due to signal-propagation-delays and semiconductor properties. Because the emitted signal and the received signal are correlated directly on the sensor array, the different latencies for every pixel have to be taken into account. This latency-related error (Fuchs and Hirzinger, 2008) leads to biases of range measurements. Because of non-linearities of semiconductors and non-perfect separation properties, a different number of photons at a constant distance cause different range measurements.

The fifth group is motion artefacts which are from the physical motion of the objects or the camera during the integration time of sampling. Lottner et al. (2007) found that motion artefacts include two categories: lateral motion artefacts and axial motion artefacts. They proposed a combination method with a traditional 2D image sensor and a TOF-RC to detect the lateral motion artefacts by using a classifiable 2D image edge detection method. Provided that an arbitrary edge can be obtained from the 2D edge image, an average of located weighted neighboring pixels is an interesting approach to correct motion artefacts. In addition, they discussed using a two phase sample algorithm instead of using a four phase sample algorithm to derive range. Lindner and Kolb (2009) investigated that fixed per-pixel

sampling schema was discarded by tracking individual surface points in all phase images. They selected the correct object location in the phase image to determine the phase values for final distance calculation. Lateral motion artefacts were detected first by calculating the optical flow between the intensity images from TOF-RCs. Then, the axial motion artefacts can be removed by using the axial motion estimation approach and a theoretical model for axial motion deviation errors.

3.1.4 Time-of-flight range camera self-calibration

The full metric potential usage of the 3D range cameras, like traditional cameras, cannot be realized if there is not a complete systematic error model and a related calibration procedure to estimate all model parameters including the coefficients for lens distortion and range biases. The lens distortion includes radial and decentering lens distortion, while the range biases comprise rangefinder offset, scale error, periodic error terms and signal propagation delay error (Lichti et al., 2010).

In order to estimate those model coefficients, a rigorous calibration procedure is desired. Many researchers have focused on the calibration procedure of TOF-RCs. They have investigated various forms of a self-calibration approach for TOF-RCs which can be classified as either a two-step process or a one-step integrated approach. Kahlmann et al. (2006) investigated a two-step process. The standard lens distortion was calibrated first. Then, the range error was corrected for a single central pixel of the range camera sensor array over a high-accuracy baseline. Variations of the distance calibration as a function of location in an image plane were modelled on a pixel-wise basis. Lindner and Kolb (2006) discussed a two-step calibration method to calibrate TOF-RCs. Those two steps include a lateral calibration from classical 2D sensors and a calibration of the distance measuring process. For distance calibration, there are two distinct steps: a global distance adjustment for the entire image and a local per-pixel adaption to obtain better results for the global adjustment. Lichti et al. (2010) presented a new method for integrated range camera systematic

calibration in which both traditional camera calibration parameters and rangefinder systematic error parameters are estimated simultaneously in a free-network bundle adjustment of observations using signalized targets. They discussed that only six datum constraints are necessary since the range observations implicitly define the free-network and the scale due to the integrated self-calibrating bundle adjustment method. Lindner et al. (2010) proposed a combined calibration approach for PMD-distance sensors. The combined model covers: estimation of the intrinsic and extrinsic parameters, adjustment of range error and correction of additional reflectivity related deviation. Shahbazi et al. (2011) used a calibration approach based on photogrammetric bundle adjustment incorporating a digital camera in the calibration process in order to overcome field of view limitation and low pixel resolution of TOF-RCs.

3.2 Three dimensional coordinates from time-of-flight range measurements

The range measurements are derived from the time-of-flight principle. The output of the TOF-RCs comprises various measurements such as intensity, distance confidence map and Cartesian coordinates. Therefore, it is important to know how to obtain Cartesian coordinates from the range measurements obtained from TOF-RCs. Figure 3.4 illustrates how to derive them.

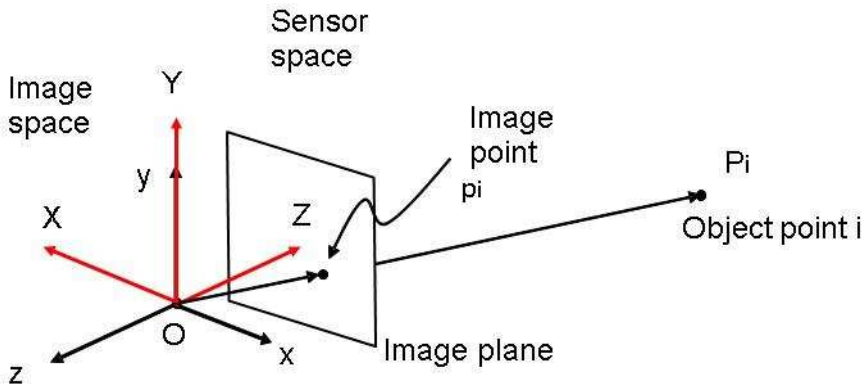

Figure 3.4: 3D co-ordinates from range measurement

An important output of TOF-RCs is range measurements which are measured independently at every pixel in the sensor frame. The image space coordinate system and the sensor space coordinate system have the same origin O. The 3D coordinates of the image point p_i in the image space coordinate system are $(x_i - x_p, y_i - y_p, -p_d)$, where (x_p, y_p) is principal point offset and p_d is principal distance. The 3D coordinates of object point P_i in the sensor space coordinate system are (X_i, Y_i, Z_i). The measurement range ρ_i is the distance from the origin O to the object point in 3D object space. Based on the pinhole camera model and similar triangles, the 3D coordinates of the object point P_i are calculated by using the known image coordinates in accordance with Equation 3.10.

$$\frac{\overrightarrow{Op_i}}{\overrightarrow{OP_i}} = \frac{\sqrt{(x_i - x_p)^2 + (y_i - y_p)^2 + {p_d}^2}}{\rho_i} \tag{3.9}$$

$$\begin{bmatrix} X_i \\ Y_i \\ Z_i \end{bmatrix} = \frac{\rho_i}{\sqrt{(x_i - x_p)^2 + (y_i - y_p)^2 + {p_d}^2}} \begin{bmatrix} -(x_i - x_p) \\ y_i - y_p \\ p_d \end{bmatrix} \tag{3.10}$$

3.3 Light coded range camera technology

Most commercial LC-RCs are based on PrimeSense chips. Generally, a LC-RC consists of an RGB-camera, an IR projector and an IR depth camera illustrated in Figure 3.5. The IR light coded pattern emitted from the IR projector is projected onto the scene in order to obtain a matrix implementation of active triangulation principle for estimating depth measurements and 3D geometry. This section discusses active triangulation for LC-RCs and error sources of Kinect LC-RCs.

3.3.1 Triangulation algorithm

A LC-RC is essentially a stereo vision system based on triangulation. A stereo vision system consists of two standard (typically identical) cameras whose fields of view partially overlap.

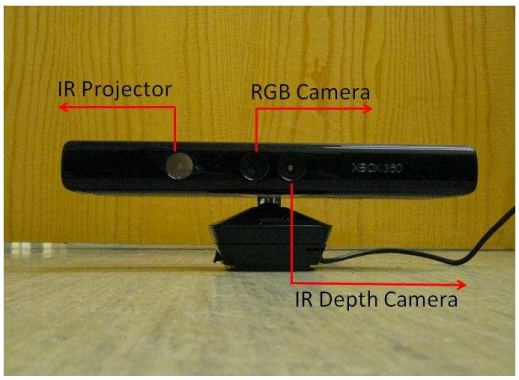

Figure 3.5: A Kinect

Additionally, two cameras of a stereo vision system are coplanar and have aligned imaging sensors and parallel optical axes. The two cameras of a stereo vision system are illustrated in Figure 3.6. The left camera L is called the reference camera with coordinate system (x_L, y_L, z_L) and the right camera is called the target camera with coordinate system (x_R, y_R, z_R).

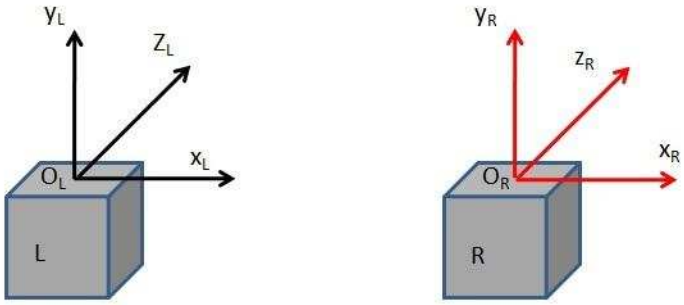

Figure 3.6: Stereo vision system

In the stereo vision system, an object point P with 3D coordinates (x, y, z) in the reference camera coordinate system is projected into the stereo cameras whose corresponding 2D image coordinates are $p_L = (u_{p_L}, v_{p_L})$, $p_R = (u_{p_R}, v_{p_R})$ respectively as shown in Figure 3.7. p_L and p_R (Mutto et al., 2010) have the same vertical coordinates. According to the stereo vision system principle, there are $u_{p_R} = u_{p_L} - d$ and $v_{p_R} = v_{p_L}$, where d is the difference between the horizontal coordinates of p_L and p_R, which is called the disparity. In addition,

by triangular similarity the disparity is inversely proportional to the depth value z as in Equation (3.11,(Klette et al., 1998)).

$$z = \frac{b|f|}{d} \tag{3.11}$$

where b is the baseline which is the distance between the two camera perspective centers and f is the common focal length of the two cameras.

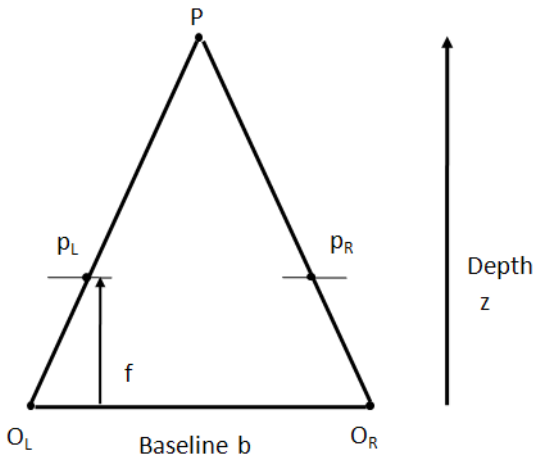

Figure 3.7: Triangulation with a pair of stereo cameras

From the 2D image coordinates of p_L and its corresponding depth z obtained from Equation 3.11, the 3D coordinates of the object point P can be derived by following Equation 3.12 (Mutto et al., 2010).

$$\begin{bmatrix} x \\ y \\ z \end{bmatrix} = K_L^{-1} \begin{bmatrix} u_{pL} \\ v_{pL} \\ 1 \end{bmatrix} z \tag{3.12}$$

where K (Equation 3.13, (Mutto et al., 2010)) is the matrix of intrinsic parameters of the stereo cameras.

$$K = \begin{bmatrix} f & 0 & x_p \\ 0 & f & y_p \\ 0 & 0 & 1 \end{bmatrix} \tag{3.13}$$

A light coded camera system is basically a stereo vision system with one of two cameras replaced by a projector. The stereo vision system of a LC-RC is comprised of a camera C and a projector A as shown in Figure 3.8. The camera C has a camera coordinate system (x_C, y_C, z_C). This camera coordinate system is also called the reference coordinate system. The projector A has a projector coordinate system (x_A, y_A, z_A). The camera C is an IR depth camera and a projector is used to emit an IR light pattern.

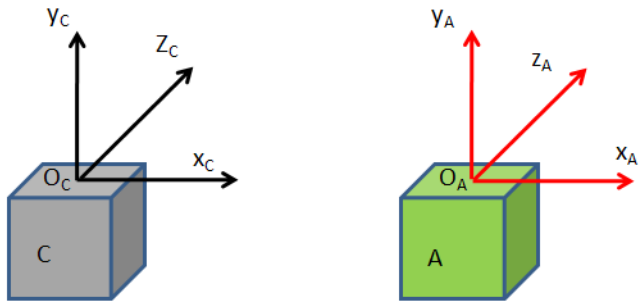

Figure 3.8: Light coded system

3.3.2 Light code-word technologies

Each pixel of a projector should have an associated code-word, which can simplify conjugate point identification. Namely, each pixel has a specific local configuration in the projected pattern. The specific pattern is projected onto the scene by the projector. Then, the pattern is reflected by the scene and captured by the camera. The main purpose of using the projected pattern is to obtain conjugate points between the camera image and projector image by analyzing received code-words in the images of the cameras. Therefore, the goal of the pattern design is to design a set of code-words which can be effectively decoded even if the pattern projection or acquisition process is not perfect.

A pixel $p_A = (u_A, v_A)$ of the pattern, its corresponding object point P and its corresponding image point $p_C = (u_C, v_C)$ are illustrated in Figure **??**. The projection or acquisition procedure introduces a horizontal shift d which is proportional to the inverse of the depth z

of P as the Equation 3.11. The disparity shift d is the most critical quantity and should be measured accurately in an active triangulation process, since it is used to measure the 3D coordinates of the object point P by using Equation 3.12.

There are three code-word methods discussed in Mutto et al. (2010) for LC-RCs as follows:

1. Direct coding as shown in Figure 3.9 is a code strategy in which a code-word is associated to p_A represented by the pattern value at p_A. The gray-level or RGB value of the pattern at p_A is used. It is the easiest code-word method to perform. This code-word allows for dynamic scene capture because it just requires a single pattern projection. However the disadvantage of the direct coding method is that it is extremely sensitive to color or gray-level distortion because of scene color distribution, reflectivity properties and external illumination.

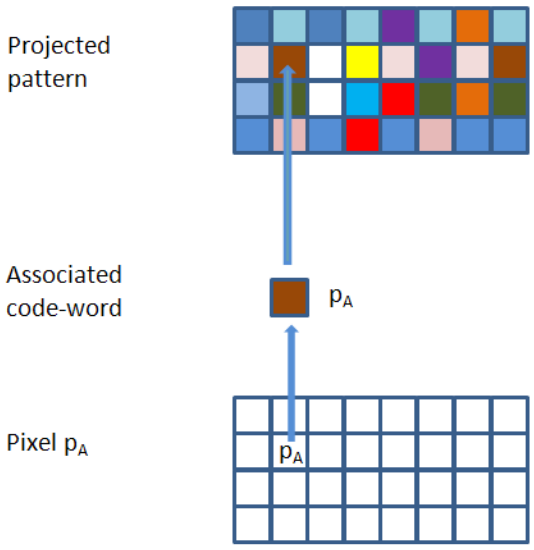

Figure 3.9: Direct coding

2. Time-multiplexing coding shown in Figure 3.10: a sequence of T patterns is projected onto a surface to be measured at a subsequent time t. The code-word associated to each pixel p_A is a sequence of the T pattern values (i.e., of gray-level or color values) at p_A.

Time-multiplexing coding uses a very small set of binary patterns for creating arbitrarily different code-words for each pixel. Its major disadvantage is that it requires the projection of a time sequence of T patterns for every single depth measurement, hence it is not suited in dynamic scenes.

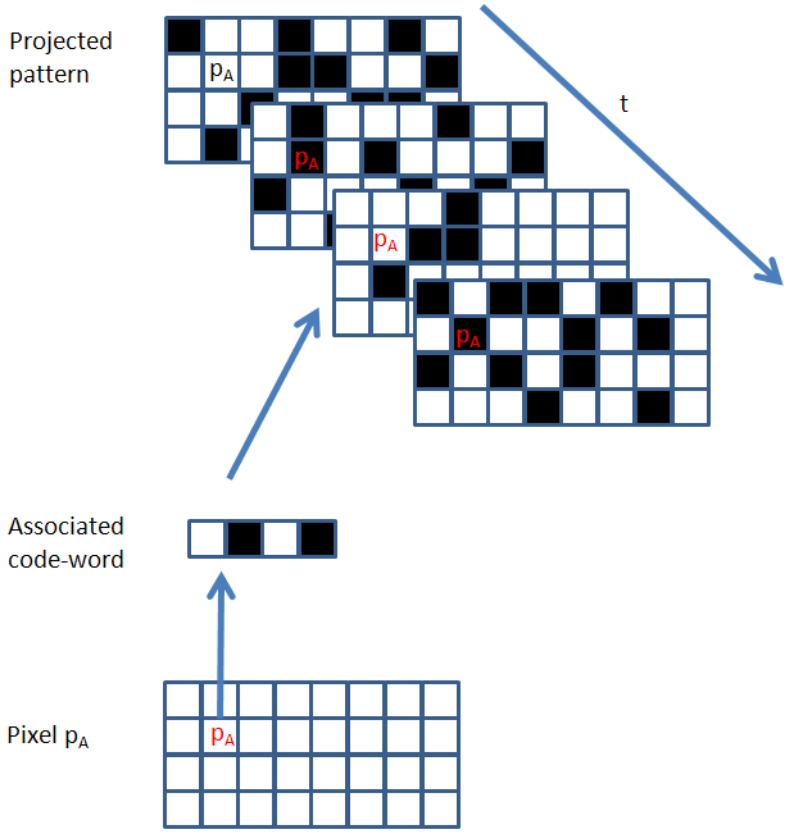

Figure 3.10: Time-multiplexing coding

3. Spatial-multiplexing coding illustrated in Figure 3.11: the code-word associated to each pixel p_A is a spatial pattern distribution in a window of n_W pixels centered around p_A. For example, for a window with 9 rows and 9 columns so n_W is equal to 81.

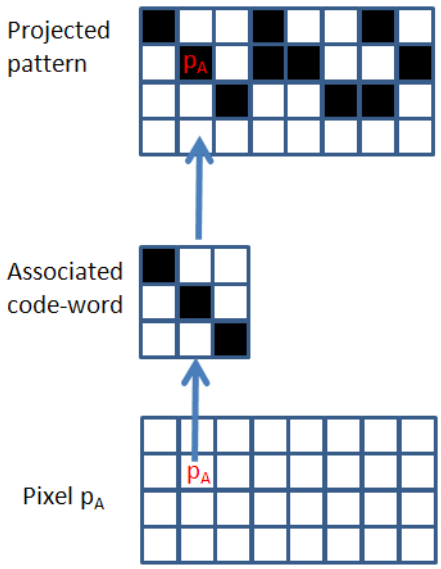

Figure 3.11: Spatial-multiplexing coding

The spatial-multiplexing techniques are the most interesting for the acquisition of dynamic scenes since they only require the projection of a single pattern, which is similar to the direct coding methods. Furthermore, they can also deal with noise and color or gray-level distortion caused by scene color distribution, reflectivity properties and external illumination. The choice of the window size n_W associated to each code-word influences the robustness of dealing with the distortion. The smaller n_W is chosen, the more robust is the coding with respect to lens distortion, since it is more likely that all the scene points on which the pattern window is projected share the same disparity. The bigger n_W is chosen the greater is the robustness of dealing with noise or color distortion caused by the projector and the cameras.

3.3.3 Conjugate point identification

The Kinect light coded range camera utilizes the spatial-multiplexing code word approach which can robustly capture dynamic scenes at a frame rate as high as 30 fps. The laser

projector of a Kinect emits a single beam which is split into multiple beams by a diffraction grating to create a spatial-multiplexing pattern of speckles (Freedman et al., 2012). The spatial-multiplexing pattern is projected onto the scene. This pattern is captured by the infrared depth camera. By calculating the covariance (Equation 3.14) (Mutto et al., 2010) between the spatial-multiplexing window centered at a given pattern point p_A^i and the projected pattern captured by the IR camera, the conjugate points of the projector and the IR depth camera are identified, which is called local algorithm.

$$C(u^i, u^j, v^j) = \sum_{(u,v)\in W(u_A,v_A)} [s(u-u_A^i, v-v_A^i)-\bar{s}(u_A^i, v_A^i)]\cdot[s(u-u_C^j, v-v_C^i)-\bar{s}(u_C^j, v_A^i)] \quad (3.14)$$

$$\bar{s}(u_A^i, v_A^i) = \sum_{(u,v)\in W} s(u-u_A, v-v_A) \quad (3.15)$$

where $\bar{s}(u_A^i, v_A^i)$ is the average of the spatial multiplexing window centered at $(u_A^i, v_A^i)^T$ and $C(u^i, u^j, v^j)$ is the horizontal covariance of the projected pattern between p_A^i and p_C^j.

Therefore, for a given pixel p_C^j and all the pixels p_A^i in the same row as p_C^j in the projected pattern, the covariance presents a unique peak in correspondence with the actual couple of conjugate points.

The local algorithm considers a measurement of the local similarity between all pairs of possible conjugate points. However, this method requires a great number of complex computations, which is time-consuming computations. Therefore, detection of the conjugate points to meet the high frame video rate is necessary. However it is not possible to meet the high frame video rate requirement by using a local algorithm to identify the conjugate points .

Freedman et al. (2012) discussed using a reference image. The reference image can be obtained by capturing a plane at a known distance from the camera. The reference is stored in the memory of the camera. When the speckles from the IR light are projected onto an object, there is a distance between the object and the sensor. If the distance is smaller or larger than the known distance, the position of the speckle in the infrared image will

be shifted towards the baseline between the IR projector and the IR depth camera. The shifts of all speckles can be determined by a simple image correlation procedure, which yields conjugate points and a disparity matrix. The distance of each pixel to the sensor can then be retrieved from the corresponding disparity and conjugate points by using the triangulation algorithm.

3.3.4 Light coded range camera error sources

For the LC-RCs, different error sources such as the sensor, the measurement setup and the environment of the scene impacts the depth measurements.

The sensor errors are caused by inadequate calibration and inaccurate measurement of disparities.

The systematic errors should be considered first. Since there are three different sensors of Kinect LC-RCs, the three sensors also have common systematic errors of three sensors including lens distortions (radial and decentring) and range errors. In addition, the relative orientation between the RGB camera and the IR depth camera is not estimated or modelled properly which can cause the errors. Inadequate calibration or errors in estimation of calibration parameters results in systematic errors. Such systematic errors can be eliminated by a proper calibration procedure. Herrera et al. (2011) discussed Kinect camera calibration using a planar check-board pattern. Chow et al. (2012) investigated a new calibration model for simultaneously determining exterior orientation parameters, interior orientation parameters and object space feature parameters.

Inaccurate measurements of disparities within the correlation algorithm during normalization also results in errors.

Errors are also caused by environment of the scene, which are also called scene dependent errors. The scene dependent errors are related to the system environment, e.s. ambient imaging conditions, and object scene structure, e.s. external experiment environment temperature and sensor internal temperature. First, the light conditions impact the corre-

lation and computation of disparities. Under strong light, the laser speckles appear with low contrast in the infrared image, which can lead to outliers or gaps in the output depth measurements. Second, some other aspects influence the depth measurement accuracy. For example, low reflectivity and background illumination impact the measurement of points. In case of low reflectivity and excessive background illumination, the camera can not acquire any information about the reflected pattern. The corresponding estimation algorithm does not produce any results. Hence in these situations, there is generally no depth information available.

Another error is caused by camera operating conditions. Chow et al. (2012) discussed that at least 60 minutes warm-up is necessary to obtain stable depth measurement from LC-RCs.

3.4 Three dimensional coordinates from light coded range measurements

The LC-RCs provide depth measurements and RGB measurements due to their measurement principle. However, it is critical to derive 3D coordinates from the depth measurements of LC-RCs shown in Equation 3.16((Khoshelham and Elberink, 2012))

$$\begin{cases} X_k = -\dfrac{depth_k}{f}(x_k - x_p + \Delta x) \\ Y_k = -\dfrac{depth_k}{f}(y_k - y_p + \Delta y) \\ Z_k = depth_k \end{cases} \tag{3.16}$$

(x_k, y_k) are image coordinates of the image point k;

(x_p, y_p) are coordinates of the perspective centre;

$(\Delta x, \Delta y)$ are additional calibration parameters;

(X_k, Y_k, Z_k) are 3D coordinates of the object point k;

f is focal length of the IR depth sensor;

$depth_k$ is the depth measurement from the IR depth sensor.

3.5 Summary

First, this chapter reported on the range camera technologies of TOF-RCs. TOF-RCs use the time-of-flight measurement principle and four discrete measurement samples to derive range measurements. Additionally, error sources in the TOF-RCs were described such as noise, systematic artifacts, scene-independent systematic artefacts, scene-independent instrumental systematic effects and motion artefacts. Finally, derivation of 3D coordinates was discussed using range measurement from TOF-RCs.

Second, this chapter discussed the LC-RCs as well. It is a new type of 3D LC-RCs. They are designed on the basis of stereo vision technologies and coded light. They use a reference image to estimate disparities and derive the depth using the disparities, baseline and focal length of IR depth camera. In addition, error sources of LC-RCs were also presented such as sensors, measurement setup and environment of the scene. Based on the studies for RCs, the concrete beam experiment is going to be discussed in the next chapter.

Chapter 4

Structure deflection measurement experiment description

In this chapter, Section 4.1 discusses the experiment design and setup for measuring dynamic concrete beam deflection. Section 4.2 describes the sensors for the data capture during the fatigue loading tests. Four different types of optical sensors are used to measure the beam deflection. Their specifications are described in this section. Section 4.3 reports the data capture procedure. Section4.4 reports the raw data of the beam deflection from the different sensors. The raw data discussed in this chapter is the basis for the range camera data processing in Chapter 5. The experimental details are presented first to help readers more clearly understand the methodology that is presented in Chapter 5.

4.1 Experiment design and setup

Figure 4.1 and Figure 4.2 show the experimental arrangement for measuring the concrete beam deflection subjected to periodic loads, which are called fatigue loading tests. The fatigue loading test experiment was conducted by Dr. Mamdouh El-Badry in the Department of Civil Engineering MikeWard Structural Laboratory at the University of Calgary. As can be seen in Figure 4.2, a 3 m long, reinforced concrete beam having a 150 mm $\times$ 300 mm rectangular cross section was supported at its two ends and was painted white. A hydraulic actuator was used to apply the periodically-varying loads to the concrete beam through a spreader beam in contact with the top surface of the concrete beam.

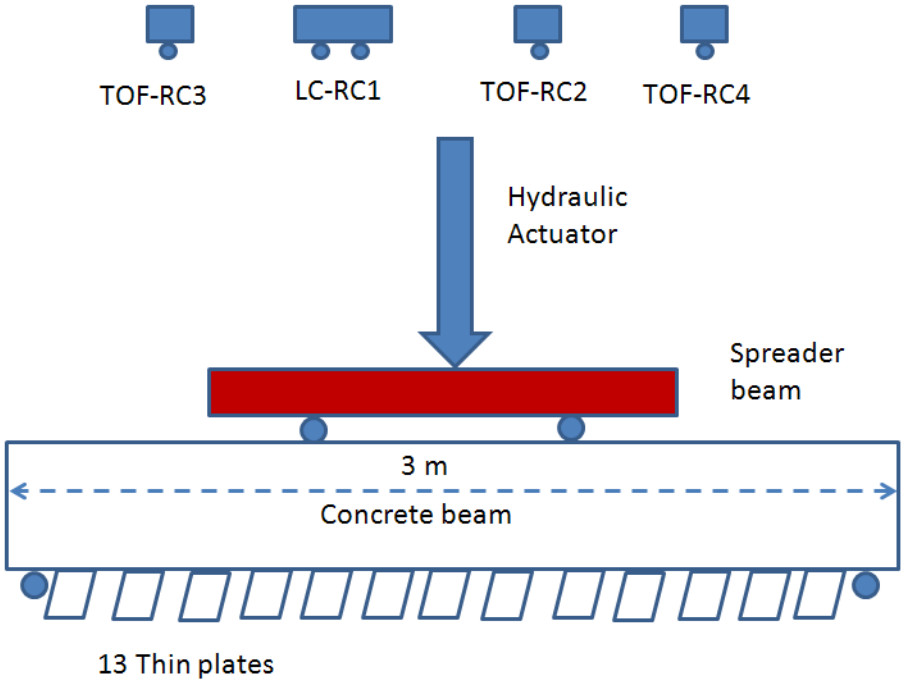

Figure 4.1: Schematic view of the experiment setup

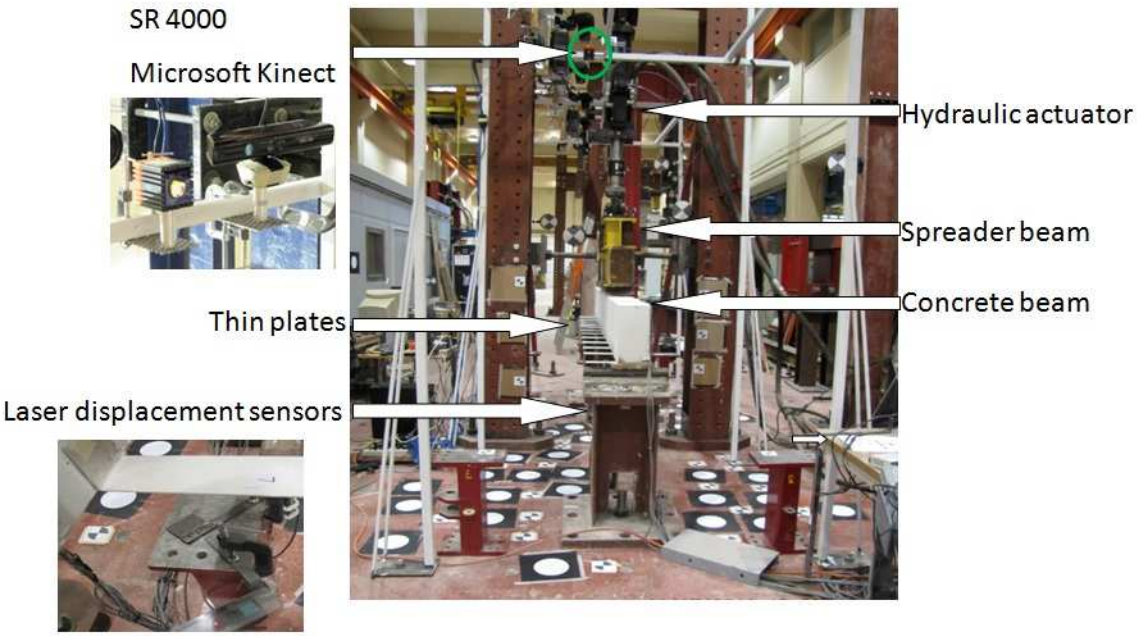

Figure 4.2: Photographic image of actual experiment setup

The experimental setup for measuring dynamic concrete beam deflection comprised three TOF-RCs, one LC-RC (LC-RC 1), five LDSs and a target system. Three different SR4000 TOF-RCs were used to capture data during the experiment. They are two ethernet cable SR4000-00400011 (TOF-RC 3 and TOF-RC 4) and one USB cable SR4000-0040001 (TOF-RC 1). In this thesis, LC-RC 1, TOF-RC 1, TOF-RC 3 and TOF-RC 4 are called Cam 1, Cam 2, Cam 3 and Cam 4 respectively. The target system compirsed thirteen thin plates and a concrete beam. The surface of interest for the range cameras was the top surface of the concrete beam. Since the spreader beam occluded almost half of the concrete beam, an alternative method was used to measure the target system. Thirteen white-washed thin aluminum plates (220 mm $\times$ 50 mm) were bonded to the side of the concrete beam at intervals of 250 mm along its length.

4.2 Sensors

4.2.1 SR4000 time-of-flight range camera

SR4000 TOF-RCs were positioned on the steel frame of each side of the hydraulic actuator with nadir-looking orientation and 1.9 m standoff distance from the camera to the top surface of the concrete beam for complete coverage of the concrete beam. Table 4.1 gives the specifications of the TOF-RCs. As can be seen, the absolute accuracy of SR4000 TOF-RC is 10 mm provided by the manufacturer. The maximum frame rate is 54 fps.

Since the deflection measurement of the concrete beam has to be made in the direction of the gravity vector, the Z-axis for the range camera has to be aligned as close to the gravity vector as possible (Jamtsho, 2010). Moreover, the TOF-RCs do not have a leveling system so a small external level was required to align the Z-axis of the camera coordinate system with the gravity vector.

Table 4.1: Specifications of SR4000 TOF-RC

Camera Type	SR4000-0040001	SR4000-00400011
Pixel array (pixel^2)	176×144	176×144
Field of view	$43.6° \times 34.6°$	$69° \times 56°$
Focal length (mm)	10	5.8
Illumination wavelength (nm)	850	850
Modulation frequency (MHz)	29/30/31	29/30/31
Detection range (m)	0.1-5	0.1-5
Calibrated range (m)	0.8-5	0.8-5
Maximum frame rate (fps)	54	54
Absolute accuracy (mm)	± 10	± 10

4.2.2 Kinect light coded range cameras

One Kinect (Cam 1) was utilized for data capture. It was positioned on the steel frame next to one of the SR4000 ethernet cameras. It is difficult to see the Kinect location in Figure 4.2 since it was hidden behind the TOF-RCs. Table 4.2 gives specifications of the Kinect LC-RC.

Table 4.2: Specifications of Kinect LC-RC

Camera name	Kinect
Field of view	$57° \times 43°$
Frame rate (Hz)	30
Camera resolution	640×480
Nominal depth resolution (mm)-at 2m distance	3
Nominal depth range (m)	0.8-3.5
Absolute accuracy (mm)	± 10
Device connection	USB

4.2.3 Laser displacement sensors

The deflection measurements were also recorded by five vertically-oriented KEYENCE LKG407 CCD LDSs positioned directly under the centroid of five of the thin plates. These devices measure displacement by active laser triangulation. The manufacturer stated linearity and precision for this sensor is 0.05% of the 100 mm measurement range and 2 μm, respectively.

Therefore, the LDSs were used as a benchmark to assess the absolute accuracy of the beam deflection measurement. The LDS data were provided by Dr. Mamdouh El-Badry.

4.3 The experiment data capture

4.3.1 Data capture procedure

Designed by Dr. Mamdouh El-Badry, Experiment I was comprised of two static loading and fatigue loading cycles. The periodic loading cycles with 4 mm maximum amplitude based on the load control were applied to the concrete beam. In general, fatigue loading tests are commonly conducted at 3 Hz (Papakonstantinou et al., 2001; Heffernan and Erki, 2004). However, in order to meet the sampling frequency requirement of the low-cost digital camera system (Detchev et al., 2012), the 1 Hz loading frequency fatigue loading testing was conducted as well. Two TOF-RCs were used to capture 3D image data. The cameras were used to capture the fatigue loading cycles and record the dynamic deflections fo the concrete beam. Initially, 7,200 load cycles were applied from 24 kN to 96 kN at 1 Hz loading frequency. Subsequently, 3 Hz periodic loads were applied. It took two days until the beam failed.

Designed by Dr. Mamdouh El-Badry, Experiment II also includes static loading and fatigue loading tests. The periodic loads based on force control were applied to the concrete beam at different loading frequencies. It took eleven days to apply the periodic loads to the concrete beam. Measurement data were recorded at 1 Hz for six days and at 3 Hz for 10 days.

4.3.2 Operation conditions of SR4000

During the dynamic data capture, several quality assurance measures were taken to obtain stable measurement data for the TOF-RCs.

First, the SR4000 TOF-RCs had been warmed up for one hour to obtain stable measure-

ment data.

Second, the light of multiple TOF-RCs would interfere with each other if they were operated with the same MF. Therefore, different modulation frequencies were used to prevent light interference. In Experiment I, Cam 3 was set at 29 MHz MF and Cam 4 was set at 31 MHz MF. During Experiment II, Cam 3 was set at 30 MHz and Cam 4 was set at 31 MHz. In addition, the SR4000 USB cable range camera (Cam 2) was mounted on the steel frame for data capture. It was located next to one of internet cable TOF-RCs. The MF of Cam 2 was set at 29 MHz.

Third, an appropriate integration time should be chosen for TOF-RCs to capture the data. The frame rate is inversely proportional to the integration time. In addition, the range measurement precision is related to the integration time. When the integration time is longer, the range measurement precision is higher. When the integration time is short, the range measurement precision is lower. In our case, the nominal motion frequencies were 1 Hz and 3 Hz respectively. The SFs should be 2 Hz and 6 Hz when the Nyquist critical frequencies are 1 Hz and 3 Hz respectively.

The integration times for both TOF-RCs were set at different values: 21 ms, 8.5 ms, 4.4 ms and 2.2 ms for which the corresponding SFs were 10 Hz, 20 Hz, 30 Hz and 40 Hz respectively during Experiment I. However, according to the results and analysis of Experiment I, the best SF was 20 Hz to keep measurement error under half-millimetre level accuracy. Therefore, in Experiment II the 20 Hz SF was adopted for data capture. As a result, all of the SFs meet the requirement.

Fourth, it is also important to note that range measurements of the thin plates were biased by range scattering error (Jamtsho and Lichti, 2010). Lichti et al. (2012) mentioned that the scattering error can be largely removed by the differencing operation if the scene structure does not change significantly from the zero-load state to the loaded state. This is a fundamental assumption that allows accurate deflection measurements to be made using

TOF-RC. In our case, since only the relative periodic motion is desired, the range bias due to scattering at each target location is of no consequence.

Fifth, systematic errors of the time-of-flight range camera impact the range measurement accuracy. Generally speaking, the systematic errors should be corrected by camera calibration. However, since only the relative, periodic motion is desired, the range bias due to systematic errors at each target location is of no consequence. Only very small changes in position were measured and the differential operation removed unmodelled systematic errors. In addition, the output of the SR4000 time-of-flight range camera is pre-calibrated by the manufacturer. Therefore, in our application, additional camera calibration was not considered.

4.3.3 Operation conditions of Kinect

During data capture, several factors should be considered as well. First, the Kinect LC-RC had been warmed up for one hour to obtain stable measurement data. Second, the depth resolution is a function of distance between the cameras and the object. The depth resolution gets worse with increasing distance. The Kinect LC-RC was mounted in the scaffold assembly about 1.9 m where the absolute accuracy is ±10 mm according to the Table 4.2. After 2 m, the absolute accuracy decreases significantly. In our experiment, the maximum deflection of the concrete beam based on loading control is 4 mm. The very small changes in position were measured within ±10 mm. In addition, the differential operation can remove unmodelled systematic errors, which is similar with SR 4000 TOF-RC (Lichti et al., 2012). Therefore, the calibration of the Kinect LC-RC did not need to be considered.

4.4 The output images of range cameras

A potential advantage of the TOF-RCs is that intensity images and depth images are provided simultaneously and they are co-located to each other. An advantage of LC-RCs is

that RGB images and depth images are offered. Figure 4.3 illustrates the depth image from a time-of-flight based range camera from top view. Figure 4.4 shows the amplitude image captured by a TOF-RC from top view.

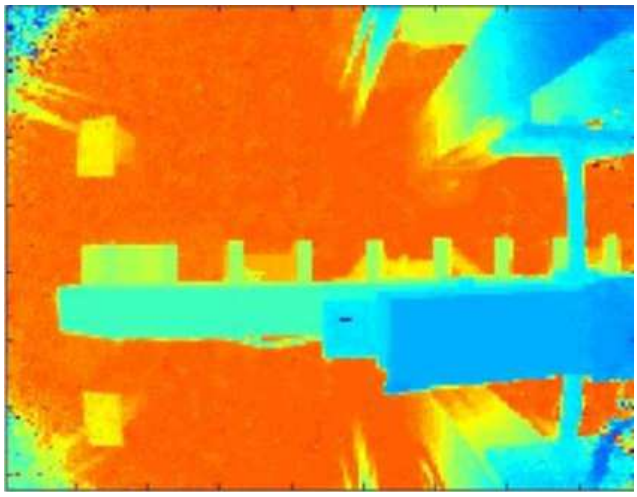

Figure 4.3: Range image of the Experiment scene (SR4000)

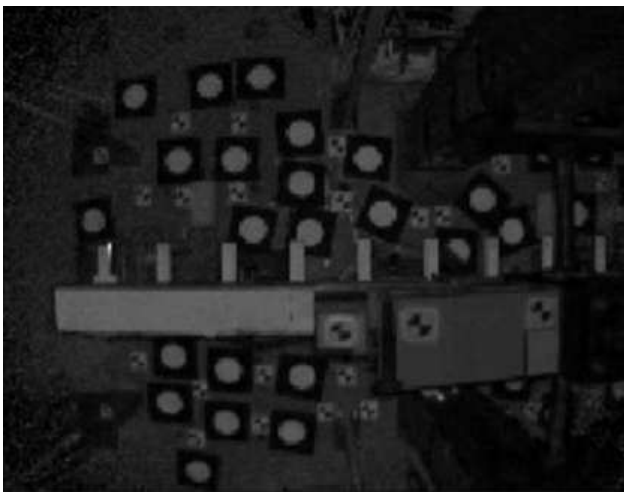

Figure 4.4: Amplitude image of the Experiment scene (SR4000)

However, a LC-RC exports a depth image and a RGB image, which come from two different types of cameras. Their field of view are not same. The two images are not co-located with each other. Figure 4.5 shows the depth image of the experiment scene captured by Kinect. Figure 4.6 gives a RGB image of the experiment scene captured by Kinect.

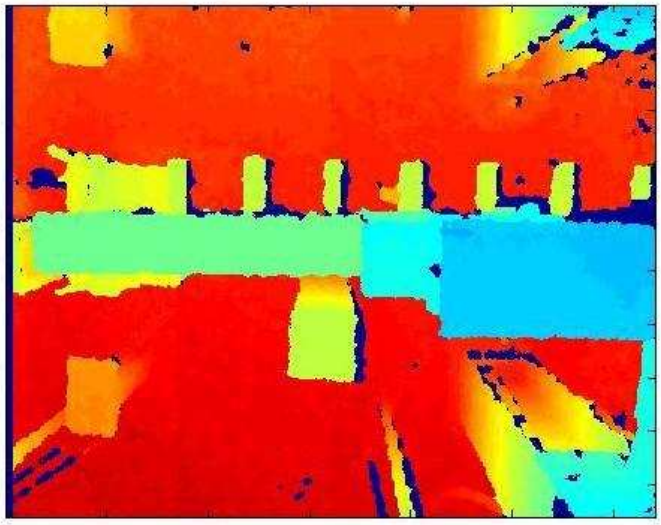

Figure 4.5: Range image of the Experiment scene (Kinect)

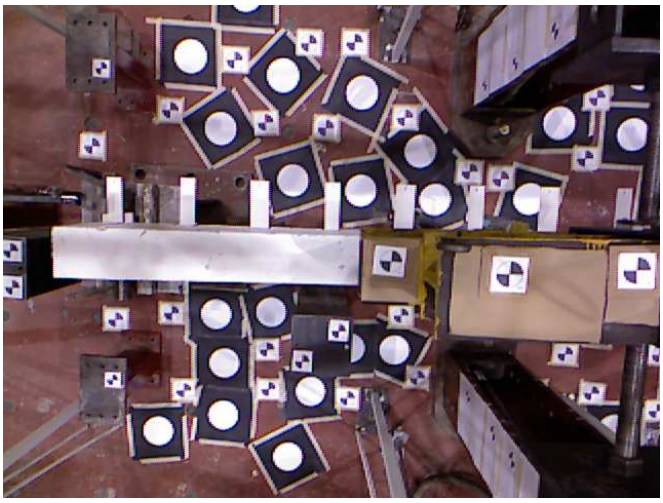

Figure 4.6: RGB image of the Experiment scene (Kinect)

4.5 Summary

This chapter presented the experimental design and practical experiment setup for the concrete beam deflection measurement. Then, different optical sensors were introduced such as SR4000 TOF-RCs, Kinect LC-RCs, LDSs and TLS. Many factors impacting the range measurement accuracy during data capture were presented such as warming up time, light

interference, choosing appropriate integration time for dynamic loading data capture and so on. The output of the two types of range cameras was also discussed. The key to using these cameras lies in the extraction of the target system from these images. That is treated in the next chapter.

Chapter 5

Range camera data processing

This chapter discusses the data preparation and image processing techniques needed to extract target objects from 3D point cloud of the RCs. Figure 5.1 shows the corresponding 3D point cloud of the dynamic deflection measurement experiment scene from one of the SR4000 TOF-RCs. Since a TOF-RC simultaneously provides co-located range and intensity images, both radiometric and depth information can be used to segment target objects. Therefore, by using 2D and 3D image processing technologies, the thin plates and the top beam surface of interest were extracted automatically.

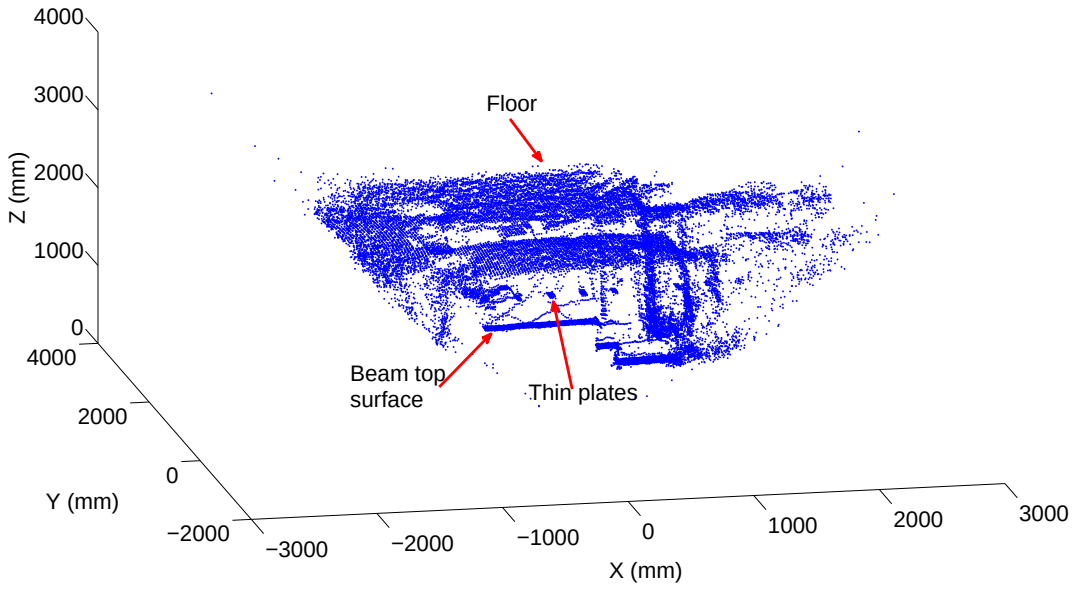

Figure 5.1: A SR4000 3D point cloud of the deflection measurement scene

Figure 5.2 shows a Kinect 3D point cloud of the deflection measurement scene. However, the RGB image and the depth image from the Kinect LC-RC are not co-located with each other. Therefore, another thin plate automatic extraction method is presented in this chapter.

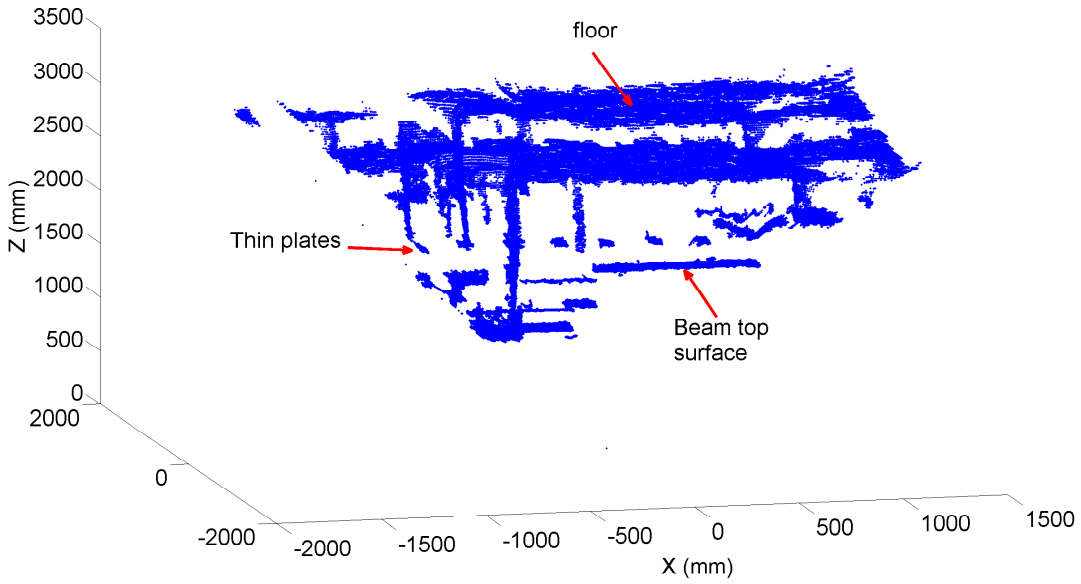

Figure 5.2: A Kinect 3D point cloud of the deflection measurement scene

In addition, a power spectral density (PSD) analysis method is described for unevenly sampled data. The loading frequency is recovered by PSD analysis. Linear and non-linear least squares are used to estimate the motion trajectory of the thin plates and to calculate the dynamic deflection of the concrete beam. Finally, the effects of the motion artefacts of a TOF-RC are described as well.

5.1 Thin plate point cloud extraction for SR4000

In this section, extracting the thin plate from 3D point cloud derived from a TOF-RC is discussed. Since the main objects of interest are the thin plates, their automatic extraction from the TOF-RC data requires specialized image processing techniques.

5.1.1 Depth-based classification

Depth-based classification is used to remove the floor and anything higher than the thin plates such as the hydraulic actuator, the spreader beam and the top surface of the concrete beam in the depth image because different objects are at different heights, which is critical to

determine depth thresholds to remove non-thin plate regions roughly in the intensity images. Several techniques are used to estimate two thresholds. First, image edge detection, ellipse detection and ellipse fitting are used to extract and measure circular targets on the floor. Then bilinear interpolation is used to determine the depth of the ellipse center that is called the first depth threshold. The first depth threshold is used to remove floor. The top surface of the concrete beam is a rectangular shape which is easy to segment. The depth between the TOF-RC and the top surface of the concrete beam is determined based on the top surface of the concrete beam segmentation. This depth is the second depth threshold. The second depth threshold is utilized to remove the hydraulic actuator, the spreader beam and the top surface of the concrete beam.

5.1.1.1 Image edge detection for intensity images

Since high contrast white circular targets on black paper are used to calculate the first depth threshold, a circular target centre measurement algorithm is necessary. The first step of the target centre measurement is to perform edge detection in order to isolate the circular targets. The Canny edge algorithm has three basic objectives (Gonzalez and Woods, 2008): the detected edges have to be as close as possible to true edges; the edges should be well localized, the distance between a point marked by Canny edge detection and the center of the true edges is as small as possible; and the detector should return a single edge for each true edge. Those three objectives are all essential for precision and accuracy of the target measurement. Therefore, the Canny algorithm is used for isolating the circular targets in this thesis and it consists of the following four steps (Gonzalez and Woods, 2008):

- Smoothing the input amplitude image with a Gaussian filter;
- Finding the gradient magnitude images from input amplitude images;
- Applying the gradient magnitude images for maxima suppression;
- Using double thresholds and connectivity analysis to link edges.

Figure 5.3 shows the edge image for a dynamic experiment scene.

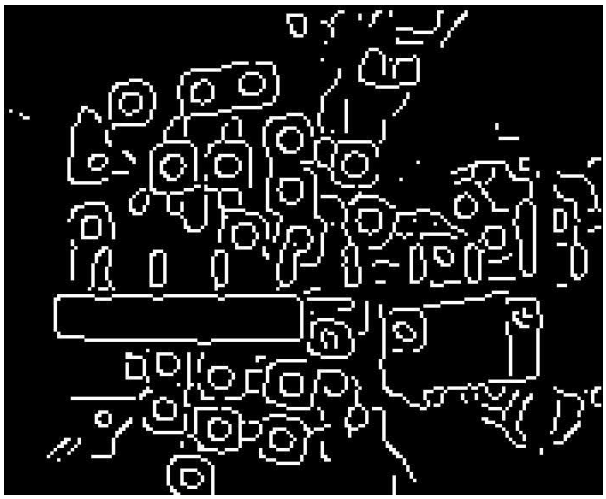

Figure 5.3: The edge image of the experiment scene with SR4000

5.1.1.2 Ellipse detection

After edge detection, the circular targets need to be detected. However, a circular target is projected onto the image plane approximately as an ellipse in the case that the target and the image planes are not parallel. Thus, ellipse detection with fake eccentricity of each connected region in the edge image (Rohs, 2004) is used in this thesis.

First of all, the connected regions cluster algorithm (Blackledge, 2005) is applied to the edge image for segmenting each connected region for further examination. For clustering one connected region, this algorithm first chooses a white pixel as a seed point. Starting from this seed point, each pixel of the rest of the connected region is tracked recursively by analyzing the pixels of the eight-neighborhood. Then, the fake eccentricity is defined as the ratio of the semi-minor axis $A_{ellipse}$ and the semi-major axis $B_{ellipse}$. If the fake eccentricity is close to one, the corresponding connected region has an ellipse-like shape (Rohs, 2004). Therefore, by estimating the fake eccentricities of all the connected regions, the ellipse target can be detected from the image. The fake eccentricities are derived from the second-order

moments of the connected regions (Rohs, 2004) with Equations 5.1 and 5.2.

$$A_{ellipse} = [(a+c) + \sqrt{(a+c)^2 - 4(ac - c^2)}] * 0.5 \tag{5.1}$$

$$B_{ellipse} = [(a+c) - \sqrt{(a+c)^2 - 4(ac - c^2)}] * 0.5 \tag{5.2}$$

$$au^2 + 2buv + cv^2 = 1 \tag{5.3}$$

$$\begin{bmatrix} a & b \\ b & c \end{bmatrix} = \frac{1}{4\mu_{uu}\mu_{vv} - \mu_{uv}^2} \begin{bmatrix} \mu_{vv} & -\mu_{uv} \\ -\mu_{uv} & \mu_{uu} \end{bmatrix} \tag{5.4}$$

$$\mu_{uu} = \frac{1}{|R|} \sum_{(u,v)\in R} (u - \bar{u})^2 \tag{5.5}$$

$$\mu_{vv} = \frac{1}{|R|} \sum_{(u,v)\in R} (v - \bar{v})^2 \tag{5.6}$$

$$\mu_{uv} = \frac{1}{|R|} \sum_{(u,v)\in R} (u - \bar{u})(v - \bar{v}) \tag{5.7}$$

$$\bar{u} = \frac{1}{|R|} \sum_{(u,v)\in R} u \tag{5.8}$$

$$\bar{v} = \frac{1}{|R|} \sum_{(u,v)\in R} v \tag{5.9}$$

where (u, v) are the pixel coordinates of a pixel point in the image; R is the pixel point set of the connected region; $|R|$ is the number of pixels of the connected region; $(\bar{u}, \bar{v})$ are the centroid of the connected region; μ_{uu}, μ_{vv} and μ_{uv} are the second moments of the connected region.

5.1.1.3 Target centre estimation

In this section, the centres of target ellipses are estimated by using the algorithm proposed in Fitzgibbon et al. (1999).

An ellipse is a special conic under certain conditions. It is well known that the general equation of a conic can be represented as

$$F(\vec{U}, \vec{X}) = \vec{U} \cdot \vec{X} = au^2 + buv + cv^2 + du + ev + f = 0 \tag{5.10}$$

where $\vec{U} = [a, b, c, d, e, f]^T$ is the coefficient (parameter) vector and $\vec{X} = [u^2, uv, v^2, u, v, 1]^T$.

If a constraint inequality (Equation (5.11)) is imposed on the above general conic equation

$$b^2 - 4ac < 0, \tag{5.11}$$

then we obtain an ellipse equation. Thus the following system represents an ellipse:

$$\begin{cases} F(\vec{U}, \vec{X}) = au^2 + buv + cv^2 + du + ev + f = 0, \\ b^2 - 4ac < 0. \end{cases} \tag{5.12}$$

For a pixel point (u_i, v_i), $F(\vec{U}, \vec{X}_i)$ can be treated as an "algebraic distance" between (u_i, v_i) and ellipse (5.12), where $\vec{X}_i = [u_i^2, u_i v_i, v_i^2, u_i, v_i, 1]^T$.

As Fitzgibbon et al. (1999) mentioned, in general, the constraint inequality (5.11) is difficult to impose in the estimation procedure. It is realized that when $\vec{U}$ in (5.10) is replaced by any multiple non-zero scale $k\vec{U}$, $F(k\vec{U}, \vec{X})$ represents the same conic as $F(\vec{U}, \vec{X})$ does. Thus we are free to scale arbitrarily the coefficients of (5.10) by the same multiple. It is enough to consider a special case of (5.12) with $4ac - b^2 = 1$. Therefore the inequality constraint has been changed into an equality constraint by using scaling.

$$\begin{cases} F(\vec{U}, \vec{X}) = au^2 + buv + cv^2 + du + ev + f = 0, \\ 4ac - b^2 = 1. \end{cases} \tag{5.13}$$

Therefore, the centre of each connected region can be estimated by least-squares ellipse fitting technique (Fitzgibbon et al., 1999) using Equations (5.13). In order to understand the

least-squares fitting technique to estimate coefficients of each of the ellipse, it is important to introduce the following matrix language.

Let $D = [\vec{X}_1, \vec{X}_2, \cdots, \vec{X}_n]^T$, where $\vec{X}_i = [u_i^2, u_i v_i, v_i^2, u_i, v_i, 1]^T$, that is

$$D = \begin{bmatrix} {u_1}^2 & u_1 v_1 & {v_1}^2 & u_1 & v_1 & 1 \\ \vdots & \vdots & \vdots & \vdots & \vdots & \vdots \\ {u_i}^2 & u_i v_i & {v_i}^2 & u_i & v_i & 1 \\ \vdots & \vdots & \vdots & \vdots & \vdots & \vdots \\ {u_n}^2 & u_n v_n & {v_n}^2 & u_n & v_n & 1 \end{bmatrix}. \tag{5.14}$$

Since $4ac - b^2$ is a homogeneous quadratic form, we can express the equality constraint $4ac - b^2 = 1$ in matrix form as follows:

$$4ac - b^2 = \vec{U}^T C \vec{U} = 1 \tag{5.15}$$

where $\vec{U} = [a, b, c, d, e, f]^T$ and

$$C = \begin{bmatrix} 0 & 0 & 2 & 0 & 0 & 0 \\ 0 & -1 & 0 & 0 & 0 & 0 \\ 2 & 0 & 0 & 0 & 0 & 0 \\ 0 & 0 & 0 & 0 & 0 & 0 \\ 0 & 0 & 0 & 0 & 0 & 0 \\ 0 & 0 & 0 & 0 & 0 & 0 \end{bmatrix}. \tag{5.16}$$

The sum of squared algebraic distances can be formulated in matrix form as

$$E = \sum_{i=1}^{n} F(\vec{U}, \vec{X}_i)^2 = (D\vec{U})^T (D\vec{U}) = ||D\vec{U}||^2. \tag{5.17}$$

Thus the ellipse fitting problem reduces to a constrained minimization problem Fitzgibbon et al. (1999)

$$\begin{cases} \text{minimize} \quad E = ||D\vec{U}||^2 = (D\vec{U})^T (D\vec{U}) \\ \text{subject to the constraint} \quad \vec{U}^T C \vec{U} = 1, \end{cases} \tag{5.18}$$

where D is an $n \times 6$ matrix, which is called *design matrix*, and C is a 6×6 matrix as defined above.

The classical Lagrange multiplier method can be used to obtain the minimum value of E. The Lagrange function is defined by

$$H(\vec{U}, \lambda) = (D\vec{U})^T(D\vec{U}) - \lambda(\vec{U}^T C\vec{U} - 1) \tag{5.19}$$

Differentiating $H(\vec{U}, \lambda)$ with respect to $\vec{U}$ and λ, gives

$$\begin{cases} 2D^T D\vec{U} - 2\lambda C\vec{U} = 0 \\ \vec{U}^T C\vec{U} = 1 \end{cases} \tag{5.20}$$

The may be rewritten as an equation system

$$\begin{cases} S\vec{U} = \lambda C\vec{U} \\ \vec{U}^T C\vec{U} = 1 \end{cases} \tag{5.21}$$

where $S = D^T D$ is the scatter matrix. This system is readily solved by considering the generalized eigenvectors of the first equation in (5.21).

The linear algebra algorithms were used to determine the eigenvalues-eigenvector pairs of the matrix S and the vector $\vec{U}$ is derived using the eigenvalues-eigenvector pairs (Fitzgibbon et al., 1999). The 2D coordinates of ellipse centres are determined based on the vector $\vec{U}$. The 3D coordinates of each ellipse centre can be determined by the 2D coordinates of each ellipse centre using the bilinear interpolation algorithm. The average value of the depth measurements (Z-coordinates) of each ellipse centre is seen as the first threshold.

5.1.1.4 Top surface of the concrete beam extraction

The top surface of the concrete beam is rectangular on shape which is easy to segment by the fake eccentricity algorithm since the fake eccentricity of the top surface is close to zero. The depth between the TOF-RC and the top surface of the concrete beam is determined based on the depth values of the top surface.

In depth images, if the depth value of each pixel is bigger than or equal to the first threshold, its intensity value of the corresponding pixel is set at zero. Moreover, if the depth value of each pixel is less than or equal to the second threshold, the intensity value of the corresponding pixel is set at zero. Therefore, the intensity image contrast is improved, which is useful for thin plate extraction. Using the first threshold and the second threshold, preliminary segmentation is done. Figure 5.4 shows the intensity image after the depth-based classification.

Figure 5.4: The result with depth-based classification (SR4000)

5.1.2 Otsu method for thin plate segmentation

A binary image can be obtained from an intensity image with image threshold estimated by the Otsu method (Otsu, 1979). The Otsu algorithm is discussed briefly in this thesis because it is used for segmenting the background and foreground in the intensity image.

By estimating a threshold using maximum between class variance, the weighted intra-class variance, defined as a weighted sum of variances of two classes (Equation 5.23) is minimized. Assume, there are L gray levels $[1, 2, 3, \ldots, i, \ldots, L-2, L-1, L]$ for an intensity image from TOF-RC. The number of pixels at level i is noted by n_i and the total number of pixels by $N = n_1 + n_2 + \ldots, +n_L$. Therefore, the gray level histogram is normalized as

follows.

$$p_i = \frac{n_i}{N} \tag{5.22}$$

An intensity image is divided into two classes $C_0 = [1, \ldots, k]$ and $C_1 = [k+1, \ldots, L]$ by a threshold k. The within class variance $\sigma_w^2(k)$ is given by Equation (5.23).

$$\sigma_w^2(k) = \omega_0 \sigma_0^2 + \omega_1 \sigma_1^2 \tag{5.23}$$

where, weights $\omega_0 = \sum_{i=1}^{k} p_i$ and $\omega_1 = \sum_{i=k+1}^{L} p_i$ are probabilities of the two classes separated by a threshold k; σ_0^2 and σ_0^2 are the variances of the two classes.

However, Otsu (1979) reported that minimizing the within-class variance is equal to maximizing between-class variance $\sigma_b^2(k)$.

$$\sigma_b^2(k) = \frac{[\mu_T \omega(k) - \mu(k)]^2}{\omega(k)[1 - \mu(k)]} \tag{5.24}$$

where μ_T is the expected value of the intensity image; $\omega(k)$ is equal to ω_0 and $\mu(k)$ is the first class expected value.

Therefore, the optimal threshold k_o can be determined by maximizing the between-class variance $\sigma_b^2(k)$. Figure 5.5 shows the binary image of Figure 5.4.

Figure 5.5: The binary image based on Otsu threshold method (SR4000)

5.1.3 Fake eccentricity for thin plate classification

There are some non-thin plate connected regions in the binary image shown in Figure 5.6. It is necessary to remove the regions.

Since each thin plate region has a similar shape and size, the fake eccentricities of those desired regions should have almost similar values within close proximity. Therefore, fake eccentricity calculated by second moments is used to classify thin plates from unwanted regions (Rohs, 2004). Figure 5.6 illustrates the result after removing non-thin plate regions of Figure 5.6 with the fake eccentricity algorithm.

Figure 5.6: The result after thin plate segmentation (SR4000)

5.1.4 Image erosion algorithm for mixed pixel removing

The boundaries of the thin plates were removed with the image erosion algorithm because mixed pixels (Dorrington et al., 2011) occur frequently at edges of the thin plates. They are caused by the superposition of the foreground and background reflected signals. The image erosion algorithm (Gonzalez and Woods, 2008) can be used to remove the edges of the thin plates. The method removes unwanted noisy points from edges of the thin plates. Figure 5.7 illustrates the final result after removing edges of the thin plates. The centroid of each thin plate can be calculated by averaging all point cloud belonging to each thin plate.

Figure 5.7: The result after image erosion (SR4000)

5.1.5 3D point cloud of the thin plates from SR4000

Figure 5.8 shows the 3D point cloud of the thin plates by using the thin plate extraction techniques mentioned previously.

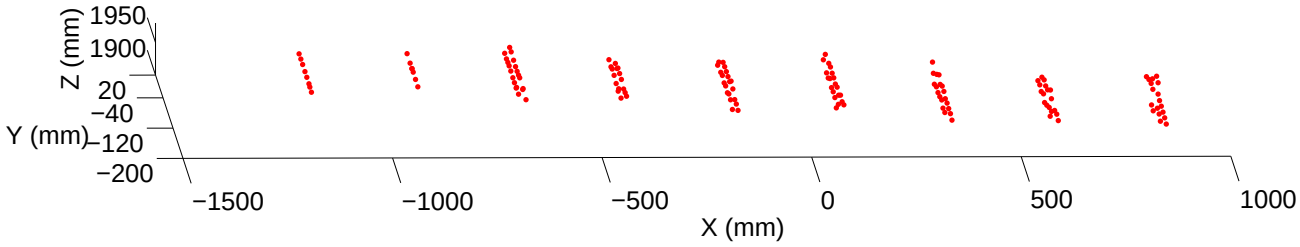

Figure 5.8: 3D point cloud of the thin plate

The range camera can provide three dimensional measurements: the lateral direction (i.e. Y-coordinate), the longitudinal direction (i.e. X-coordinate) and the vertical direction (i.e. Z-coordinate). Based on direction of the periodic force, the thin plates move toward vertical, longitudinal and lateral directions during the fatigue test experiment. However, even though the thin plates do move towards lateral direction (Y-coordinate), Y-coordinate can be still used to judge robustness of the thin plate point extraction techniques.

In order to prove the robustness, two data sets with five hundred frames were analyzed. Figures 5.9 and 5.10 show Y-coordinates of a thin plate vs time serials of the two data sets. As can be seen, the maximum Y-coordinate of the first data set is -47.03 mm and the minimum Y-coordinate of the first data set is -47.39 mm. The difference in the first data set is -0.36 mm. The maximum Y-coordinate of the second data set is -47.03 mm and the minimum Y-coordinate of the second data set is -47.35 mm. The difference in the second data set is -0.32 mm. The periodic motion can be seen in Figures 5.9 and 5.10. The mean value of the periodic displacements is constant over time. As a result, the thin plate extraction and centroid calculation method are robust.

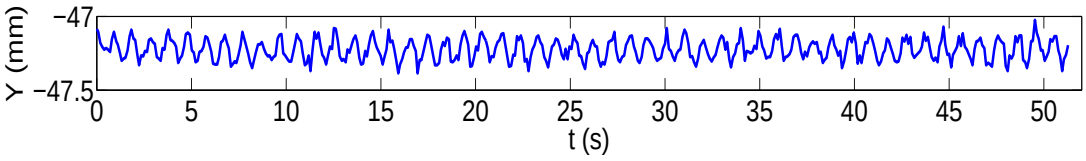

Figure 5.9: Y-coordinates of a thin plate vs time-1 Hz

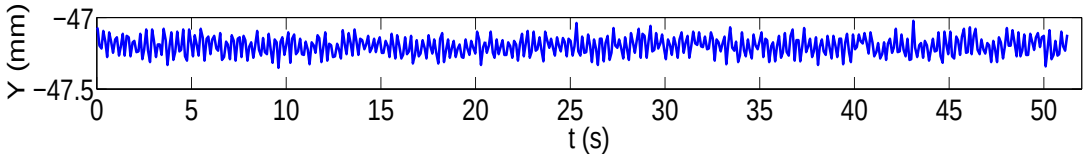

Figure 5.10: Y-coordinates of the thin plate vs time-3 Hz

5.2 Thin plate point cloud extraction for Kinect

5.2.1 Procedure of thin plate extraction for Kinect

A Kinect LC-RC was also used to acquire measurement data of the dynamic concrete beam experiment. So, an automatic point cloud extraction technique for the Kinect measurement

data was developed as well. The depth sensor of Kinect is able to return a depth image. The RGB sensor of the Kinect is able to return an RGB image just like traditional digital cameras. However, unfortunately, the two images are not co-located and their fields of view are different. Therefore, the two images do not capture the same scenes.

In this thesis, only the depth image is used to extract the thin plates because of the non-co-located problem. Depth-based classification was first applied for preliminary segmentation. Depth-based segmentation based on two thresholds manually choosing was used to remove the floor and other objects higher than the thin plates. A binary image was created by using the depth-based segmentation as shown in Figure 5.11.

Figure 5.11: The binary image after depth-based segmentation (Kinect)

Second, since each thin plate region has similar shape and size, fake eccentricities of those desired regions have similar values within close proximity. Therefore fake eccentricities calculated by second moments of connected regions are used to distinguish the thin plates from unwanted regions (Rohs, 2004). In addition, the 2D image coordinates of the thin plate centroids showing on the co-located binary image should lie on a line. Therefore, line fitting is used to remove the unwanted regions. Then, image erosion was used to remove the edges of the thin plates. Moreover, region growing (Rabbani et al., 2006) was used to remove the

3D point cloud that do not belong to any thin plate. Figure 5.12 shows the final result of the thin plate extraction as a binary image. The centroid of each thin plate was calculated by averaging all 3D point cloud belonging to each thin plate. Bearing plate on top of the cylinder is the problem so the extracted thin plate is not rectangular. However, this thin plate was not used to analyze the deflection of the concrete beam. Therefore the deflection results were not impacted by this thin plate.

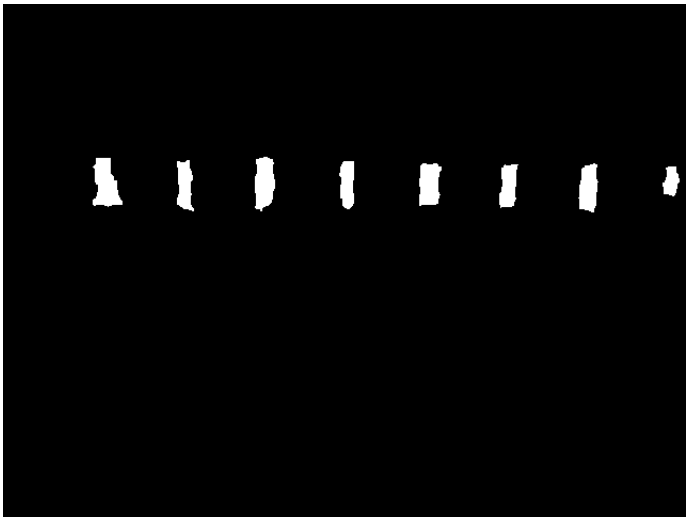

Figure 5.12: Final result of the thin plate extraction (Kinect)

5.2.2 3D point cloud of the thin plates with Kinect

The 3D point cloud derivation was discussed in Section 3.4. Figure 5.13 shows 3D point cloud of the thin plates from Kinect LC-RCs by using the thin plate extraction procedure described above.

In order to validate the robustness of the thin plate point cloud extraction procedure for Kinect LC-RCs, the two data sets with around four hundred frames were analyzed as well. Y-coordinate vs time series are plotted in Figure 5.14 and Figure 5.15. As can be seen, the maximum Y-coordinate of the first data set is -227.01 mm and the minimum Y-coordinate of the first data set is -232.46 mm. The difference in the first data set is -5.45 mm. The mean value of the first data set is -229.81 mm. The STD is 0.92 mm. The maximum Y-coordinate

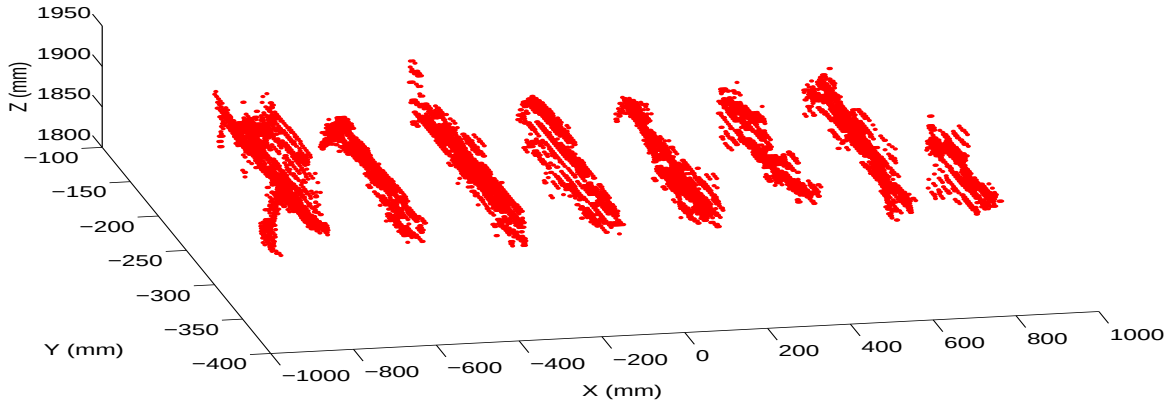

Figure 5.13: The 3D point cloud (Kinect)

of the second data set is -230.28 mm and the minimum Y-coordinate of the second data set is -236.60 mm. The difference in the second data set is -6.32 mm. The mean value of the second data set is -233.62 mm. The STD is 0.94 mm. Andersen et al. (2012) presented that the absolute accuracy is roughly 40 mm at 2 m distance. The standoff distance between the cameras and the concrete beam is around 2 m. The maximum distance difference of each data set is less than the measurement precision mentioned in (Andersen et al., 2012), as a result, the thin plate extraction and centroid calculation method is robust.

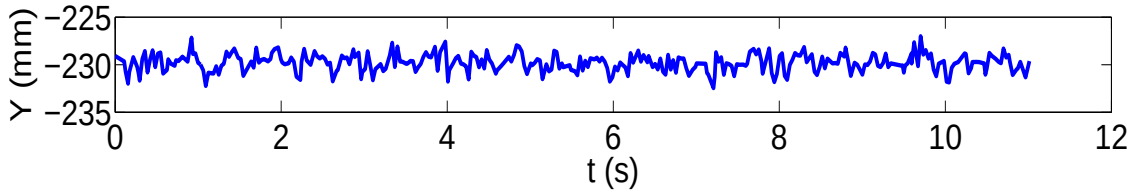

Figure 5.14: Y-coordinates of a thin plate vs time serials-1 Hz (Kinect)

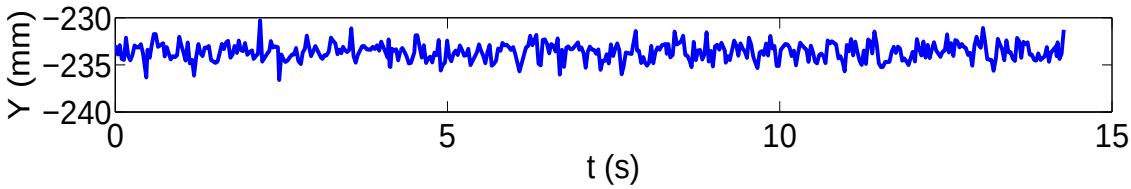

Figure 5.15: Y-coordinates of a thin plate vs time serials-3 Hz (Kinect)

5.3 Displacement measurement from range camera data

5.3.1 Power spectral density analysis

In the beam deflection experiment, the motion of the thin plate centroid is ideally a sinusoidal waveform. The sinusoidal waveform can be analyzed easily in the frequency domain from which the approximate signal frequency and amplitude can be derived. Therefore, spectral analysis methods were used to analyze the thin plate centroid data. Although the range camera time series were uniformly sampled, some random drop-outs occurred frequently, which is called the missing data problem.

There are a few ways to deal with the uneven sampling or the missing data problem. Interpolation is one method. A grid of an even time interval for the observation data is specified and the missing values are interpolated from the original measurement data on the grid. Sometimes the missing data are set at zeros or set at fixed values based on the time series data. The interpolated observation data are analyzed by using the Fast Fourier Transform method. However, if a lot of consecutive points are missing, in general, such techniques perform poorly to analyze the measurement data in the frequency domain.

A totally different method of spectral analysis for unevenly sampled data is used in this thesis that can mitigate these kind of problems caused by the missing data problem. Lomb's method (Press et al., 1992) considers data only at time t_i that are actually sampled, which means the spectral density analysis of Lomb method is based on discrete sample points. Suppose that there are N samples $h_i = h(t_i), i = 0, \ldots, N-1$ and their mean and variance are shown in Equations 5.25 and 5.26 respectively.

$$\bar{h} = \frac{1}{N} \sum_{i=0}^{N-1} h_i \tag{5.25}$$

$$\sigma^2 = \frac{1}{N-1} \sum_{i=0}^{N-1} (h_i - \bar{h})^2 \tag{5.26}$$

The Lomb normalized periodogram (spectral power density as a function of angular frequency

$\omega = 2\pi f_0 > 0$) is defined as follows

$$P_N(\omega) = \frac{1}{2\sigma^2}[\frac{[\sum_j (h_j - \bar{h}) \cos \omega(t_i - \tau)]^2}{\sum_j \cos^2 \omega(t_i - \tau)} + \frac{[\sum_j (h_j - \bar{h}) \sin \omega(t_i - \tau)]^2}{\sum_j \sin^2 \omega(t_i - \tau)}] \tag{5.27}$$

$$\tan(2\omega\tau) = \frac{\sum_j \sin 2\omega t_j}{\sum_j \cos 2\omega t_j} \tag{5.28}$$

where τ is defined by Equation 5.28 and it is a kind of offset.

Lomb (Press et al., 1992) investigated that the coefficients of the harmonic equation can be estimated by an observation data set at a given frequency ω by linear least-square fitting to the harmonic model 5.29. The angular frequency ω can be determined by Equation 5.27.

$$h(t) = C \cos \omega t + D \sin \omega t + E \tag{5.29}$$

The measurements of the thin plates are the sum of a periodic signal and white Gaussian noise. Thus, spectral analysis of the unevenly sampled data was conducted with the Lomb method (Press et al., 1992). The approximate loading frequency can be estimated by using the power spectral density (PSD) analysis of depth measurements. Figure 5.16 shows the power spectral density as a function of the frequency of the thin plate centroid measurements with the Lomb method. $\alpha = [0.001, 0.005, 0.01, 0.05, 0.1, 0.5]$ are the statistical significance levels. In order to see the significance levels clearly, only two levels are shown in Figure5.16. As can be seen, there is one dominant peak in the power spectrum above $\alpha = 0.001$, which shows that there is sinusoidal component in the signal (Press et al., 1992). If there is no dominant peak above $\alpha = 0.5$ statistical significance level, which means that there is noise component in the signal. By searching for a peak of the power spectrum density, the corresponding frequency is determined, which means the approximate loading frequency is derived.

With the recovered approximate loading frequency, the approximate coefficients C, D, E of the harmonic model (Equation 5.29) of the thin plate trajectory can be estimated by using

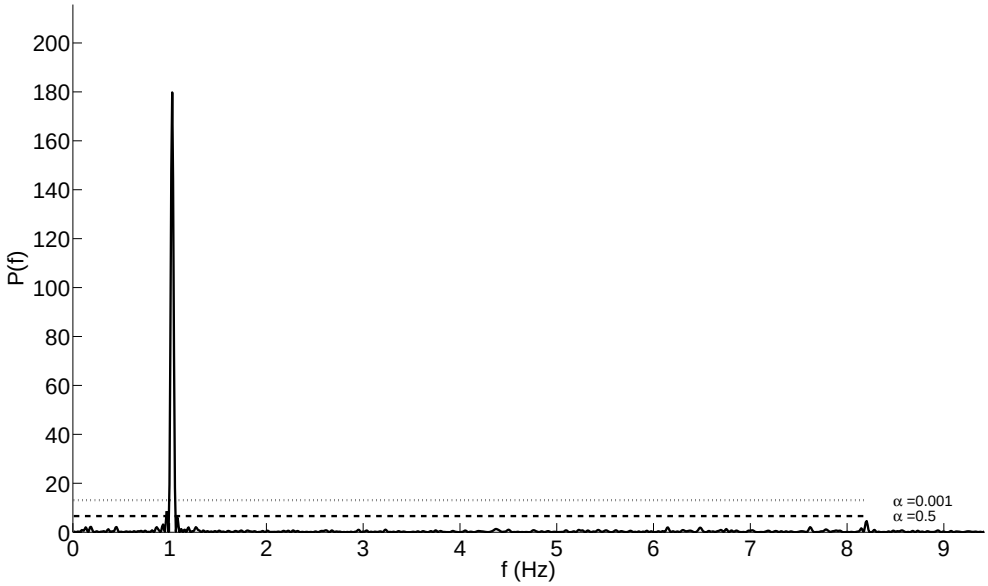

Figure 5.16: An example of PSD of thin plate centroid observations based on Lomb method

linear least-squares. Then the coefficients C, D, E, ω of the harmonic can be estimated with non-linear least-squares by using approximate coefficients C, D, E, ω as initial values. The amplitude A and the load frequency f_0 were calculated by using Equations 5.30 and 5.31 respectively.

$$A = \sqrt{C^2 + D^2} \tag{5.30}$$

$$f_0 = 2\pi\omega \tag{5.31}$$

5.3.2 Linear least-squares estimation

Linear least-squares is described briefly in this thesis. The general observation model can be expressed as Equation 5.32. If the observation model is linear, Equation 5.32 can be described using Equation 5.33.

$$\mathbf{z} = g(\mathbf{x}) + \mathbf{v} \tag{5.32}$$

$$\mathbf{z} = G\mathbf{x} + \mathbf{v} \tag{5.33}$$

where G is the design matrix; $\mathbf{v}$ is the vector of random errors and $\mathbf{z}$ is the set of the measurements. In our case, the set of measurements are the depth measurements of the thin plate centroids. $\mathbf{x} = [C, D, E]$ is the unknown vector. The design matrix (Equation 5.34) is as follows

$$G = \begin{bmatrix} cos(\omega t_1) & sin(\omega t_1) & 1 \\ \vdots & \vdots & \vdots \\ cos(\omega t_i) & sin(\omega t_i) & 1 \\ \vdots & \vdots & \vdots \\ sin(\omega t_N) & cos(\omega t_N) & 1 \end{bmatrix} \tag{5.34}$$

The unknown vector can be estimated by using Equation 5.35.

$$\hat{\mathbf{x}} = (G^T R^{-1} G)^{-1} G^T R \mathbf{z} \tag{5.35}$$

where R is observation covariance matrix $R = diag(\sigma_{z1}^2, \sigma_{z2}^2, \cdots, \sigma_{zn}^2)$.

5.3.3 Least-squares estimation with a linearized model

In our case, the trajectory of the thin plates model is a harmonic which is non-linear when the frequency is estimated as well, so all the coefficients of the harmonic model $\mathbf{x} = [C, D, E, \omega]$ should be estimated. In order to handle this kind of a non-linear model, Taylor series expansion can be used (Cheney and Kincaid, 2007).

$$\begin{aligned} \mathbf{z} = g(\mathbf{x}) + \mathbf{v} = g(\hat{\mathbf{x}}) + \frac{dg(\mathbf{x})}{d\mathbf{x}}|_{\mathbf{x}=\hat{\mathbf{x}}}(\mathbf{x} - \hat{\mathbf{x}}) + \frac{1}{2!}\frac{d^2 g(\mathbf{x})}{d\mathbf{x}^2}|_{\mathbf{x}=\hat{\mathbf{x}}}(\mathbf{x} - \hat{\mathbf{x}})^2 + \cdots + \mathbf{v} \\ \approx g(\hat{\mathbf{x}}) + \frac{dg(\mathbf{x})}{d\mathbf{x}}|_{\mathbf{x}=\hat{\mathbf{x}}}(\mathbf{x} - \hat{\mathbf{x}}) + \mathbf{v} \end{aligned} \tag{5.36}$$

where $\delta\mathbf{x} = \mathbf{x} - \hat{\mathbf{x}}$ is the difference between the estimation and approximate value of the unknown vector.

Only the zero and first order terms are retained so the Taylor series expansion (Equation 5.36) is simplified to a linear equation as follows.

$$\mathbf{z} = g(\hat{\mathbf{x}}) + G\delta\mathbf{x} + \mathbf{v} \tag{5.37}$$

$$\delta \mathbf{z} = \mathbf{z} - g(\hat{\mathbf{x}}) = G\delta\mathbf{x} + \mathbf{v} \tag{5.38}$$

where $\delta\mathbf{z}$ is called the measurement misclosure vector; $\mathbf{z}$ is the observation measurement of the thin plate centroid from different range cameras; $\mathbf{x}$ is the coefficients of the model $[C, D, E, \omega]$ which are called unknowns and $g(\hat{\mathbf{x}})$ is the predicted observations.

By calculating the correction $\delta\hat{\mathbf{x}}$ in Equation 5.39, the difference between the approximated and true values of the unknown vector is derived.

$$\delta\hat{\mathbf{x}} = (G^T R^{-1} G)^{-1} G^T R^{-1} \delta\mathbf{z} \tag{5.39}$$

where R is the observation covariance matrix $R = diag(\sigma_{z1}^2, \sigma_{z2}^2, \cdots, \sigma_{zn}^2)$ and G is the design matrix that is the partial derivatives of the functional model with respect to the unknowns.

$$G = \begin{bmatrix} \cos(\omega t_1) & \sin(\omega t_1) & 1 & -Ct_1 \sin(\omega t_1) + Dt_1 \cos(\omega t_1) \\ \vdots & \vdots & \vdots & \vdots \\ \cos(\omega t_i) & \sin(\omega t_i) & 1 & -Ct_1 \sin(\omega t_i) + Dt_1 \cos(\omega t_i) \\ \vdots & \vdots & \vdots & \vdots \\ \cos(\omega t_N) & \sin(\omega t_N) & 1 & -Ct_1 \sin(\omega t_N) + Dt_1 \cos(\omega t_N) \end{bmatrix} \tag{5.40}$$

The difference between the approximate and estimated values of the unknown vector are applied to the current estimates of the unknowns by using iteration to estimate the best coefficients of the model. For the iteration, the initial values of the unknowns are denoted $\hat{\mathbf{x}}_0$ and the estimated corrections are denoted $\delta\hat{\mathbf{x}}_0$. The new estimates are stated as $\hat{\mathbf{x}}_1 = \hat{\mathbf{x}}_0 + \delta\hat{\mathbf{x}}_0$. In general, non-linear least squares are shown as follows.

$$\hat{\mathbf{x}}_{k+1} = \hat{\mathbf{x}}_k + \delta\hat{\mathbf{x}}_k \tag{5.41}$$

The iteration process is continued until convergence is declared or a predefined number of iterations have occurred. Convergence is usually declared when the correction vector, $\delta\hat{\mathbf{x}}_k$, has elements that are sufficiently small such that the effect on the final solution is negligible.

5.3.4 Statistical testing

After calculating the concrete beam displacements from the measurement data of the range cameras, it is critical to evaluate the displacement measurement precision using statistical methods. There are several quantities of interest such as the covariance matrix of parameters, STDs of estimated parameters to assess the displacement measurement precision and the STDs of estimated residuals.

The correlation between coefficients of the model can be acquired from the covariance matrix of the estimated parameters $\hat{\mathbf{x}}$. Before calculating the covariance matrix, the estimated variance factor $\hat{\sigma}_0^2$ should be derived by using the estimated residuals and the observation variance matrix .

$$\hat{\sigma}_0^2 = \frac{\hat{r}^T R^{-1} \hat{r}}{n-4} \tag{5.42}$$

where, R is the observation covariance matrix; $\hat{r}$ is the estimated residuals; n is the number of samples and $n-4$ is degrees of freedom. The estimated residuals are calculated by $\hat{r} = G\hat{\delta\mathbf{x}} + \delta\mathbf{z}$.

Then, the covariance matrix of the estimated parameters is calculated by using Equation 5.43.

$$C_{\hat{\mathbf{x}}} = \hat{\sigma}_0^2 (G^T R^{-1} G)^{-1} \tag{5.43}$$

Using the covariance matrix of the estimated parameters, the STDs of the estimated parameters can be calculated. However, the deflection measurement is calculated by Equation $A = \sqrt{C^2 + D^2}$. The derivation of STD of the deflection measurement is discussed in this thesis. Given the expectations $E(\hat{C})$ and $E(\hat{D})$, the variance of the estimated deflections can be derived by Equation 5.44.

$$Var(A) = \alpha^T Cov(C, D) \alpha \tag{5.44}$$

$$\alpha = (\frac{E(\hat{C})}{\sqrt{E(\hat{C})^2 + E(\hat{D})^2}}, \frac{E(\hat{D})}{\sqrt{E(\hat{C})^2 + E(\hat{D})^2}}) \tag{5.45}$$

where, α is the vector; $Cov(C, D)$ is the covariance matrix of the estimated parameters $\hat{C}$ and $\hat{D}$; $Var(A)$ is the variance of the estimated amplitude.

The standard deviation of estimated residuals $\sigma_{\hat{r}}$ is called the standard error of estimates. It can be used to assess how well the fitted model fits the sample data and indicates the measurement precision of observation data. It can be derived by Equation 5.46.

$$\sigma_{\hat{r}} = \sqrt{\frac{\hat{r}^T \hat{r}}{n-4}} \tag{5.46}$$

5.4 Effects of motion artefacts of time-of-flight range cameras

The range imaging measurement principle assumes that the object is stationary during the four integration periods. However, when the target or the TOF-RC is moving during the four integration periods, each measurement in Equation 3.5 contains an additional time-dependent phase shift as shown in Equation 5.47, which leads the phase difference to be biased.

$$\begin{cases} \hat{C}(\tau_0) = \dfrac{K}{2} \cdot \cos(\varphi + \Delta\varphi_0) + B \\ \hat{C}(\tau_1) = -\dfrac{K}{2} \cdot \sin(\varphi + \Delta\varphi_1) + B \\ \hat{C}(\tau_2) = -\dfrac{K}{2} \cdot \cos(\varphi + \Delta\varphi_2) + B \\ \hat{C}(\tau_3) = \dfrac{K}{2} \cdot \sin(\varphi + \Delta\varphi_3) + B \end{cases} \tag{5.47}$$

where $\Delta\varphi$ is the time-dependent phase shift.

If the target motion is a sinusoidal curve, as is the case of the fatigue load testing, and the Z-axis of the 3D coordinate system is parallel with the gravity vector such that the motion is confined to the radial direction, then the periodic change in range is given by Equation

5.48. Therefore, the additional phase shift is shown in Equation 5.49:

$$\Delta\rho(t) = k \cdot \sin(2\pi f_0 t) \tag{5.48}$$

$$\Delta\varphi(t) = \frac{4\pi f_m}{c}\Delta\rho(t) \tag{5.49}$$

where k is the amplitude of the target motion; f_0 is the frequency of the target motion and c is speed of light.

Using Equations 5.48 and 5.49, the sampling measurement is thus given by Equation 5.50.

$$\hat{C}_i = \frac{K}{2} \cdot \cos(\varphi + \frac{\pi i}{2} + \frac{4\pi f_m}{c} k sin(2\pi f_0 t)) + B \tag{5.50}$$

With the four biased sampling measurements, the biased phase difference (Equation 5.51) is derived. Since the phase difference is biased, the range measurement is biased (Equation 5.52) as well. The impact of the target motion on the range measurements is assessed in Chapter 6 by simulation.

$$\hat{\varphi} = tan^{-1}(\frac{\hat{C}_3 - \hat{C}_1}{\hat{C}_0 - \hat{C}_2}) \tag{5.51}$$

$$\hat{\rho} = \frac{\hat{\varphi} c}{4\pi f_m} \tag{5.52}$$

5.5 Summary

This chapter presented range camera data processing. Extraction of the thin plates from the 3D point cloud of the object scene is essential for accurate measurement of the beam deflection. Therefore, different automatic extraction methods of the thin plates for different optical sensors were presented.

Depth-based classification was the basis for the thin plate extraction. Traditional 2D image processing algorithms were very useful to the automatic extraction of the thin plates.

The refined point cloud of the thin plates were used to compute the centroid of the thin plates. The centroid was used as the reference point of interest for measuring the displacement of the concrete beam.

Power spectral density analysis with the Lomb method on the raw measurement data of the thin plate centroid overcomes the missing data problem. Linear and non-linear least squares were used to estimate the loading frequency and the deflection amplitude with time series measurement data. Statistical methods were used to analyze the displacement measurement precision of the concrete beam.

Motion artefacts of TOF-RCs affect the dynamic deflection measurement accuracy. This chapter discussed the influence of motion artefacts when target motion is a sinusoidal wave. Based on the methodology mentioned in this chapter, the results for the concrete beam are derived. In the next chapter, the results and analysis of the concrete beam deflection are presented.

Chapter 6

Results and analysis

This chapter presents the results and analysis of the deflection measurement for a concrete beam subjected to dynamic loading observed by two different optical sensors: TOF-RCs and LC-RCs. First, the simulation results for the concrete beam motion are described in Section 6.1. Second, the analysis of Experiment I and Experiment II is conducted. Section 6.2 presents the data analysis for the measurements derived from the SR4000 range cameras set at different SFs during Experiment I. Section 6.3 describes the analysis of dynamic concrete beam from a SR4000 TOF-RC and a Kinect LC-RC during Experiment II. In Section 6.3, the vertical deflection, longitudinal, and lateral displacements of the concrete beam are presented. The ability of Kinect LC-RCs to measure the dynamic deflection is also investigated. The results derived from LDS are used as a benchmark to evaluate absolute accuracy of the different sensors.

6.1 Simulation analysis of motion artefacts

The measurement principle of TOF-RCs assumes that the sensor and the target object are stationary during the four integration times. Motion artefacts occur as a result of the object target or the sensor motion during data capture. Ideally the trajectory of the thin plate motion is a sinusoidal curve. Therefore, during the dynamic beam experiment, the impact of the motion artefacts should be analyzed since the concrete beam was subjected to periodic loads with 1 Hz or 3 Hz loading frequency and a 4 mm amplitude. So, in this section, a target experiencing sinusoidal motion with the 1 Hz or 3 Hz frequency and the 4 mm amplitude was numerically simulated.

Figures 6.1, 6.2, 6.3 and 6.4 illustrate the simulated true and biased ranges ρ for de-

flection along with their time stamps using the four different SFs when the target motion frequency is 1 Hz. The true range represents the range derivation using the time-of-flight measurement principle without considering the motion artefacts. The biased range denotes the range derivation using the time-of-flight measurement principle by considering the motion artefacts. As can be seen, the amplitude difference between them is small but there is a significant temporal phase difference between the true and biased signals. The biggest temporal phase difference by calculating the true and biased signal phase is $-13.2°$ with 1 Hz motion frequency and 10 Hz SF, but it is of no consequence since it does not impact the amplitude measurement accuracy which is of prime importance (Qi and Lichti, 2012a,b).

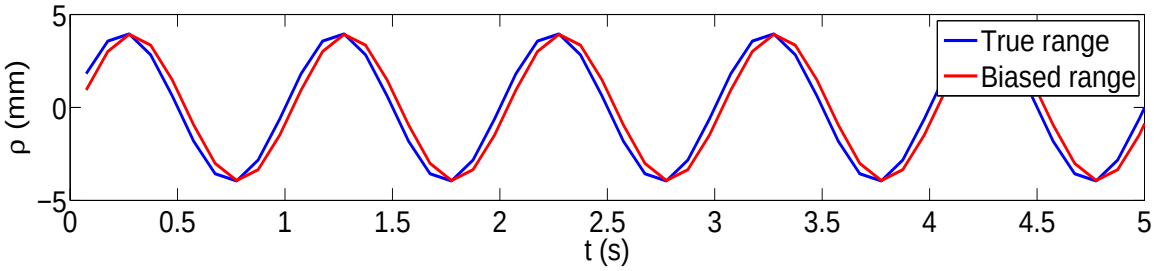

Figure 6.1: Simulated true and biased ranges vs time ($f_0 = 1$ Hz and $f_s = 10$ Hz)

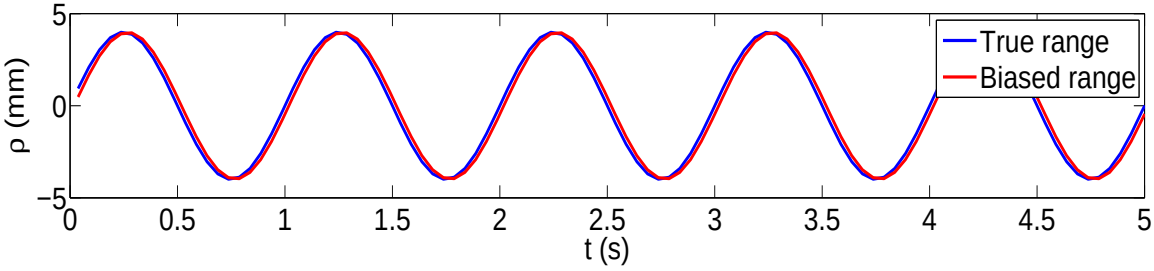

Figure 6.2: Simulated true and biased ranges vs time ($f_0 = 1$ Hz and $f_s = 20$ Hz)

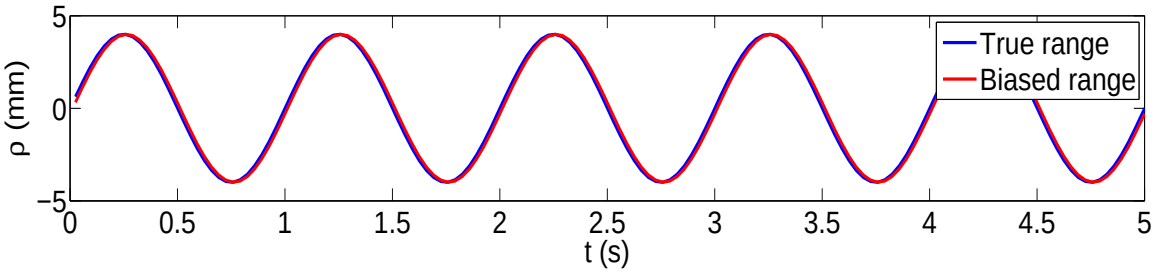

Figure 6.3: Simulated true and biased ranges vs time ($f_0 = 1$ Hz and $f_s = 30$ Hz)

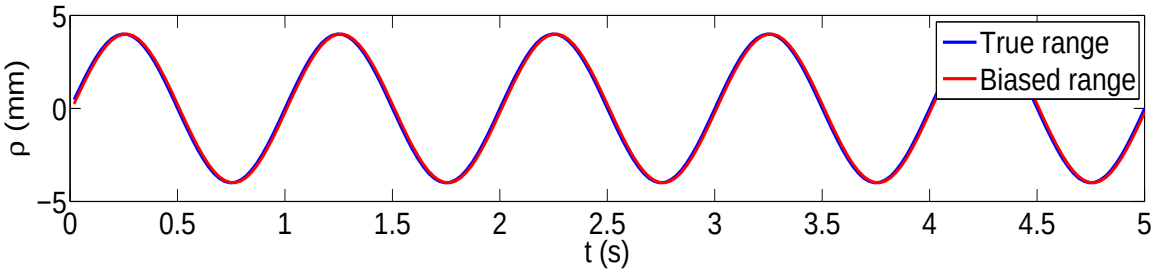

Figure 6.4: Simulated true and biased ranges vs time ($f_0 = 1$ Hz and $f_s = 40$ Hz)

Figures 6.5, 6.6, 6.7 and 6.8 show the true and biased ranges along with their time stamps using the different SFs (i.e. 10 Hz, 20 Hz, 30 Hz and 40 Hz) while the target motion frequency is 3 Hz. As can be seen, the trajectories of the target motion are sinusoidal waveforms except for at 10 Hz SF. The sinusoidal waveform is significantly distorted when the SF is 10 Hz. When the SF is 20 Hz, the trajectories of the target motion better resemble a sinusoidal waveform. However, we can still see the differences such as the phase difference and the amplitude difference. For the other two SFs, we can only see very small differences between the true and biased signals.

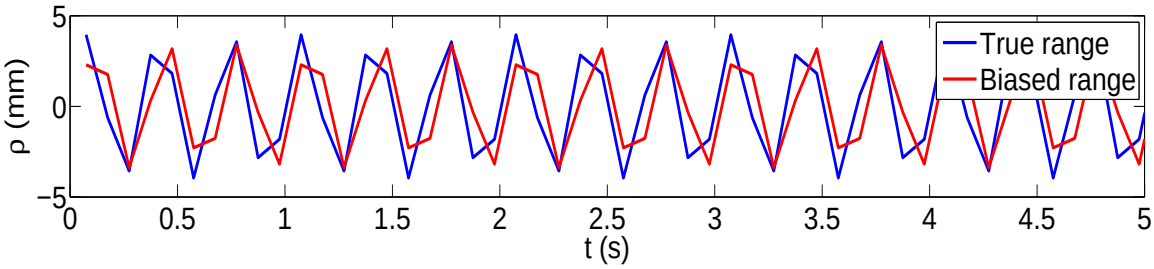

Figure 6.5: Simulated true and biased ranges vs time ($f_0 = 3$ Hz and $f_s = 40$ Hz)

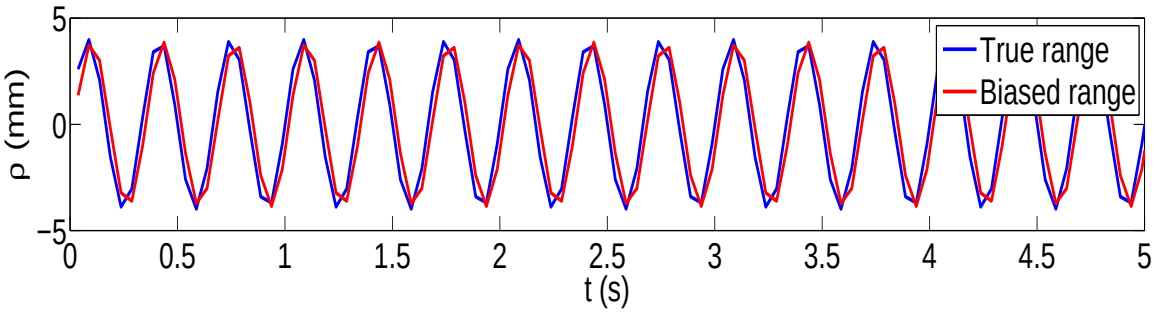

Figure 6.6: Simulated true and biased ranges vs time ($f_0 = 3$ Hz and $f_s = 20$ Hz)

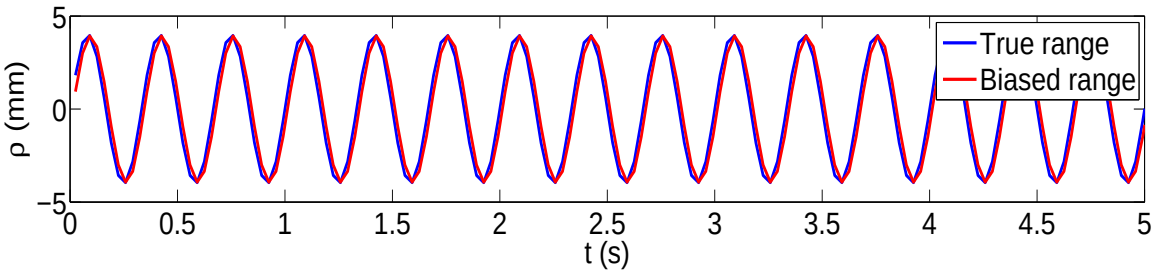

Figure 6.7: Simulated true and biased ranges vs time ($f_0 = 3$ Hz and $f_s = 30$ Hz)

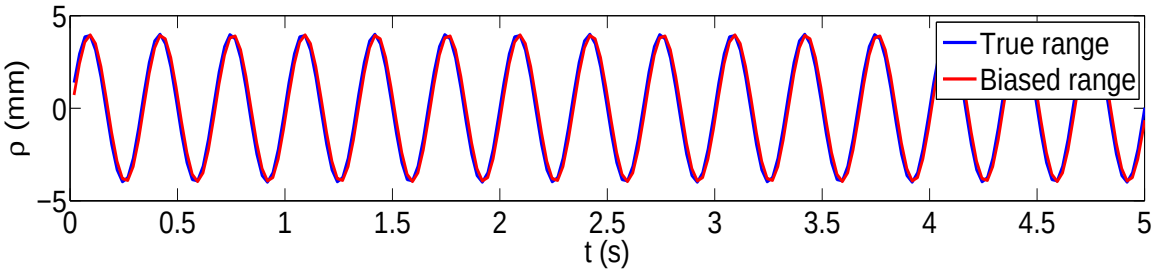

Figure 6.8: Simulated true and biased ranges vs time ($f_0 = 3$ Hz and $f_s = 40$ Hz)

Figure 6.9 shows the amplitude differences between the ideal 4 mm amplitude of the target motion and the estimated amplitude of the target motion by considering motion artefacts as a function of SF f_s.

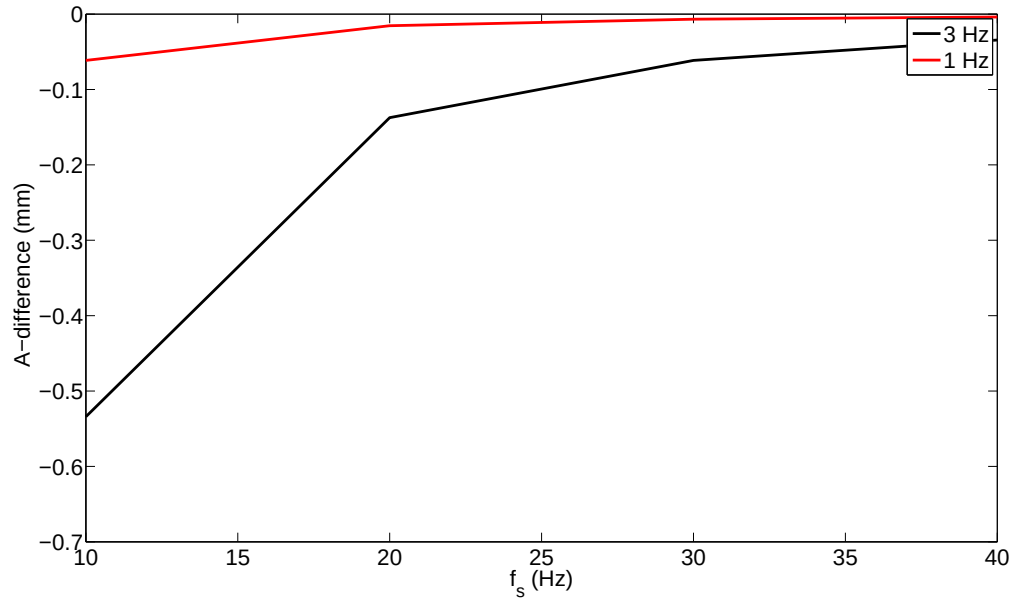

Figure 6.9: The differences between the ideal 4 mm and the biased deflections

As shown by Figure 6.9, when the SF is increased, the amplitude error is reduced. When the motion frequency is 1 Hz and the SF is 10 Hz, the greatest amplitude difference between the ideal 4 mm and the biased deflections is only -0.061 mm, which is 1.5% of 4 mm amplitude. Therefore, it is expected that the motion artefacts do not significantly affect the deflection measurement accuracy when the amplitude of the periodic sinusoidal loads is 4 mm and the motion frequency is 1 Hz.

The maximum difference is -0.53 mm, which is 13.6% of 4 mm amplitude when the motion frequency is 3 Hz and the SF is 10 Hz. The motion artefactes at 3 Hz loading frequency have more influences than at 1 Hz loading frequency since the higher loading frequency causes the higher phase shift mentioned in Chapter 5, which leads to higher motion artefacts. However, when the SF is 20 Hz, the amplitude difference is -0.14 mm. So, in order to reduce the

influence of motion artefacts and to keep the deflection measurement error under the half-millimetre level, the SF of TOF-RCs has to be at least 20 Hz when time-of-flight range cameras are used for data capture of the periodic motion with 4 mm amplitude and the 3 Hz motion frequency.

As a result, in the beam deflection measurement experiment, if the motion frequency is 1 Hz, the TOF-RCs set at 10 Hz, 20 Hz, 30 Hz and 40 Hz SFs can be used to do data capture, which can keep the error under half-millimetre as shown in the simulation data analysis. If the motion frequency is 3 Hz, the TOF-RCs set at 20 Hz, 30 Hz and 40 Hz SFs can be used to perform data capture, which can keep the measurement error under half-millimetre according to the simulation data analysis.

6.2 Experiment I: results and analysis

This section mainly focuses on the results and analysis of the deflection of the dynamic concrete beam with two SR4000 TOF-RCs set at different SFs during Experiment I. First, the range measurement precision of TOF-RCs is analyzed. Then, the 3D deflection measurements of the concrete are reported including vertical direction, longitudinal direction and lateral direction. Furthermore, statistical methods are used to analyze the deflection measurement precision. Finally, the best SF is chosen to monitor the deflection of the dynamic concrete beam.

6.2.1 The range measurement precision analysis of time-of-flight range cameras

Before the experiment, Cam 3 was used to capture zero-load data with two different MFs: 29 MHz and 31 MHz. Although the objects of main interest to measure the beam deflection were the thin plates attached to the bottom side of the concrete beam, the top surface of the beam was still useful to analyze the range measurement precision of the TOF-RC. The STD of the concrete beam top surface measurements can be used to evaluate the range

measurement precision of TOF-RCs. The range measurement precision of the TOF-RC was analyzed at different MFs and different SFs.

Figure 6.10 shows the STD of the beam top surface measurements as a function of SF and MF. As can be demonstrated in Figure 6.10, the range measurement precision of the concrete beam is improved by decreasing SF. In addition, by comparing the measurement precision between 29 MHz and 31 MHz MFs at the same SF, there are the significant improvements by using 31 MHz MF.

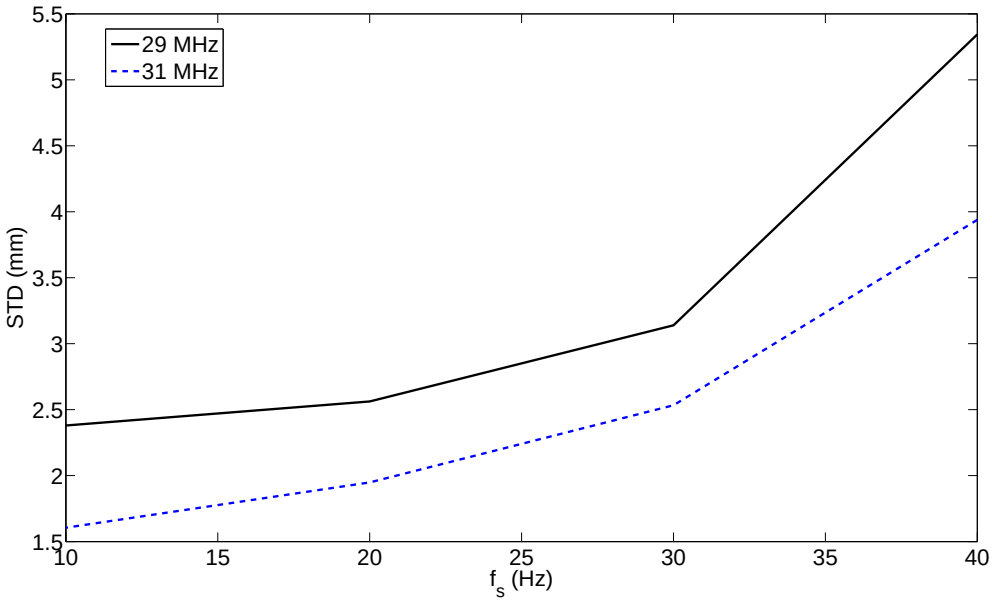

Figure 6.10: Precision analysis of the TOF-RCs

Table 6.1 lists the STDs of the beam top surface measurements. The improvement in range measurement precision is at least 11.3% by comparing the range measurement precision of these two different modulation frequencies. By comparing the two SFs, 40 Hz and 10 Hz, the range measurement precision improvement is over 55.4%.

Table 6.1: STDs of the beam top surface measurement

SF (Hz)	10	20	30	40
STD (mm)-29 MHz	2.38	2.56	3.14	5.34
STD (mm)-31 MHz	1.61	1.95	2.53	3.94
% improvement	14.5	11.5	11.3	26.3

6.2.2 Raw data derived from a SR4000 time-of-flight range camera

This sub-section discusses the deflection measurements of the concrete beam with two SR4000 TOF-RCs. Cam 3 captured seven thin plates using 29 MHz MF and Cam 4 captured another seven thin plates using 31 MHz MF. There was a common plate (Plate 7), which was captured by the two cameras. It is used as an example to analyze the motion trajectory and the deflection of the concrete beam.

Figure 6.11 illustrates the raw data trajectory of Plate 7's centroid in vertical direction. As can be seen, even though there is random noise in the raw trajectory, the trend of the thin plate centroid is still a harmonic waveform.

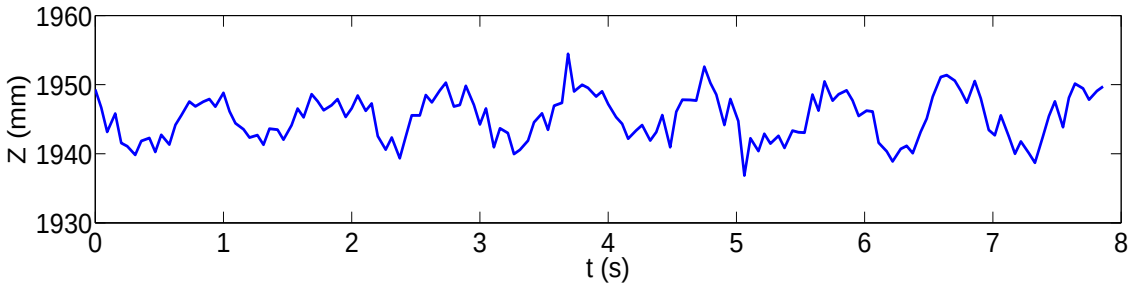

Figure 6.11: Raw data trajectory of one thin plate centroid

6.2.3 Data analysis of SR4000 time-of-flight range cameras: 1 Hz

6.2.3.1 Vertical displacement analysis

Absolute evaluation of the motion trajectory and the deflection of the concrete beam with SR4000 TOF-RCs was performed by comparing the motion trajectory and deflection estimated from the SR4000 TOF-RCs and the independent measurements from LDSs at the same time. In total 500 frames of measurement data were used to perform data analysis of the concrete beam deflection in vertical direction.

The motion frequencies (i.e. loading frequencies) and defections of the concrete beam can be derived based on the range data processing procedure mentioned in Chapter 5. Figure 6.12 shows an example of the so-obtained PSD of the thin plate centroid measured with one of

the TOF-RCs. As revealed from Figure 6.12, there is one dominant peak in the spectrum at the loading frequency. The estimated loading frequency is 1.0286 Hz.

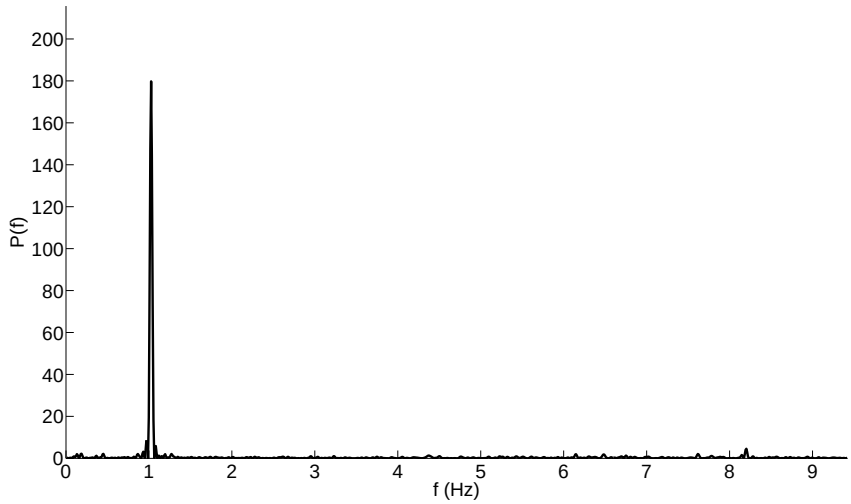

Figure 6.12: PSD of a thin plate motion with TOF-RC ($f_0 = 1$ Hz and $f_s = 20$ Hz)

The deflection measurement of the concrete beam from LDSs were analyzed using the same procedure as from TOF-RCs. The SF of the LDSs is 300 Hz. Figure 6.13 shows the so-obtained PSD of the same thin plate measured with one of the LDSs. There is one dominant peak in Figure 6.13 at the loading frequency. The estimated loading frequency is 1.0296 Hz.

With the recovered loading frequency, the other coefficients of the harmonic model Equation 5.29 can be estimated by using linear least-squares. Then, the approximate values of the loading frequency and the other coefficients were used as initial values for parameter estimates of the harmonic model. Non-linear least squares was used to derive the optimal values of the coefficients that can be used to calculate frequency and amplitude of the concrete beam motion. Figures 6.14, 6.15, 6.16 and 6.17 show the thin plate centroid trajectories when Cam 4 using 31 MHz MF was set at four different SFs. The black curve is the reconstructed thin plate trajectory. The blue curve is the raw thin plate trajectory. As can be seen, the motion trajectories are the sinusoidal waveforms at the four different SFs. When SFs were 10 Hz and 20 Hz, the raw measurements of the thin plate motion have less noise.

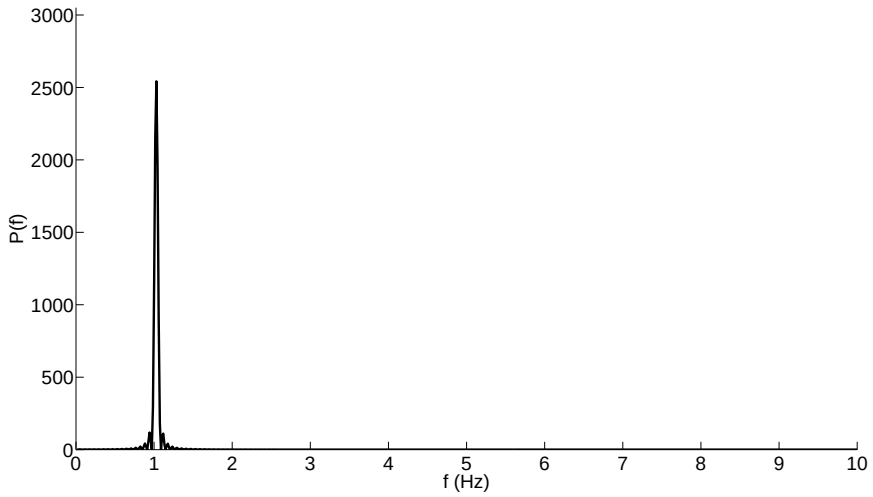

Figure 6.13: PSD of a thin plate motion with LDS

While for 30 Hz and 40 Hz SFs, the raw measurements of thin plate motion have much more noise. The derived trajectories from Cam 3 are similar to those from Cam 4.

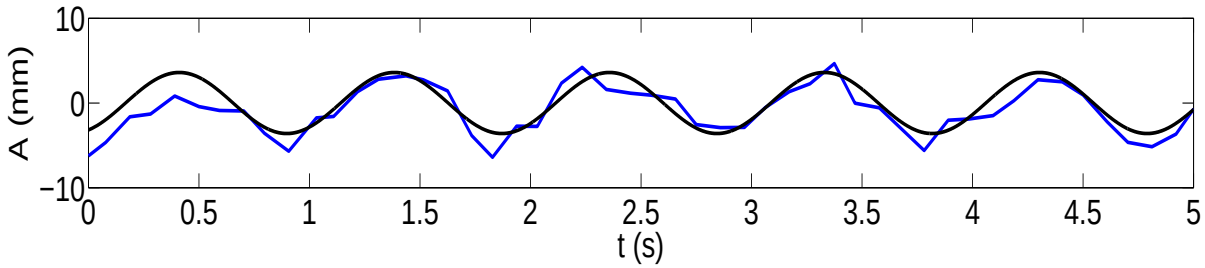

Figure 6.14: Thin plate centroid trajectories ($f_0 = 1$ Hz and $f_s = 10$ Hz)

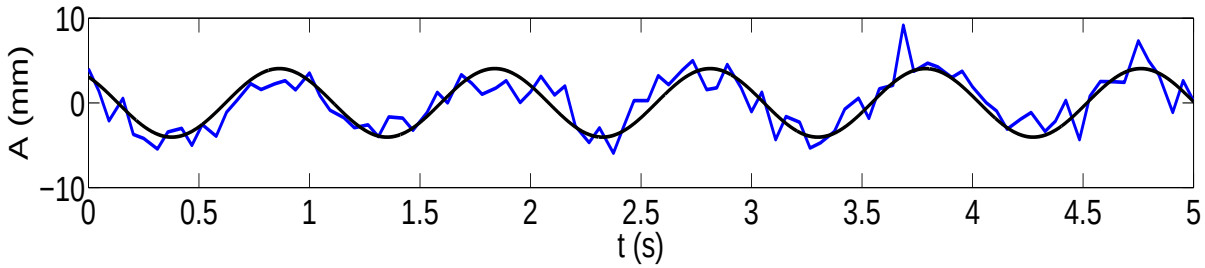

Figure 6.15: Thin plate centroid trajectories ($f_0 = 1$ Hz and $f_s = 20$ Hz)

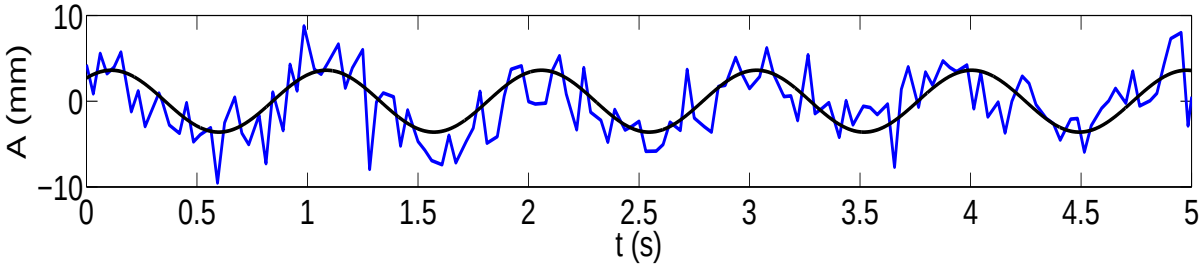

Figure 6.16: Thin plate centroid trajectories ($f_0 = 1$ Hz and $f_s = 30$ Hz)

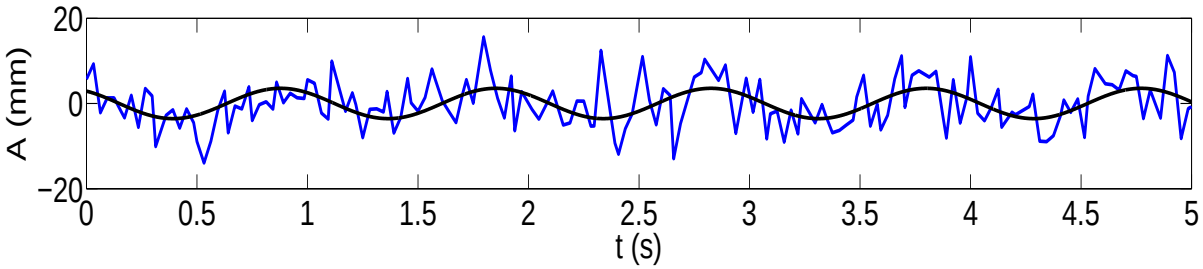

Figure 6.17: Thin plate centroid trajectories ($f_0 = 1$ Hz and $f_s = 40$ Hz)

Table 6.2 shows the STDs of estimated residuals derived from Cam 3 and Cam 4. As can be seen from Table 6.2, the STDs assess how well the fitted model fits the observation measurement data and the observation measurement precision. With increasing SF, the measurement precision is decreased. Overall, the measurement precision of Cam 4 is higher than Cam 3 because Cam 4 was set at 31 MHz MF which is higher than Cam 3's MF.

Table 6.2: Experiment I: STDs of residuals ($f_0 = 1$ Hz)

f_s (Hz)	10	20	30	40
$\sigma_{\hat{r}}$(Cam3) (mm)	2.37	3.32	6.05	13.08
$\sigma_{\hat{r}}$(Cam4) (mm)	1.18	1.78	2.73	4.83

Figure 6.18 illustrates an example of the trajectories of the chosen thin plate recovered from the TOF-RC and the LDS measurements. As can be seen, the recovered trajectories match very well. The estimated loading frequency is 1.0280 Hz obtained from the LDS measurements using non-linear least-squares. Its STD is 4.53e-006 Hz. The estimated deflection derived from LDS measurement is 3.93 mm and its corresponding STD is 5.50e-004 mm.

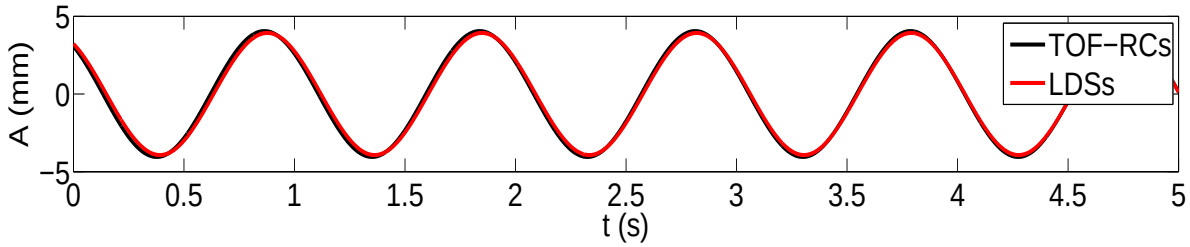

Figure 6.18: The estimated trajectories of the same thin plate with TOF-RC and LDS (f_0 = 1 Hz and f_s = 30 Hz)

The recovered loading frequencies derived from the range measurements of the two TOF-RCs are reported in Table 6.3 at different SFs. The loading frequency difference Δf_0 is the difference between the TOF-RC and LDS determined loading frequencies. Δf_0 is listed in Table 6.3. Moreover, the STDs of the estimated loading frequency σ_{f_0} are also reported in Table 6.3. As revealed from Table 6.3 the loading frequency can be recovered at four different SFs with high absolute accuracy based on Δf_0. The measurement precision of the loading frequency is decreased with increasing SF.

Table 6.3: Experiment I: Estimated loading frequency (f_0 = 1 Hz)

f_s(Hz)	10	20	30	40
f_0(Cam3) (Hz)	1.0281	1.0291	1.0266	1.0247
f_0(Cam4) (Hz)	1.0280	1.0280	1.0276	1.0270
Δf_0(Cam3) (Hz)	0.0001	0.0011	-0.0014	-0.0033
Δf_0(Cam4) (Hz)	0	0	-0.0004	-0.0019
σ_{f_0}(Cam3) (Hz)	4.9e-004	0.0012	0.0033	0.0064
σ_{f_0}(Cam4) (Hz)	2.2e-004	5.7e-004	0.0015	0.0031

The maximum deflections estimated for the concrete beam are calculated from the two TOF-RCs with different SFs and their differences (ΔA) with respect to the maximum deflections derived from the LDSs. They are reported in Table 6.4. In addition, Table 6.4 reports the differences of the estimated maximum deflection between TOF-RCs and LDSs. When the ideal loading frequency was 1 Hz, in order to keep the measurement error under half-millimetre accuracy, Cam 3 cannot be set at 10 Hz and 40 Hz SFs. For Cam 4, the

four different SFs can be used to obtain half-millimetre level accuracy. Since the MF of TOF-RCs impacts the deflection measurement accuracy, the absolute deflection accuracy of Cam 4 is higher than the absolute deflection accuracy of Cam 3. Meanwhile, when the SF is higher, the range measurement noise is larger. Motion artefacts cause lower absolute deflection accuracy for Cam 3 and Cam 4 set at 10 Hz SF. The absolute accuracy of the beam deflection with the TOF-RC is much smaller than the 10 mm absolute accuracy reported by the manufacturer. As shown in Table 6.4, STDs of amplitude σ_A are all less than 1 mm.

Table 6.4: Experiment I: Deflection of Plate 7 ($f_0 = 1$ Hz)

f_s (Hz)	10	20	30	40
A (Cam3) (mm)	3.31	3.55	3.56	4.90
A (Cam4) (mm)	3.61	4.05	3.61	3.56
ΔA (Cam3) (mm)	-0.62	-0.38	-0.37	0.97
ΔA (Cam4) (mm)	-0.32	0.12	-0.32	-0.37
σ_A (Cam3) (mm)	0.15	0.21	0.38	0.83
σ_A (Cam4) (mm)	0.08	0.11	0.17	0.31

Moreover, even though, by analyzing Plate 7, the maximum deflection of the concrete beam was obtained, other thin plate data analysis should be considered as well, which demonstrates the wide coverage advantage of TOF-RCs. Based on Table 6.4 analysis, the best sampling frequency is 20 Hz. Therefore, Table 6.5 shows the deflections of the all thin plate motion except Plate 12 at 20 Hz SFs. There is too much light around Plate 12, which lead to overexposure so Plate 12 could not be extracted automatically. The deflections of Plate 1 to Plate 7 are calculated from Cam 4. The deflections of Plate 8 to Plate 13 are estimated from Cam 3.

Figure 6.19 illustrates the beam deflection at 20 Hz SF derived from the TOF-RCs and also shows the beam deflection derived the five LDSs. As can be seen, the deflection of the thin plates along the length of the concrete beam increases towards the centre plate (i.e. Plate 7). Figure 6.19 illustrates well one of the advantages of the SR4000 TOF-RC: the wide coverage spanned by two cameras is greater than that of the five LDSs. As shown in

Table 6.5: Experiment I: Deflection of the thin plate motion

Plates	A (mm)-20 Hz
Plate 1	0.31
Plate 2	1.34
Plate 3	1.98
Plate 4	2.75
Plate 5	3.45
Plate 6	3.98
Plate 7	4.05
Plate 8	3.78
Plate 9	3.34
Plate10	2.59
Plate11	1.89
Plate13	0.32

Figure 6.19, the LDS located under the Plate 9 was unable to accurately determine the beam deflection. As shown in Figure 6.20, its raw trajectory is not sinusoidal, suggesting some sort of defect. The other four plate trajectories derived from LDS are sinusoidal.

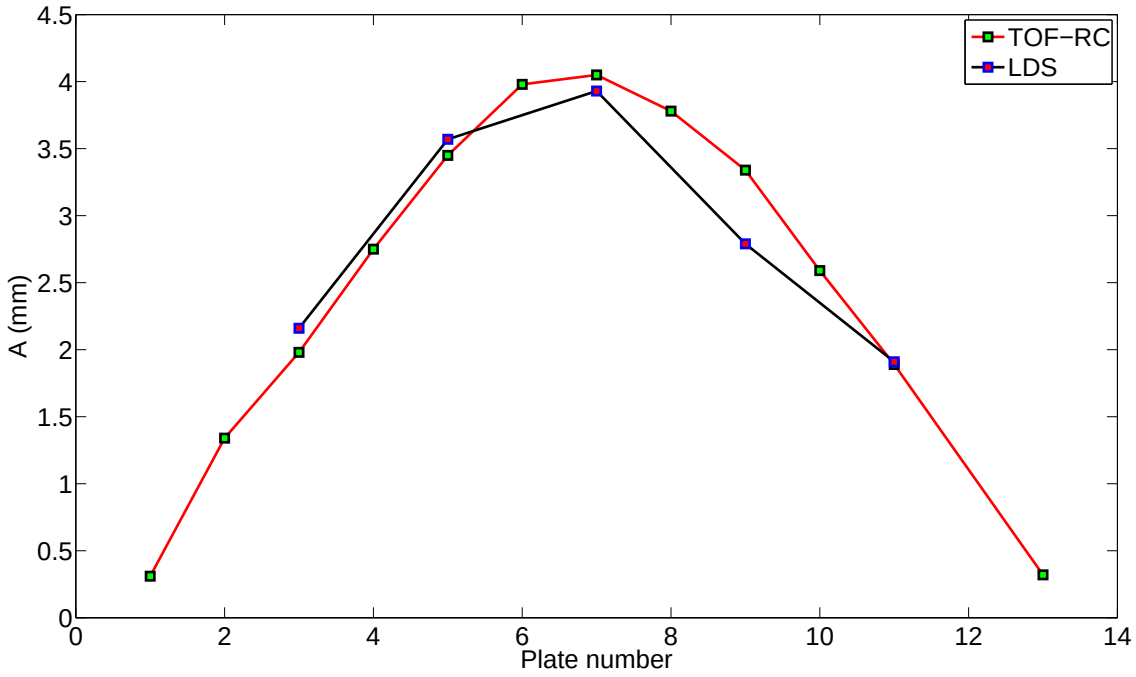

Figure 6.19: Experiment I: Beam deflection ($f_0 = 1$ Hz and $f_s = 20$ Hz)

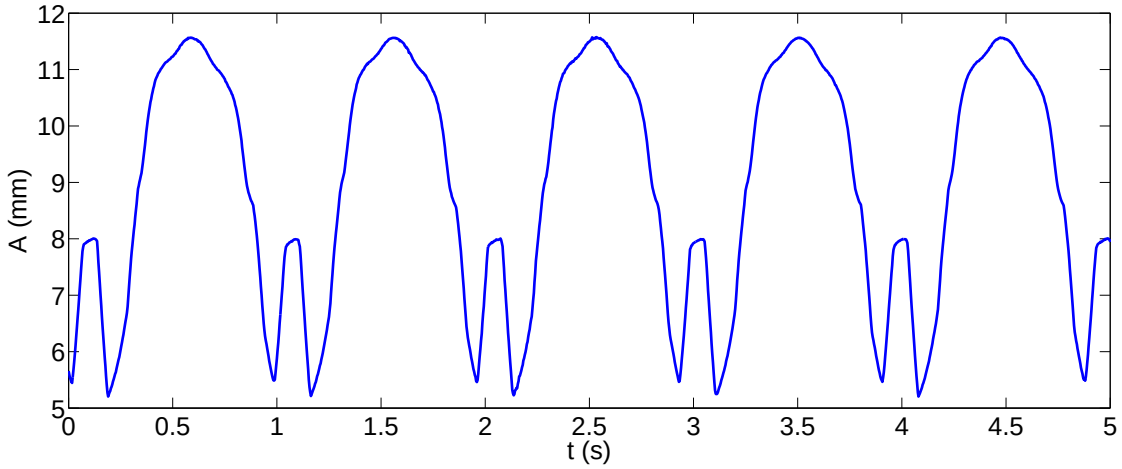

Figure 6.20: Experiment I: Raw data-LDS (Plate 9)

6.2.3.2 Longitudinal displacement analysis

There were two cylinders between the concrete beam and steel support shown in Figure 4.1. One cylinder was fixed and another one was not. So, the deflection could occur longitudinally. The trajectory of the longitudinal motion was a sinusoidal wave because the concrete beam was subjected to periodic loads.

Figures 6.21 and 6.22 show the longitudinal displacement analysis of Plate 7 derived from Cam 4 at 1 Hz loading frequency when the sampling frequencies are 10 Hz and 20 Hz using the same data set as the vertical analysis. As can be seen, the longitudinal motion trajectory of the concrete beam can be recovered. Table 6.6 lists the recovered frequencies and displacements of Plate 7 longitudinal motion dervied from Cam 4 at 10 Hz and 20 Hz SFs.

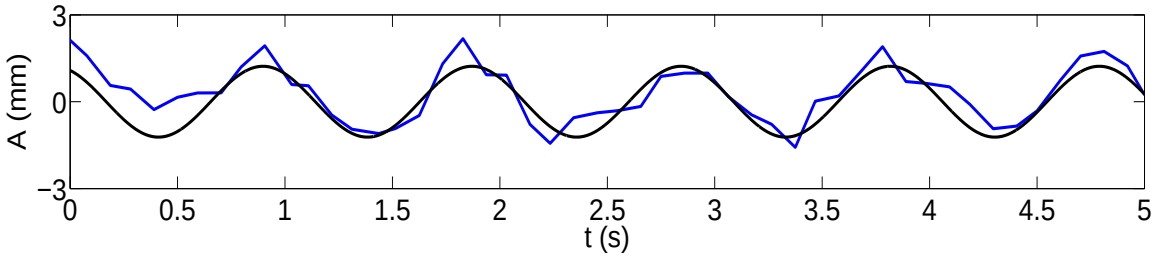

Figure 6.21: Longitudinal displacements ($f_0 = 1$ Hz and $f_s = 10$ Hz)

The 3D coordinates of one circular target centroid attached on the floor were measured to

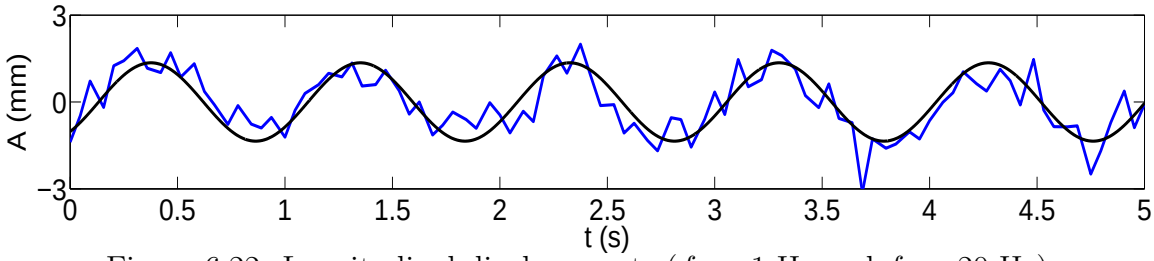

Figure 6.22: Longitudinal displacements ($f_0 = 1$ Hz and $f_s = 20$ Hz)

Table 6.6: Experiment I: Longitudinal displacement-Cam4 ($f_0 = 1$ Hz)

f_s(Hz)	10	20
f_0 (Hz)	1.0276	1.0262
A (mm)	1.2	1.4
σ_{f_0} (Hz)	2.2e-004	5.9e-004
σ_A (Hz)	0.03	0.04

determine the accuracy of the longitudinal displacements. The X-coordinate of the circular target centroid is as a function of time shown in Figure 6.23. As can be seen, the trajectory of the X-coordinate as a function of time is not a sinusoidal curve but noise. In order to prove it is indeed noise, the PSD of the time series can be calculate and analyzed. Figure 6.24 shows the PSD of one circular target centroid trajectory. As can be seen, there is no dominant peak above the statistical significance level ($\alpha = 0.5$) in Figure 6.24, which means that the trajectory is noise (Press et al., 1992). Therefore, it can be conclude that the floor and the cameras mounted on the steel frames were not moving during the fatigue loading test. So, the longitudinal displacements of the circular target were not caused by the periodic loads.

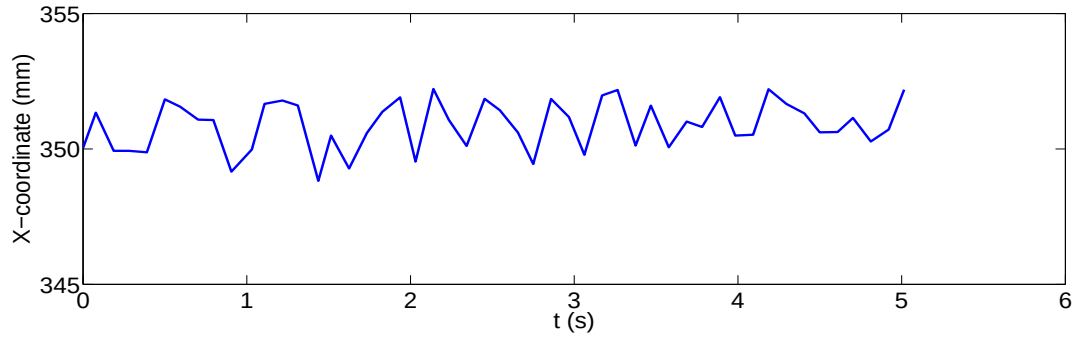

Figure 6.23: X-coordinate of an circular target centroid ($f_0 = 1$ Hz and $f_s = 10$ Hz)

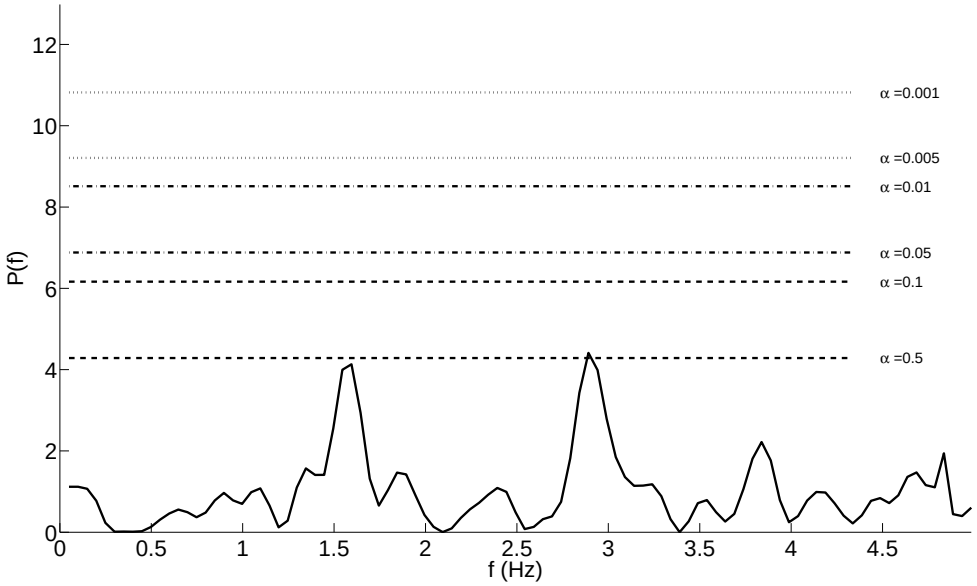

Figure 6.24: PSD of longitudinal direction ($f_0 = 1$ Hz)

6.2.3.3 Lateral displacement analysis

The presence of the lateral displacement suggests that the load was applied eccentrically. If it is not, the lateral displacement will be happened. Figures 6.25 shows the lateral displacement analysis of Plate 7 derived from Cam 4 at 1 Hz loading frequency when the sampling frequency is 10 Hz. As can be seen, the lateral motion trajectory of the concrete beam can be recovered.

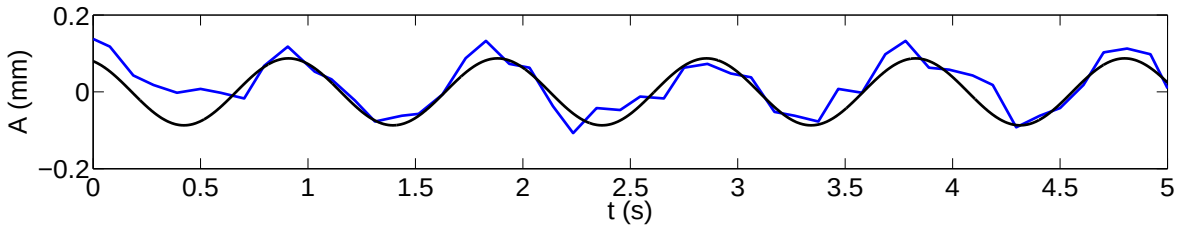

Figure 6.25: Lateral displacements ($f_0 = 1$ Hz and $f_s = 10$ Hz)

Figure 6.26 show the Y-coordinate of the circular target centroid is as a function of time. As can be seen, the trajectory of the Y-coordinate as a function of time is not a sinusoidal curve. Figure 6.27 show the PSD of the circular target centroid trajectory in lateral direction.

As can be seen, there is no dominant peak above $\alpha = 0.5$ statistical significance level in Figure 6.27 as well. Therefore, it can be concluded that the cameras mounted on the steel frames were stable during the fatigue loading test. So, the lateral displacements of the circular target were not caused by the periodic loads.

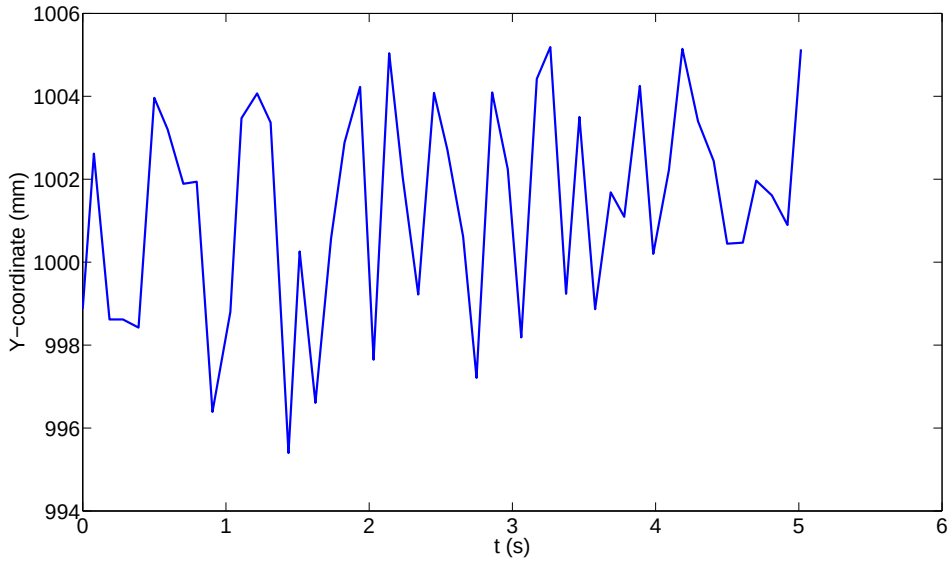

Figure 6.26: Y-coordinate of an circular target centroid ($f_0 = 1$ Hz and $f_s = 10$ Hz)

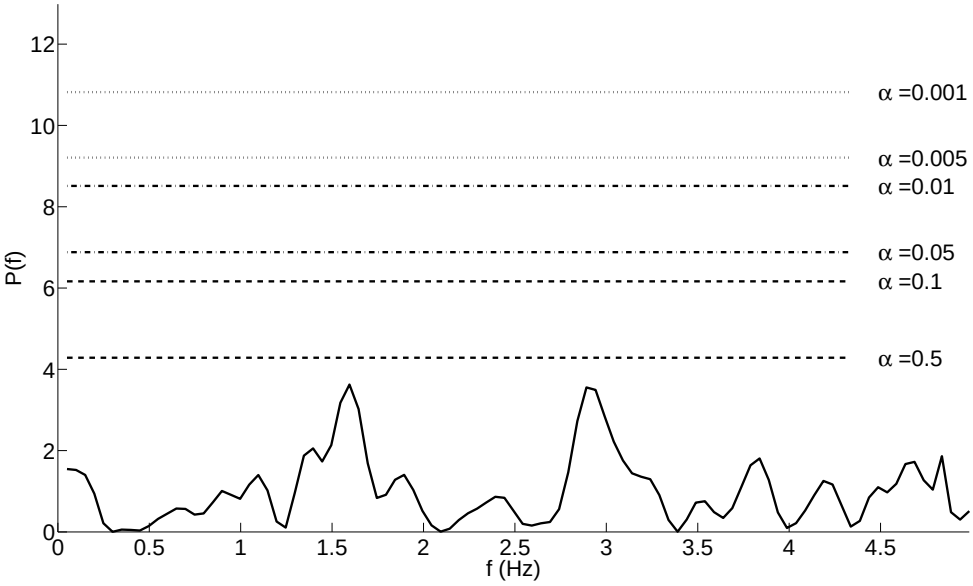

Figure 6.27: PSD of lateral direction($f_0 = 1$ Hz)

6.2.4 Data analysis of SR4000 time-of-flight range cameras: 3 Hz

In this sub-section, the absolute accuracy of deflections of the concrete beam is assessed when the loading frequency was 3 Hz. The data processing procedure is similar with Sub-section 6.2.3. The evaluation was performed comparing measurements from two TOF-RCs set at SFs of 10 Hz, 20 Hz, 30 Hz and 40 Hz and five LDSs using 300 Hz SF. Five hundred frames of the measurement data were used to perform data analysis of the concrete beam deflection.

6.2.4.1 Vertical displacement analysis

Figure 6.28 shows PSD $P(f)$ of Plate 7 motion at 30 Hz SF in vertical direction. Just like Figure 6.12, there is one dominant peak in Figure 6.28 at 3 Hz loading frequency. So, the estimated frequency of the concrete beam motion is 3.0914 Hz.

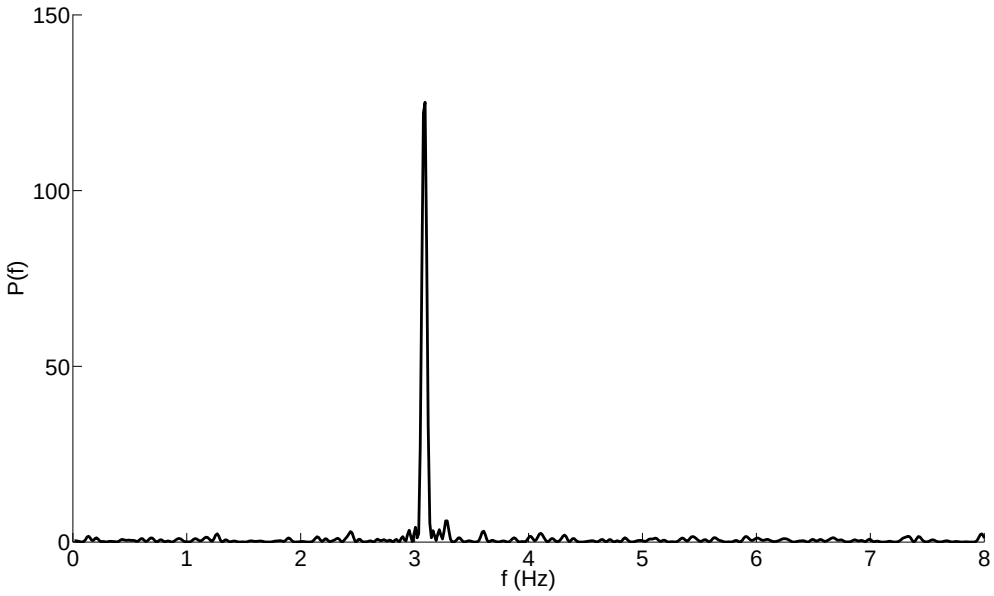

Figure 6.28: PSD of thin plate centroid trajectory-3 Hz (TOF-RC)

The same process described in Sub-section 6.2.3 was performed to calculate the vertical deflections and frequency of the concrete beam motion when the loading frequency was 3 Hz. Figures 6.29, 6.30, 6.31 and 6.32 show the motion trajectories of the thin plate centroid

at the four SFs recovered from Cam 4 with 31 MHz MF. The motion trajectories of the thin plate centriod derived from Cam 3 are similar to those of Cam 4.

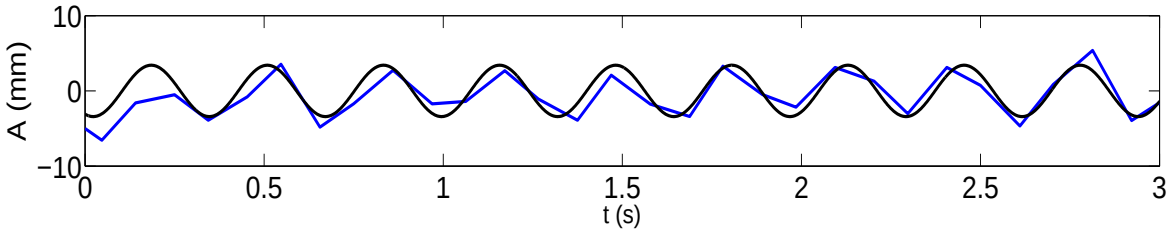

Figure 6.29: Thin plate centroid trajectories ($f_0 = 3$ Hz and $f_s = 10$ Hz)

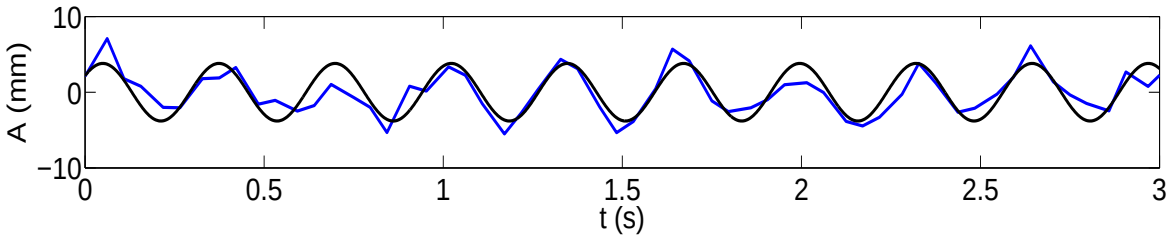

Figure 6.30: Thin plate centroid trajectories ($f_0 = 3$ Hz and $f_s = 20$ Hz)

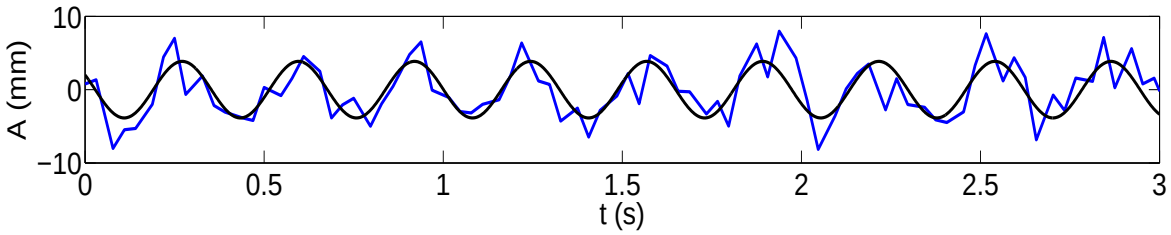

Figure 6.31: Thin plate centroid trajectories ($f_0 = 3$ Hz and $f_s = 30$ Hz)

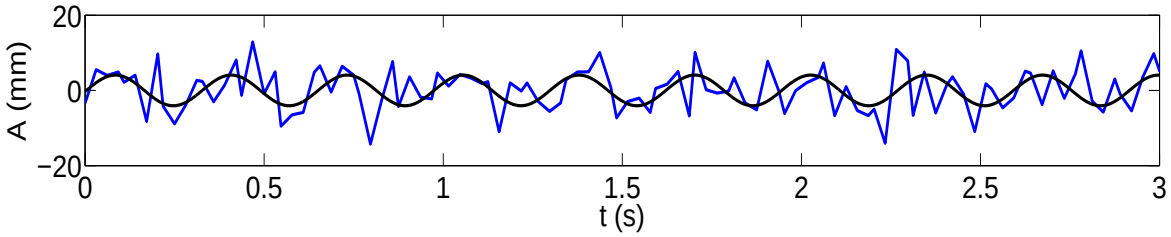

Figure 6.32: Thin plate centroid trajectories ($f_0 = 3$ Hz and $f_s = 40$ Hz)

Table 6.7 lists the STDs of the estimated residuals. As has been seen from Table 6.7, the measurement precision of the observation data have a decreasing trend with increasing SF.

Table 6.7: Experiment I: STDs of estimated residuals ($f_0 = 3$ Hz)

f_s (Hz)	10	20	30	40
$\sigma_{\hat{r}}$(Cam3) (mm)	2.51	3.72	5.34	12.09
$\sigma_{\hat{r}}$(Cam4) (mm)	1.24	1.71	2.67	4.52

The recovered loading frequencies from the different optical sensors are reported in Table 6.8. The differences in recovered loading frequencies between the TOF-RC and the LDS are presented as well. Meanwhile, the STDs of the estimated loading frequency are illustrated at different SFs. The estimated maximum deflection and loading frequency derived from the LDS measurements were 4.00 mm and 3.0843 Hz with the same solution as the TOF-RC. Their corresponding STDs were 9.59e-004 mm and 8.21e-006 Hz respectively.

Table 6.8: Experiment I: Estimated loading frequency ($f_0 = 3$ Hz)

f_s(Hz)	10	20	30	40
f_0(Cam3) (Hz)	3.0842	3.0851	3.0826	3.0801
f_0(Cam4) (Hz)	3.0846	3.0843	3.0853	3.0904
Δf_0(Cam3) (Hz)	-0.0002	0.0008	-0.0017	-0.0042
Δf_0(Cam4) (Hz)	0.0003	0	0.0010	0.0061
σ_{f_0}(Cam3)	4.79e-004	0.0012	0.0022	0.0060
σ_{f_0}(Cam4)	2.49e-004	5.94e-004	0.0013	0.2883

Table 6.9 presents the deflection measurements of the concrete beam motion calculated from the two TOF-RC measurements with different SFs. In addition, the differences of the estimated maximum deflection derived between the TOF-RC and the LDS results are presented. The STDs of the deflection estimates are illustrated at different SFs as well.

As revealed in Table 6.8, the loading frequencies can be accurately recovered at all SFs based on the absolute accuracies reported in Table6.8. Additionally, the differences in the loading frequency for the two TOF-RCs are very small. Moreover, the STDs of the loading frequency suggests that a higher SF results in a higher STD.

Table 6.9: Experiment I: Deflection of Plate 7 ($f_0 = 3$ Hz)

f_s (Hz)	10	20	30	40
A(Cam3) (mm)	3.57	3.71	4.72	5.10
A(Cam4) (mm)	3.42	3.80	3.86	4.07
ΔA(Cam3) (mm)	-0.43	-0.29	0.72	1.10
ΔA(Cam4) (mm)	-0.58	-0.2	-0.14	0.07
σ_A(Cam3) (mm)	0.16	0.21	0.34	0.76
σ_A(Cam4) (mm)	0.08	0.11	0.17	0.29

As can be seen in Table 6.9, the largest deflection difference derived from Cam 3 is 1.10 mm at 40 Hz SF. The absolute accuracy of the beam deflection with the TOF-RC is much greater than the 10 mm absolute accuracy reported by the manufacturer. Motion artefacts impact the absolute accuracies for both cameras at 10 Hz SF. STDs of the loading frequencies and deflections are low, which means the deflection is measured with high measurement precision at all four SFs. However it degrades with increasing SF, and when the SF was 40 Hz, the absolute accuracies for both cameras are low.

According to previous absolute accuracy and precision analysis, the best SF is 20 Hz. So, Table 6.10 reports the deflections of all thin plates. Figure 6.33 shows the concrete beam deflection at 20 Hz SF derived from TOF-RC and the beam deflection derived from the five LDSs. As can be seen, the deflection of all thin plate motion (except Plate 12) along the length of the concrete beam illustrate the increases towards the mid-span of the concrete beam. However, the LDS located under the Plate 9 was unable to accurately determine the beam deflection because of the same reason mentioned in Sub-section 6.2.3.

Table 6.10: Experiment I: Deflections of the thin plates ($f_0 = 3$ Hz)

Plates	A (mm)-20 Hz
Plate 1	0.33
Plate 2	1.22
Plate 3	1.84
Plate 4	2.57
Plate 5	3.43
Plate 6	3.52
Plate 7	3.80
Plate 8	3.52
Plate 9	3.22
Plate10	2.59
Plate11	1.79
Plate13	0.21

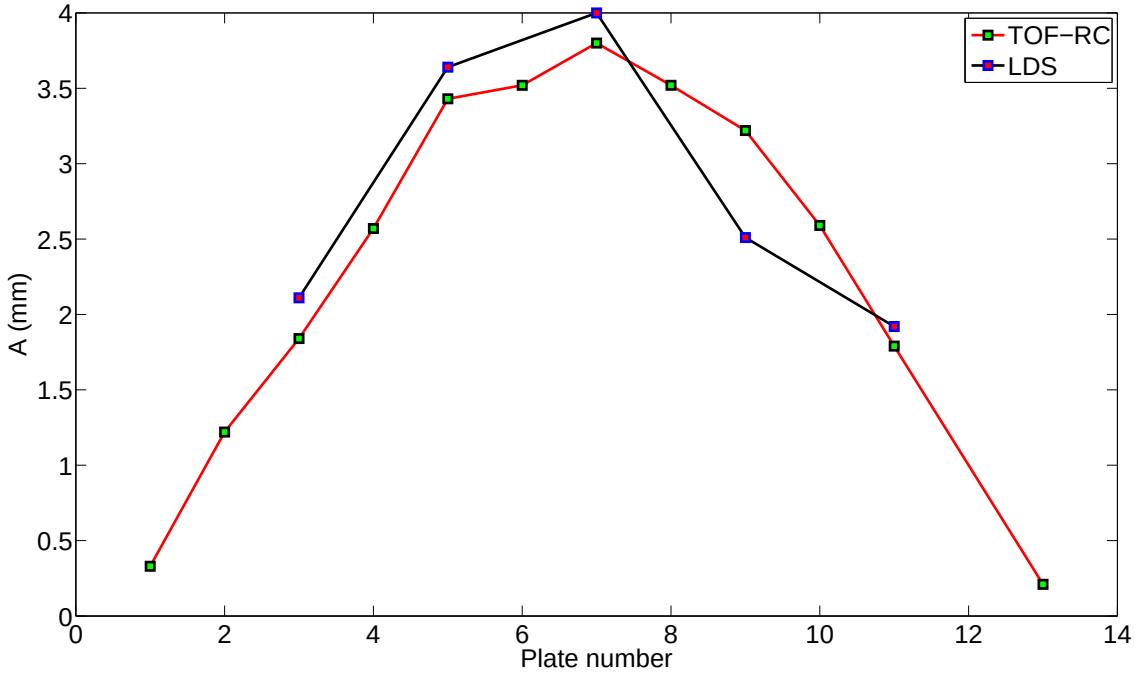

Figure 6.33: Experiment I: Beam deflection ($f_0 = 3$ Hz and $f_s = 20$ Hz)

6.2.4.2 Longitudinal displacement analysis

Figures 6.34 shows the longitudinal displacement analysis of Plate 7 derived from Cam 4 at 3 Hz loading frequency when the sampling frequency was 20 Hz. As can be seen, the longitudinal motion trajectory of the concrete beam can be recovered. The recovered loading

frequency and recovered deflection on longitudinal are 3.0832 Hz and 1.2 mm respectively. Their corresponding STDs are 6.4e-004 Hz and 0.04 mm.

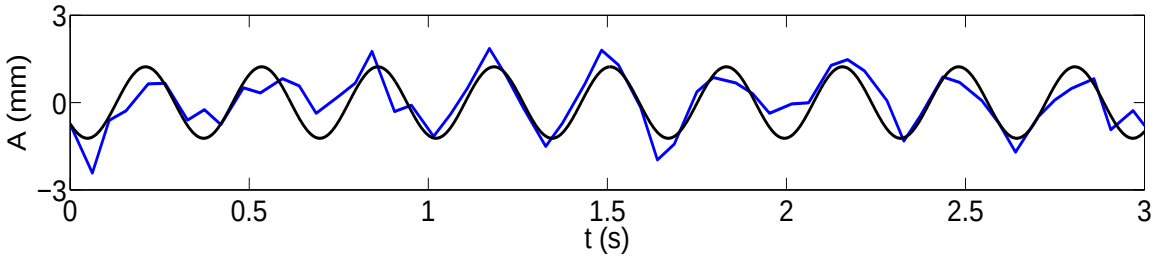

Figure 6.34: Longitudinal displacements ($f_0 = 3$ Hz and $f_s = 20$ Hz)

Figure 6.35 shows the X-coordinate of the circular target centroid is as a function of time. As can be seen, the trajectory of the X-coordinate as a function of time is not a sinusoidal curve. Figure 6.36 shows the PSD of the one circular target centroid trajectory in longitudinal direction. As can be seen, there is no dominant peak above $\alpha = 0.5$ statistical significance level in Figure 6.36. Therefore, it can be concluded that the cameras mounted on the steel frames were stable during the fatigue loading test. So, the longitudinal displacements of the circular target were not caused by the periodic loads when the loading frequency was 3 Hz.

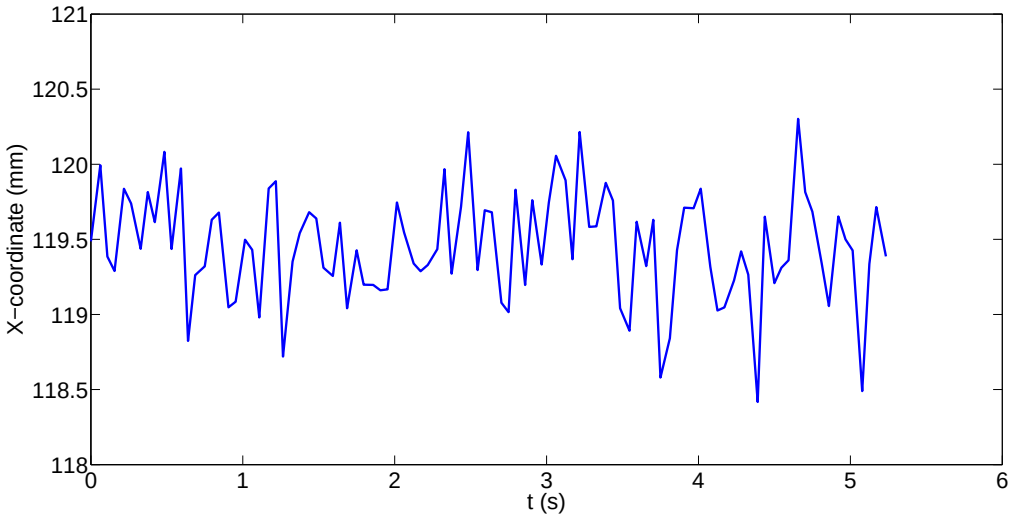

Figure 6.35: X-coordinate of an circular target centroid ($f_0 = 3$ Hz)

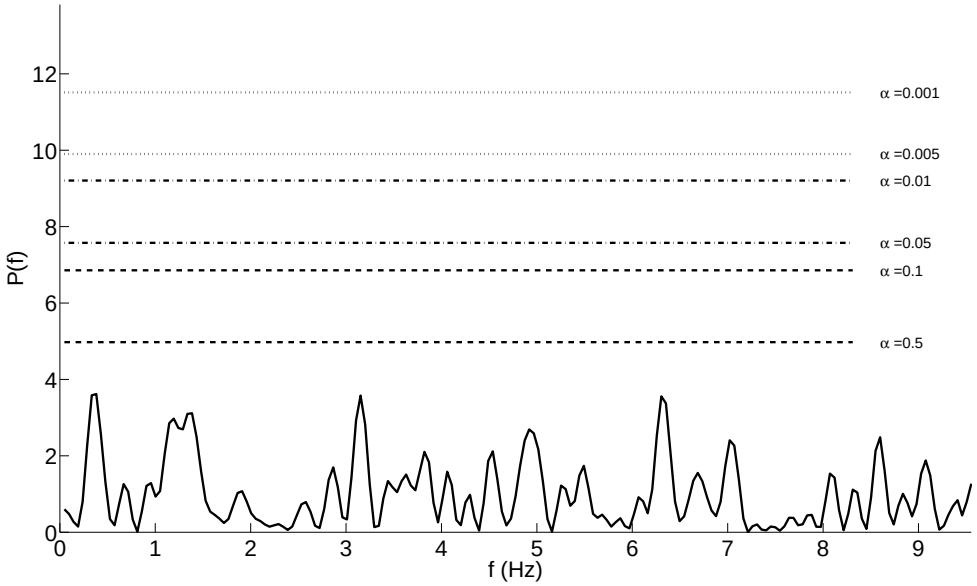

Figure 6.36: PSD of longitudinal direction($f_0 = 3$ Hz)

6.2.4.3 Lateral displacement analysis

The loading frequency and deflection on the lateral direction cannot be recovered because of the effects of the measurement noise significantly. Figure 6.37 show the Y-coordinate of a circular target centroid is as a function of time. As can be seen, the trajectory of the Y-coordinate as a function of time is not a sinusoidal curve. However by calculating the PSD of one circular target centroid trajectory on lateral direction, the PSD can still be used to analyze whether and the steel frame were moving. Figure 6.38 shows the PSD of the circular target centroid trajectory on lateral direction. As can be seen, there is no dominant peak above $\alpha = 0.5$ in Figure 6.38. Therefore, it can be concluded that the cameras mounted on the steel frames were stable during the fatigue loading test when the loading frequency was 3 Hz.

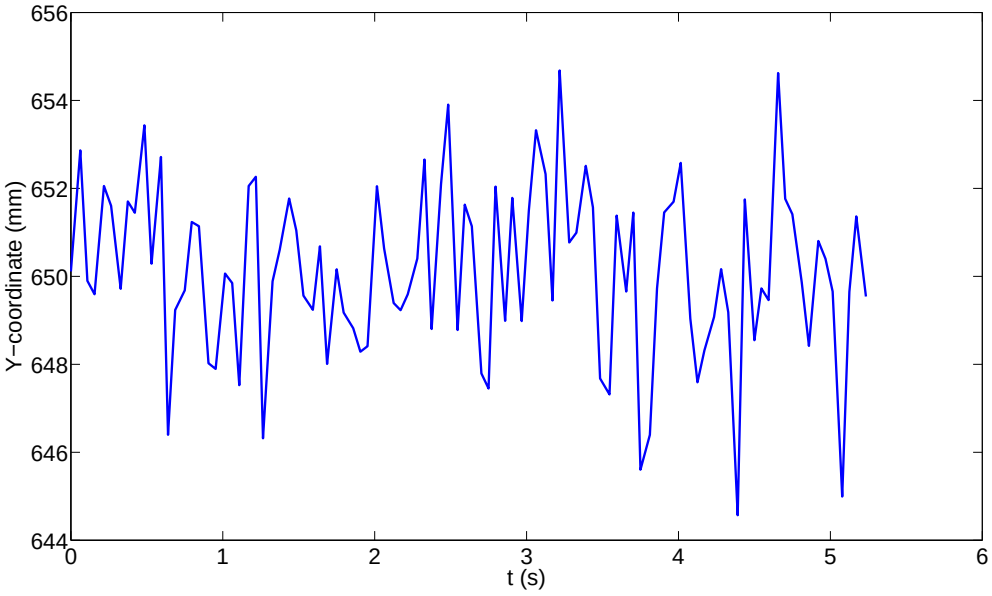

Figure 6.37: Y-coordinate of an circular target centroid ($f_0 = 3$ Hz)

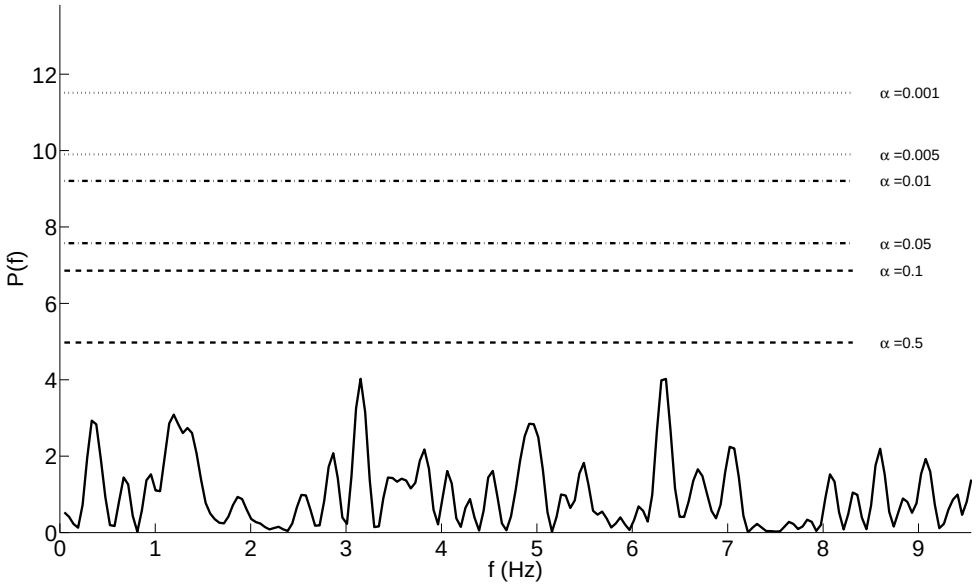

Figure 6.38: PSD of lateral direction($f_0 = 3$ Hz)

6.3 Experiment II: results and analysis

During Experiment II, two SR4000 ethernet cable TOF-RCs (Cam 3 and Cam 4), one SR 4000 USB cable TOF-RC camera (Cam 2) and one Kinect LC-RC (Cam 1) were used to perform data capture for the dynamic deflection experiment (i.e. fatigue loading test). It took eleven days to do the fatigue loading test. The results of the SR4000 USB cable TOF-RC are presented. The camera was used to record concrete beam motion in real time, which was useful to analyze fatigue properties of the concrete beam. Cam 2 was set at 29 MHz. Based on the results and analysis of Experiment I, it could be concluded that higher dynamic measurement accuracy could be obtained if the SF was set at 20 Hz. Therefore, the SF of SR4000 TOF-RCs was set at 20 Hz during Experiment II. In addition, preliminary results are reported in this section for Kinect LC-RC. The SF of Kinect was set at 30 Hz during Experiment II.

6.3.1 Repeatability test of SR4000 time-of-flight range cameras

The zero-load test was conducted to assess the beam deflection measurement repeatability of SR4000 TOF-RCs. Plate 7 was used to evaluate measurement consistency of the SR4000 TOF-RCs. Three data sets (i.e. Case 1, Case 2 and Case 3) derived from different time were used to analyze the repeatability of the SR4000 TOF-RC. Each data set had over 1500 frames and the duration was more than 75 s. Figures 6.39, 6.40 and 6.41 show the Z-coordinate of the thin plate centroid at zero-load state.

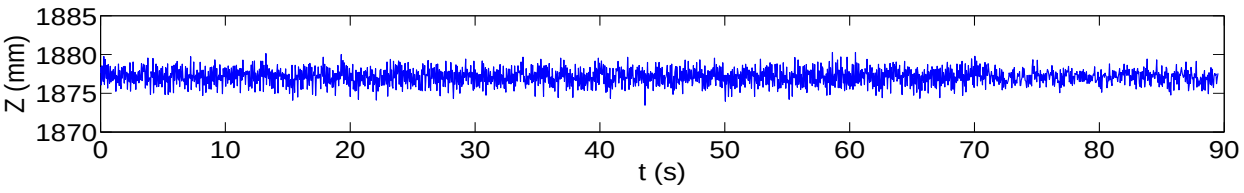

Figure 6.39: Case 1: repeatability test of SR4000

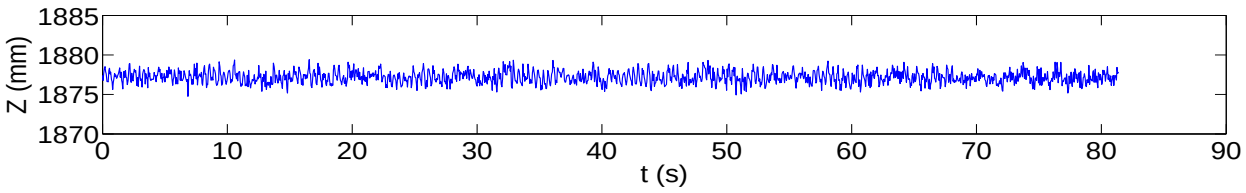

Figure 6.40: Case 2: repeatability test of SR4000

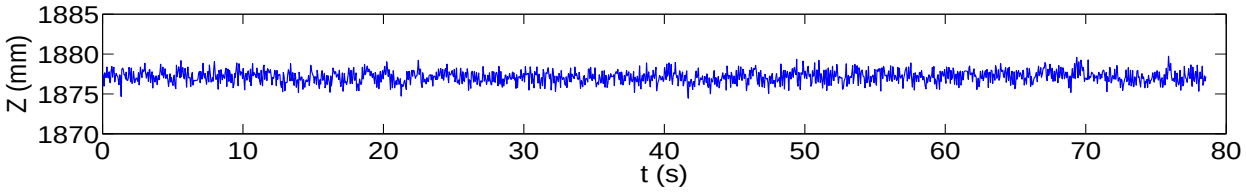

Figure 6.41: Case 3: repeatability test of SR4000

Table 6.11 shows the mean values and the STDs of the three cases. As has been demonstrated in Table 6.11, the maximum difference of Z-coordinates mean among three cases is 0.1 mm. The STDs of the three cases are less than 1.2 mm. The mean values show that range measurements of SR4000 TOF-RCs are stable over a short period of time, which is sufficient to meet the absolute accuracy requirements for the deflection measurement.

Table 6.11: Repeatability test of SR4000

	Z-Mean (mm)	STD (mm)
Case 1	1877.1	0.79
Case 2	1877.2	0.79
Case 3	1877.1	1.11

6.3.2 Data analysis SR4000 time-of-flight range cameras: 1 Hz

For the SR4000 USB cable TOF-RC, the real-time thin plate extraction method mentioned in Chapter 5 was used. In order to analyze the tendency of the concrete beam deflection as a function of time, a random hour of deflection measurement data was extracted for each day when 1 Hz periodic loads were implemented.

6.3.2.1 Vertical displacement analysis

First, several data sets were used to perform vertical displacement analysis when the loading frequency was 1 Hz. Figures 6.42, 6.43 and 6.44 show the raw and estimated motion trajectories of the concrete beam for three data sets.

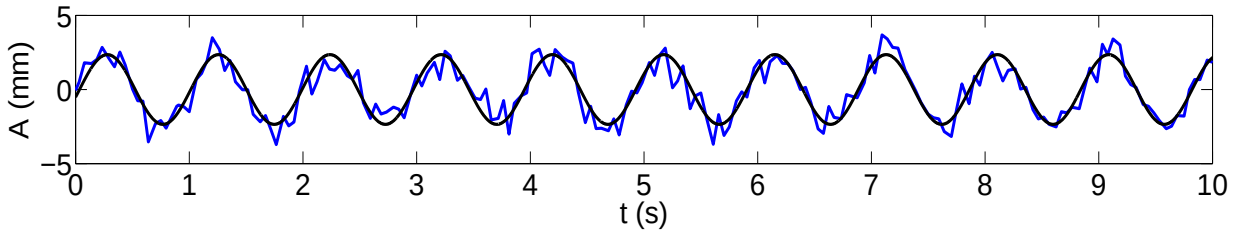

Figure 6.42: Case 1: thin plate raw and reconstructed trajectories ($f_0 = 1$ Hz)

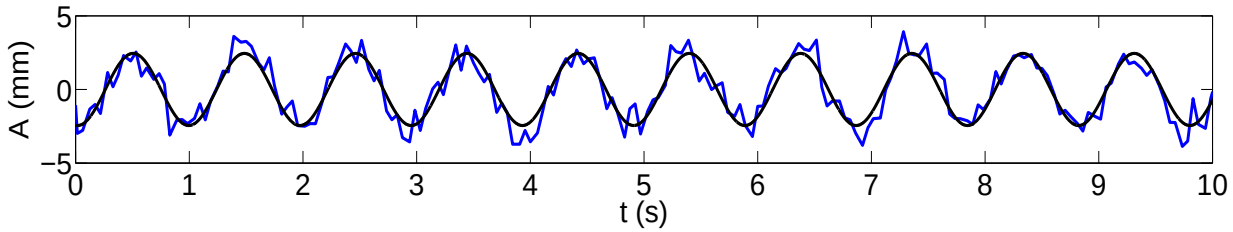

Figure 6.43: Case 2: thin plate raw and reconstructed trajectories ($f_0 = 1$ Hz)

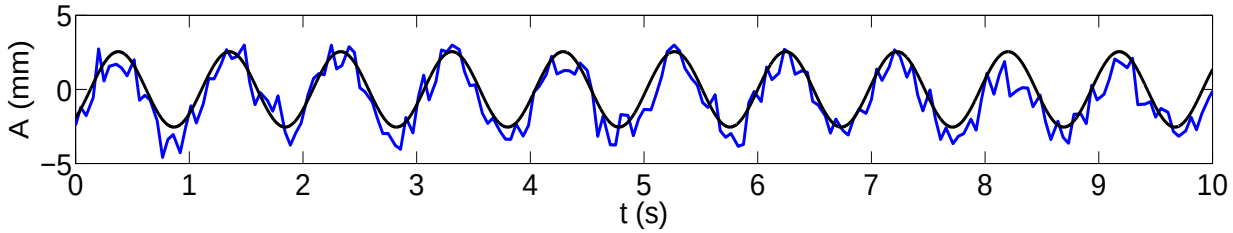

Figure 6.44: Case 3: thin plate raw and reconstructed trajectories ($f_0 = 1$ Hz)

Table 6.12 shows the analysis of six day data sets of the dynamic deflection measurement derived from Cam 2 when the loading frequency was 1 Hz based on the number of cycles (TNC). The recovered frequencies and deflections of the concrete beam motion are reported in Table 6.12. The absolute accuracies of the frequencies and deflections of the concrete beam motion are illustrated as well. Moreover, the STDs of the estimates and their residuals are

listed. As can be seen, the motion frequencies and deflections can be accurately recovered for all cases by calculating the absolute accuracies (Δf_0 and ΔA) in Table 6.12. Additionally, the deflectons of the concrete beam motion changed slightly by comparing Day 1 (4500) with Day 9 (395500). The deflection difference between Day 1 (4500) and Day 9 (395500) is 0.2 mm based on SR4000 measurement data and it is 0.43 mm based on LDS measurement data. The absolute accuracy of the deflection is half-millimetre for each day. The STDs of the motion frequencies and the deflections are very small. The STDs of the loading frequency are less than 0.1 mHz and the STDs of the deflections are less than 0.015 mm. As a result, the SR4000 TOF-RCs have the capability to measure dynamic structural behavior with small deflection.

Table 6.12: Experiment II: Estimated frequency and deflections ($f_0 = 1$ Hz)

Dates	Day 1	Day 2	Day 3	Day 6	Day 8	Day 9
TNC	4500	42950	49850	231900	337000	395500
f_0(Hz)-Cam 2	1.0219	1.0221	1.0221	1.0223	1.0224	1.0221
A (mm)-Cam 2	2.35	2.45	2.49	2.54	2.55	2.55
f_0(Hz)-LDS	1.0219	1.0222	1.0222	1.0222	1.0224	1.0222
A (mm)-LDS	2.18	2.32	2.55	2.58	2.59	2.61
Δf_0 (Hz)	0	-0.0001	-0.0001	0	-0.0001	-0.0001
ΔA (mm)	0.17	0.13	0.06	0	-0.04	-0.06
σ_{f_0} (Hz)-Cam 2	3.39e-006	6.17e-006	6.91e-006	4.74e-006	1.06e-005	3.34e-006
σ_A (mm)-Cam 2	0.0094	0.0053	0.0127	0.0104	0.0146	0.0098
$\sigma_{\hat{r}}$ (mm)-Cam 2	0.75	0.74	0.80	0.71	0.79	0.77
σ_{f_0} (Hz)-LDS	1.69e-005	2.28e-005	5.39e-006	1.58e-007	1.76e-007	2.07e-007
σ_A (mm)-LDS	0.0018	0.0026	6.69e-004	2.22e-004	2.47e-004	2.94e-004

6.3.2.2 Longitudinal displacement analysis

Figures 6.45, 6.46 and 6.47 show the longitudinal displacements of several data sets when the concrete beam was subjected to periodic loads at 1 Hz loading frequency. As can be seen, the longitudinal motion trajectory of the concrete beam can be recovered for all cases.

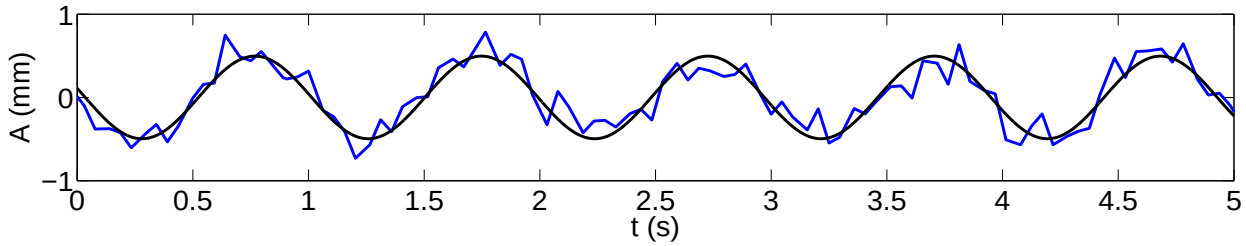

Figure 6.45: Case 1: longitudinal displacements ($f_0 = 1$ Hz)

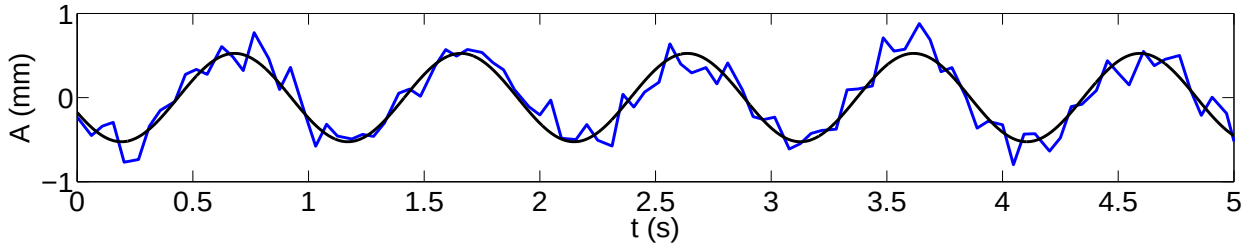

Figure 6.46: Case 2: longitudinal displacements ($f_0 = 1$ Hz)

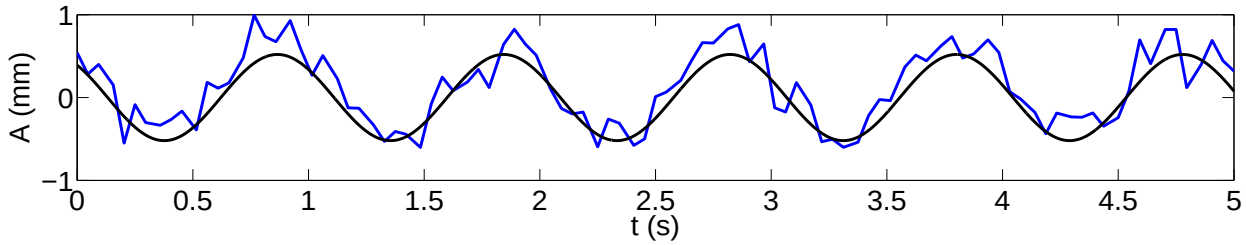

Figure 6.47: Case 3: longitudinal displacements ($f_0 = 1$ Hz)

Table 6.13 shows the recovered frequencies and deflections of the thin plate longitudinal motion based on the SR4000 TOF-RC measurements. Furthermore, Table 6.13 reports STDs of the estimates of the longitudinal displacements and the motion frequencies. The measurement precisions of the loading frequencies are very high. Low STDs of the longitudinal displacement estimates show that the measurement precision of the longitudinal displacements are very promising. The longitudinal displacements of Plate 7 for each data set are all around a half millimetre. In addition, the LDSs were not used to obtained the longitudinal displacements so that the absolute accuracies cannot be obtained.

Table 6.13: Experiment II: Longitudinal displacement analysis-Cam 2 ($f_0 = 1$ Hz)

Dates	TNC	f_0(Hz)	A (mm)	σ_{f_0} (Hz)	σ_A (mm)	$\sigma_{\hat{r}}$ (mm)
Day 1	4500	1.0219	0.50	3.39e-006	0.0020	0.16
Day 2	42950	1.0221	0.52	6.17e-007	0.0011	0.15
Day 3	49850	1.0221	0.53	6.91e-006	0.0027	0.17
Day 6	231900	1.0223	0.51	6.76e-006	0.0030	0.20
Day 8	337000	1.0224	0.51	1.29e-005	0.0036	0.19
Day 9	395500	1.0222	0.52	3.87e-006	0.0023	0.18

Table 6.14 provides comparisons of the recovered loading frequencies from the vertical displacement and the longitudinal displacement. The loading frequency differences between them are almost equivalent except that there are tiny differences of Day 8 and Day 9.

Table 6.14: Experiment II: Comparisons of recovered loading frequencies ($f_0 = 1$ Hz)

Dates	TNC	f_0 (Hz)-V	f_0 (Hz)-L	δf_0 (Hz)
Day 1	4500	1.0219	1.0219	0
Day 2	42950	1.0221	1.0221	0
Day 3	49850	1.0221	1.0221	0
Day 6	231900	1.0223	1.0223	0
Day 8	337000	1.0223	1.0224	-0.0001
Day 9	395500	1.0221	1.0222	-0.0001

6.3.2.3 Lateral displacement analysis

Figures 6.48, 6.49 and 6.50 shows the lateral displacements of the concrete beam when the loading frequency was 1 Hz. The lateral motion trajectories with 1 Hz loading frequency

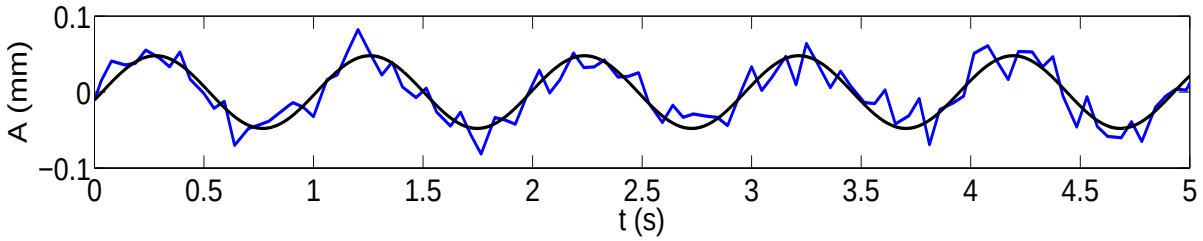

Figure 6.48: Case 1: lateral displacements ($f_0 = 1$ Hz)

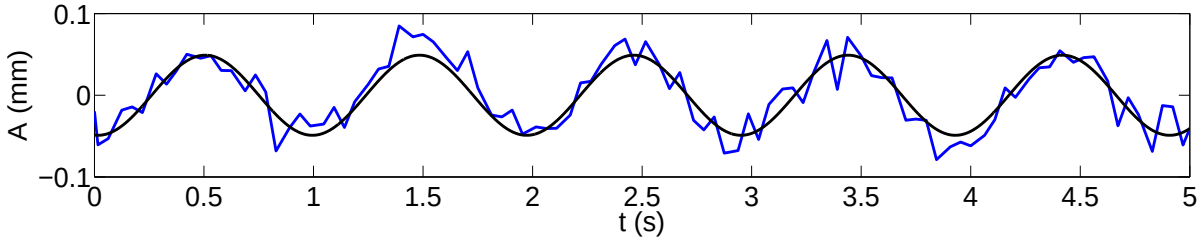

Figure 6.49: Case 2: lateral displacements ($f_0 = 1$ Hz)

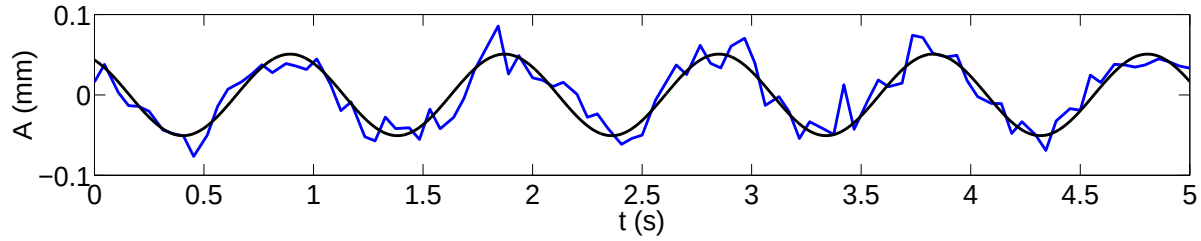

Figure 6.50: Case 3: lateral displacements ($f_0 = 1$ Hz)

Table 6.15 reports the estimated results of the lateral motion of the concrete beam. The estimated deflections and frequencies of the lateral motion of the concrete beam are reported. The STDs of the estimated parameters are given as well. As can be illustrated, the loading frequencies estimated from lateral, vertical and longitudinal motions are identical on Day 1. The loading frequency difference among three motions is only 0.0010 Hz on Day 2. The loading frequency difference among three motions is only 0.0001 Hz on Day 3. The lateral displacement measurements are reliable since the floor and steel frame were stable based on the previous analysis.

Table 6.15: Experiment II: Lateral displacement analysis-Cam 2 ($f_0 = 1$ Hz)

Dates	TNC	f_0(Hz)	A (mm)	σ_{f_0} (Hz)	σ_A (mm)	$\sigma_{\hat{r}}$ (mm)
Day 1	4500	1.0219	0.048	4.22e-005	4.81e-004	0.017
Day 2	42950	1.0211	0.049	7.32e-005	5.71e-004	0.017
Day 3	49850	1.0220	0.051	2.53e-004	8.29e-004	0.015

But sometimes the raw trajectories of Plate 7 centroid are not sinusoidal curve just like Figure 6.51. It shows an example of the raw measurement of the lateral motion. Based on those raw measurements, the deflections and frequencies of the lateral motion cannot be

estimated because of the effects of the measurement noise significantly.

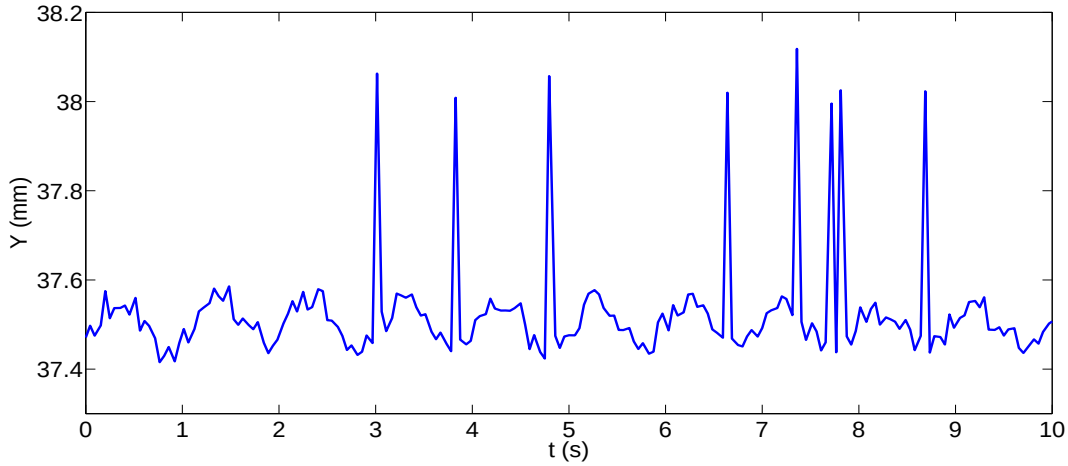

Figure 6.51: Raw data of the lateral displacements ($f_0 = 1$ Hz)

6.3.3 Data analysis of SR4000 time-of-flight range cameras: 3 Hz

6.3.3.1 Vertical displacement analysis

During the dynamic concrete beam experiment, the vertical motion of the concrete beam with 3 Hz loading frequency was tested on ten days. Figures 6.52, 6.53 and 6.54 illustrate the raw and recovered trajectories of the vertical motion of a thin plate.

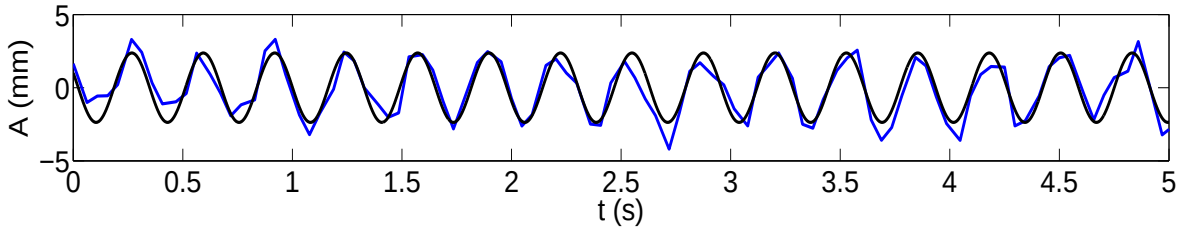

Figure 6.52: Case 1: thin plate raw and estimated trajectories ($f_0 = 3$ Hz)

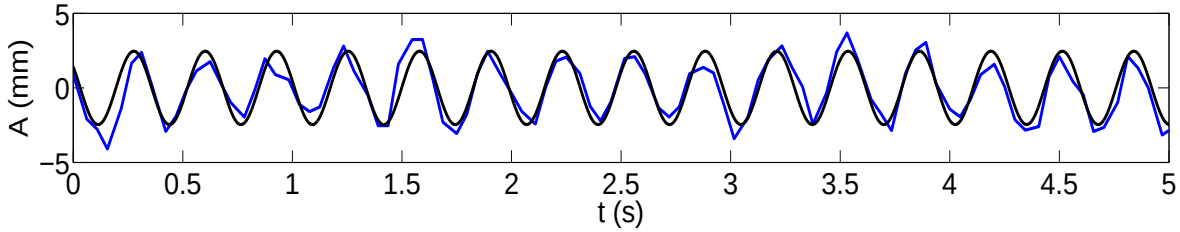

Figure 6.53: Case 2: thin plate raw and estimated trajectories ($f_0 = 3$ Hz)

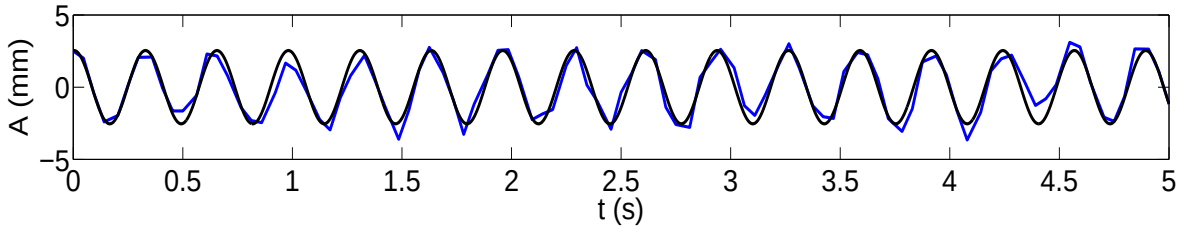

Figure 6.54: Case 3: thin plate raw and estimated trajectories ($f_0 = 3$ Hz)

As can be seen, the estimated vertical trajectories of the thin plate motion can be recovered from the raw measurements obtained from SR4000 TOF-RCs. All the figures illustrate 5 s of the vertical motion trajectories. Each data set for vertical analysis was captured at the same time of each day. The time difference of each data set was 24 hours except that there was no data set on Day 6. The concrete beam was only subjected to periodic loads at 1 Hz on Day 6.

Table 6.16 shows the recovered loading frequencies and the deflections of the concrete beam motion derived from TOF-RC (Cam 2) and LDS. Their differences are also given in Table 6.16. As can be seen, the absolute accuracy on each day is half-millimetre level. In all the cases, the deflections of the concrete beam increase slightly in time. The maximum deflection difference between Day 1 (32400) and Day 11 (880286) is just 0.31 mm based on the LDS measurement. The maximum deflection difference between Day 1 (32400) and Day 11 (880286) is 0.18 mm based on the SR4000 measurement. The recovered loading frequency differences have high absolute accuracy by comparing the loading frequencies derived from the TOF-RC and the LDS (i.e. Δf_0).

Table 6.17 gives the STDs of the deflections and loading frequencies derived from Cam 2 and the LDS. The number of raw measurement samples from Cam 2 is much more than the number of raw measurement samples from the LDS. For example, the number of sample of Day 1 data set is 35083 which is more than 10 times of the number of sample of Day 1 data set from LDS. Most of the STDs of the deflections derived from the LDS are less than the STDs derived from TOF-RCs. All STDs of the amplitude estimates on each day are less

than 0.02 mm based on the TOF-RC and LDS raw data measurements. All the STDs of the loading frequencies for each day are less than 0.1 mHz. STDs of Table 6.17 illustrate that estimates of the deflections and the loading frequencies have high precision. Moreover, Table 6.17 reports the STDs of the estimated residuals. They are less than 1 mm. As a result, the TOF-RC has an ability to record the dynamic deflection in real time.

Table 6.16: Experiment II: Estimated frequency and maximum deflection of Plate 7 ($f_0 = 3$ Hz)

Dates	TNC	f_0 (Hz)	A (mm)	f_0 (Hz)-LDS	A (mm)-LDS	Δf_0 (Hz)	ΔA(mm)
Day 1	32400	3.0672	2.37	3.0680	2.32	-0.0008	0.05
Day 2	60050	3.0677	2.42	3.0678	2.42	-0.0001	0.00
Day 3	92450	3.0678	2.43	3.0679	2.58	0.0001	-0.15
Day 4	154200	3.0677	2.44	3.0678	2.58	0.0001	-0.14
Day 5	226400	3.0680	2.46	3.0681	2.58	-0.0001	-0.12
Day 7	332900	3.0683	2.47	3.0684	2.60	-0.0001	-0.13
Day 8	391000	3.0686	2.48	3.0687	2.61	-0.0001	-0.13
Day 9	486400	3.0678	2.48	3.0679	2.63	-0.0001	-0.15
Day 10	677400	3.0673	2.54	3.0674	2.64	-0.0001	-0.10
Day 11	880286	3.0672	2.55	3.0673	2.63	-0.0001	-0.09

Table 6.17: Experiment II: Standard deviations with Cam 2 and LDS ($f_0 = 3$ Hz)

Dates	TNC	σ_{f_0} (Hz)	σ_A (mm)	$\sigma_{\hat{r}}$ (mm)	σ_{f_0} (Hz)-LDS	σ_A (mm)-LDS
Day 1	32400	7.43e-007	0.0057	0.76	5.58e-004	0.0061
Day 2	60050	2.78e-006	0.0092	0.79	1.02e-005	0.0021
Day 3	92450	9.56e-007	0.0060	0.71	4.25e-006	8.29e-004
Day 4	154200	5.64e-007	0.0046	0.62	4.68e-006	9.14e-004
Day 5	226400	7.81e-007	0.0062	0.82	2.14e-007	3.00e-004
Day 7	332900	8.34e-007	0.0059	0.73	1.42e-007	2.01e-004
Day 8	391000	1.62e-006	0.0076	0.77	1.48e-007	2.10e-004
Day 9	486400	1.52e-006	0.0075	0.77	1.97e-007	2.82e-004
Day 10	677400	1.57e-006	0.0062	0.57	1.96e-007	2.82e-004
Day 11	880286	5.17e-007	0.0043	0.56	1.93e-007	2.77e-004

The fatigue loading test can be used to determine the behaviour of the concrete beam. Figure 6.55 shows the fatigue loading results derived from the SR4000 TOF-RC and the LDS. The deflections of the concrete beam subjected to periodic loads are increased as a

function of the number of loading cycles. The maximum deflection difference between the TOF-RC and the LDS is 0.15 mm.

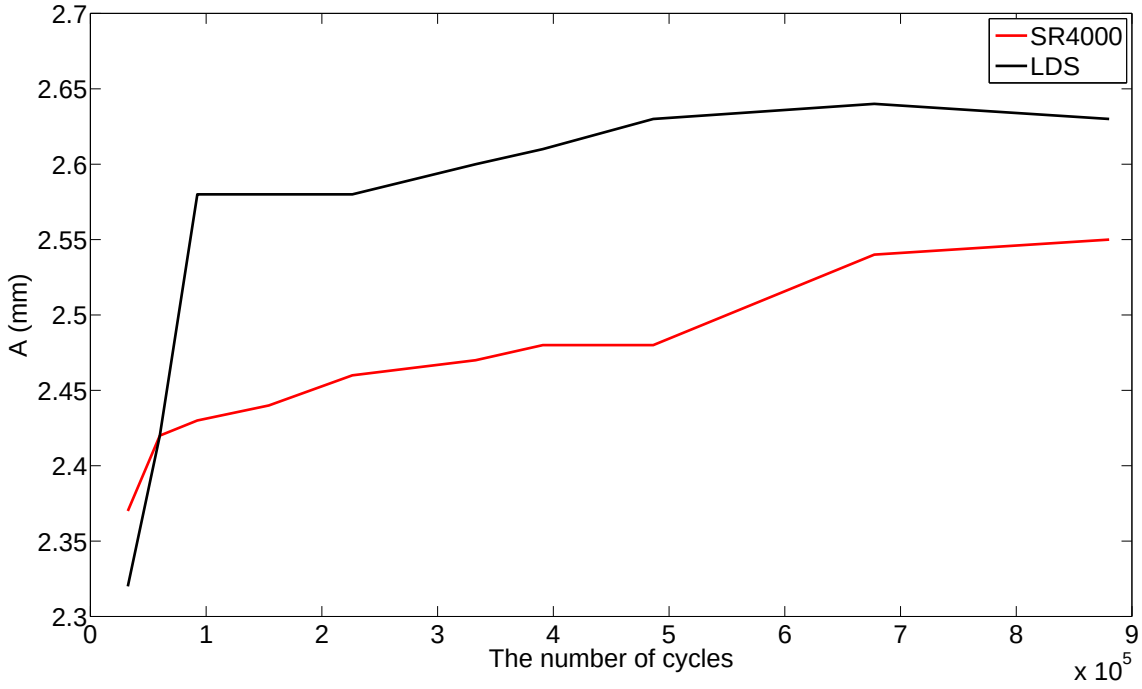

Figure 6.55: The fatigue loading results with SR4000 and LDS

6.3.3.2 Longitudinal displacement analysis

Figures 6.56, 6.57 and 6.58 show the longitudinal motion of the concrete beam when the loading frequency was 3 Hz. The motion trajectories with 3 Hz loading frequency have the same trend as the motion trajectories with 1 Hz loading frequency.

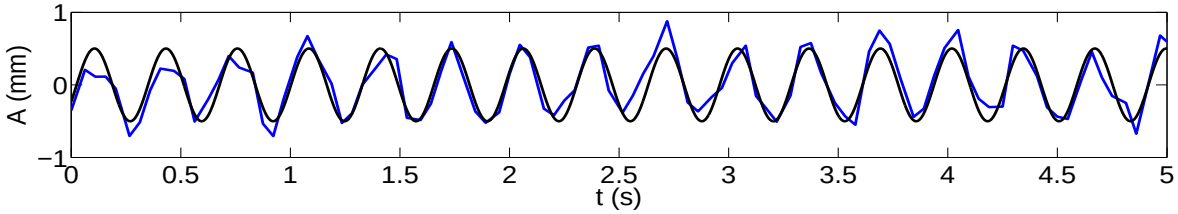

Figure 6.56: Case 1: longitudinal displacements ($f_0 = 3$ Hz)

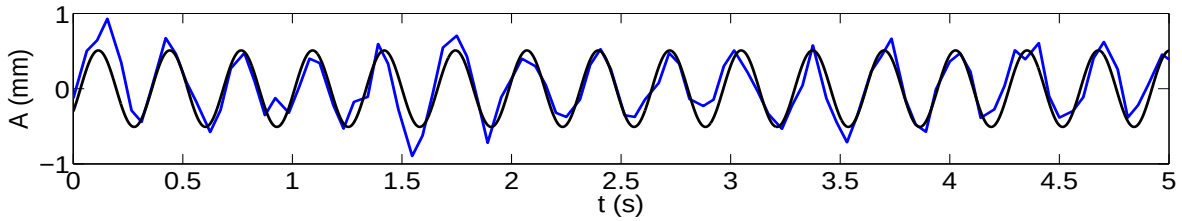

Figure 6.57: Case 2: longitudinal displacements ($f_0 = 3$ Hz)

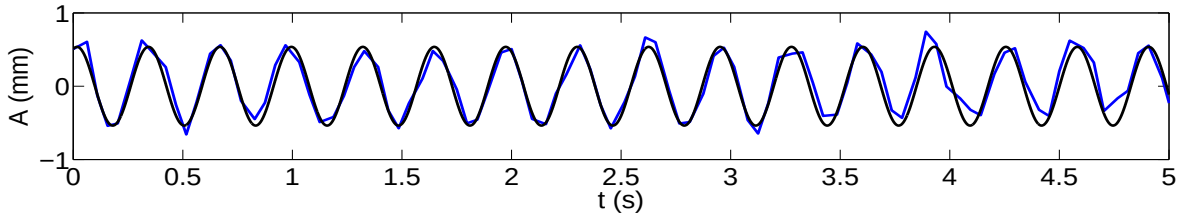

Figure 6.58: Case 3: longitudinal displacements ($f_0 = 3$ Hz)

Table 6.18 reports the longitudinal displacement analysis with 3 Hz loading frequency. First, the deflections of the longitudinal motion of the concrete beam are reported. Second, the estimated loading frequencies of each day are reported as well. Third, the STDs of the estimated deflections and frequencies of longitudinal motion are given in Table 6.18. As can be seen, during the fatigue load test, the longitudinal displacement did change significantly by comparing the deflections of Day 1 (32400) and Day 11 (880286) and the STDs of Day 1 and Day 11. The maximum difference of the deflections is 0.04 mm which is much larger than STD difference of deflections -0.0002 mm between Day 1 and Day 11 . In addition, the loading frequency can also be recovered with longitudinal displacement analysis. The low STDs of the longitudinal displacement estimates indicate that the measurement precisions the longitudinal displacements are very high when the loading frequency was 3 Hz.

Table 6.19 provides comparisons of the recovered frequencies derived from the vertical displacement and the longitudinal displacement derived from Cam 2. The loading frequencies obtained from the vertical and longitudinal displacements of the same data set were identical for each day.

Table 6.18: Experiment II: Longitudinal displacement analysis ($f_0 = 3$ Hz)

Dates	TNC	f_0 (Hz)	A (mm)	σ_{f_0} (Hz)	σ_A (mm)	$\sigma_{\hat{r}}$ (mm)
Day 1	32400	3.0672	0.50	7.44e-007	0.0012	0.16
Day 2	60050	3.0677	0.51	2.78-006	0.0019	0.17
Day 3	92450	3.0678	0.51	1.17e-006	0.0015	0.18
Day 4	154200	3.0677	0.51	6.07e-007	0.0010	0.19
Day 5	226400	3.0680	0.51	9.19e-007	0.0015	0.18
Day 7	332900	3.0683	0.51	9.79e-007	0.0014	0.18
Day 8	391000	3.0686	0.52	1.68e-006	0.0017	0.17
Day 9	486400	3.0678	0.52	1.52e-006	0.0016	0.16
Day 10	677400	3.0673	0.54	1.57e-006	0.0013	0.12
Day 11	880286	3.0672	0.54	5.17e-007	0.0010	0.12

Table 6.19: Experiment II: Comparison of the loading frequencies ($f_0 = 3$ Hz)

Dates	TNC	f_0 (Hz)-V	f_0 (Hz)-L	Δf_0 (Hz)
Day1	32400	3.0672	3.0672	0
Day2	60050	3.0677	3.0677	0
Day3	92450	3.0678	3.0678	0
Day4	154200	3.0677	3.0677	0
Day5	226400	3.0680	3.0680	0
Day7	332900	3.0683	3.0683	0
Day8	391000	3.0686	3.0686	0
Day9	486400	3.0678	3.0678	0
Day10	677400	3.0673	3.0673	0
Day11	880286	3.0672	3.0672	0

6.3.3.3 Lateral displacement analysis

Figures 6.59, 6.60 and 6.61 shows the lateral displacements of the concrete beam when the loading frequency was 3 Hz. The lateral motion trajectories with 3 Hz loading frequency were sinusoidal curve.

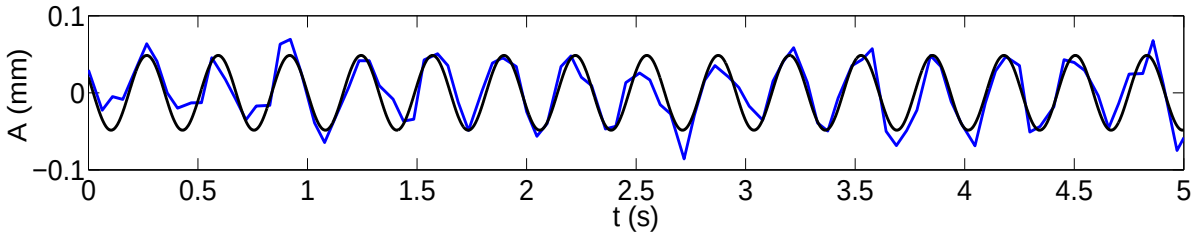

Figure 6.59: Case 1: lateral displacements ($f_0 = 3$ Hz)

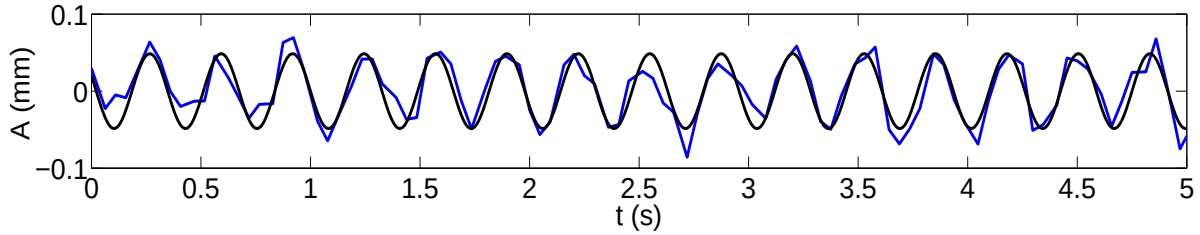

Figure 6.60: Case 2: lateral displacements ($f_0 = 3$ Hz)

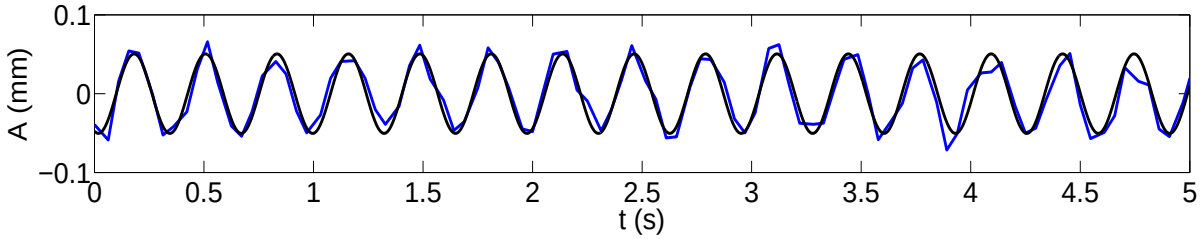

Figure 6.61: Case 3: lateral displacements ($f_0 = 3$ Hz)

Table 6.20 reports the estimated results of the lateral motion of the concrete beam when the loading frequency was 3 Hz. The estimated deflections and frequencies of the lateral motion of the concrete beam are reported. The STDs of the estimated parameters are given as well. By comparing the frequency difference from Tables 6.19 and 6.20, the maximum difference of the loading frequency is 0.0004.

Table 6.20: Experiment II: lateral displacement analysis ($f_0 = 3$ Hz)

Dates	TNC	f_0 (Hz)	A (mm)	σ_{f_0} (Hz)	σ_A (mm)	$\sigma_{\hat{r}}$ (mm)
Day 1	32400	3.0668	0.049	3.28e-004	9.12e-004	0.016
Day 2	60050	3.0678	0.049	7.28e-005	5.87e-004	0.017
Day 9	486400	3.0677	0.049	1.50e-004	7.76e-004	0.019
Day 10	677400	3.0673	0.050	6.55e-005	4.67e-004	0.013
Day 11	880286	3.0672	0.050	3.03e-005	3.50e-004	0.012

Overall, the TOF-RCs can measure three dimensional displacements including lateral, longitudinal and vertical components. In this section, the vertical, longitudinal and lateral displacements as a function of time were analyzed. So, TOF-RCs can be used to track the

3D direction motions at small deflections. But if the small deflections is less than 0.1 mm, the TOF-RCs are not sensitive to estimated the deflections and frequencies.

6.3.4 Repeatability test for Kinect range camera

In Experiment II, a Kinect (Cam 1) was used for data capture as well. The purpose of using the Kinect was to investigate its performance for deflection measurement. A repeatability test was conducted to evaluate the precision of the Kinect camera. The only SF of the Kinect LC-RC is 30 Hz.

First, 3D point cloud of the thin plate centroid at zero-load were used to assess the repeatability of the Kinect. Although thirteen thin plates were used to describe the beam deflection status, only one thin plate's deflection was analyzed for the Kinect LC-RC for simplicity. Three data sets captured at zero load state were chosen randomly. Figures 6.62, 6.63 and 6.64 show the Z-coordinate of the Plate 7 centroid from 330 frames from the Kinect.

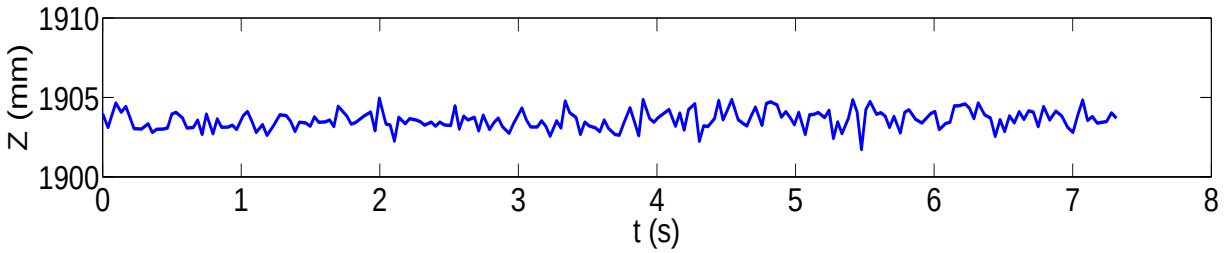

Figure 6.62: Case 1: repeatability test

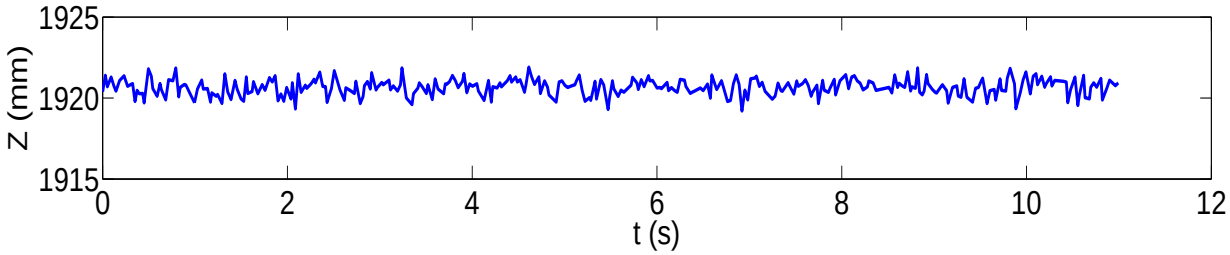

Figure 6.63: Case 2: repeatability test

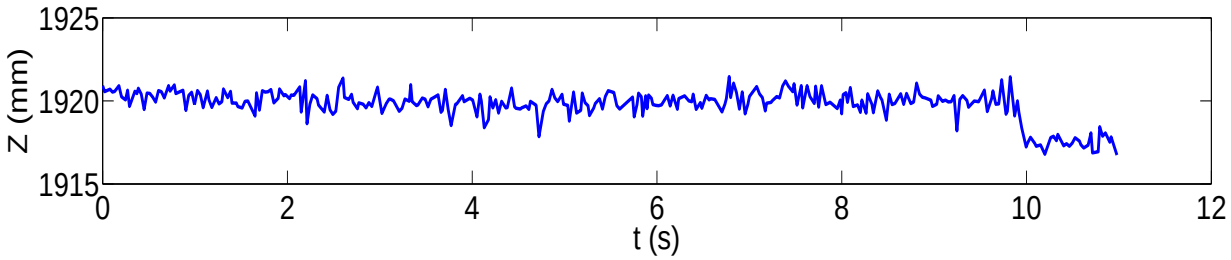

Figure 6.64: Case 3: repeatability test

Table 6.21 reports the mean values and STDs of the Z-coordinate of the thin plate centroid. Since the concrete beam was at zero-load, the mean value difference of Z-coordinates between Case 1 and Case 2 should be zero ideally. However, the mean value difference between Case 1 and Case 2 is 17.6 mm from Table 6.21. The depth values of the thin plate were fluctuated for Case 3. For example, in Figure 6.64, there a discontinuity at about 10 s which is called instability problem. The repeatability of the Kinect LC-RCs is not stable. The results have the similar trend as found by Andersen et al. (2012) who reported that even if the Kinect LC-RCs are setup in static mode, the depth value of a given object point fluctuates.

Table 6.21: Repeatability test

	Z-Mean (mm)	STD (mm)
Case 1	1903.6	0.59
Case 2	1920.7	0.52
Case 3	1919.8	0.92

6.3.5 Displacement analysis

6.3.5.1 Raw data captured by a Kinect range camera

Figures 6.65, 6.66 and 6.67 show the raw data captured during periodic loading derived from the Kinect. As can be seen, the raw measurement data are unstable. The depth measurements of the same surface have different levels. It shows the presence of an instability problem.

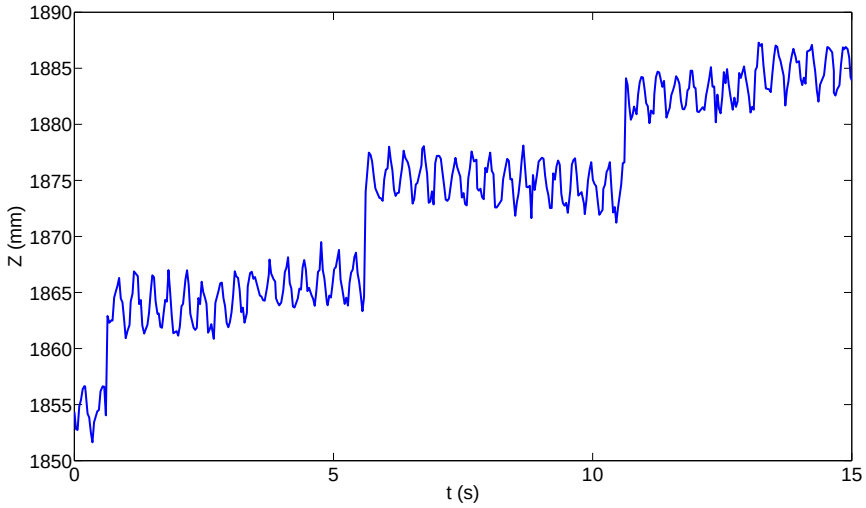

Figure 6.65: Case 1: thin plate raw trajectory with Kinect

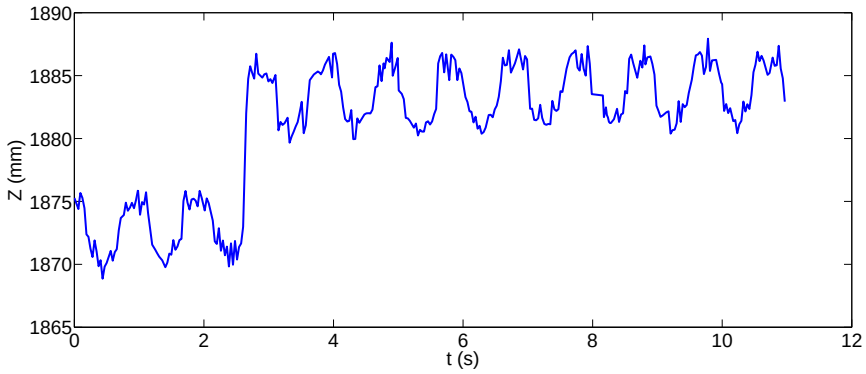

Figure 6.66: Case 2: thin plate raw trajectory with Kinect

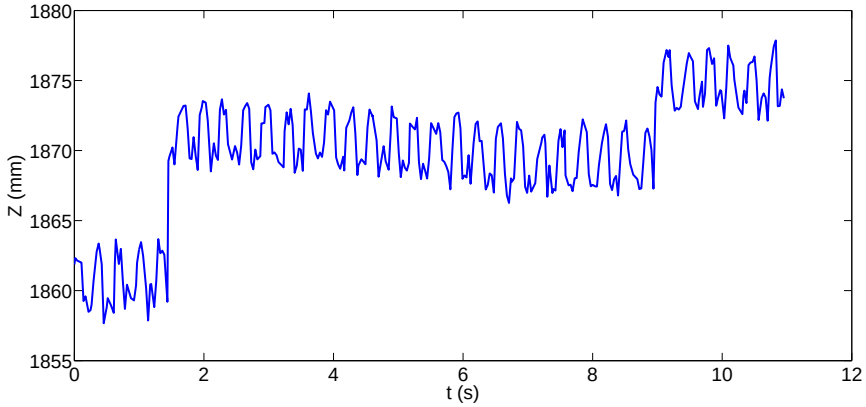

Figure 6.67: Case 3: thin plate raw trajectory with Kinect

6.3.5.2 Data analysis of a Kinect range camera: 1 Hz

The dynamic data analysis for the same thin plate (Plate 7) was conducted to assess the Kinect's performance for the concrete beam deflection measurements. If raw trajectories derived from Kinect are not stable, which is similar with Figures 6.65, 6.66 and 6.67, we cannot use these to estimate the frequencies and deflections of the concrete beam motion.

However, there were several data sets which were stable which can show that the Kinect LC-RCs have a potential ability to measure the dynamic deflections of the concrete beam. So, the frequency and the deflection estimates were conducted using stable data sets with 330 samples. Figures 6.68 and 6.69 show the recovered and raw trajectory with 1 Hz loading frequency.

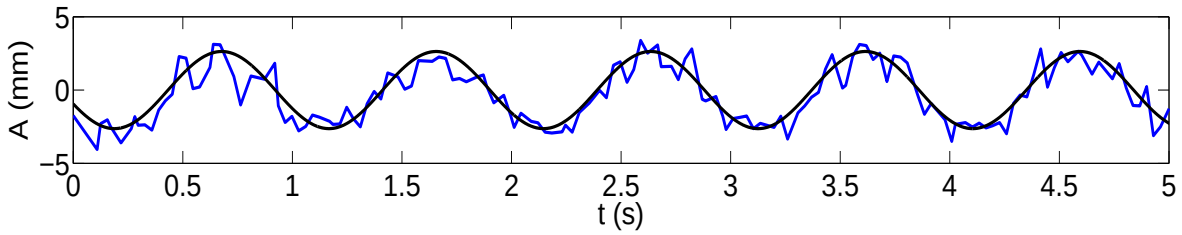

Figure 6.68: Case 1 : Thin plate raw and estimated trajectories with Kinect ($f_0 = 1$ Hz)

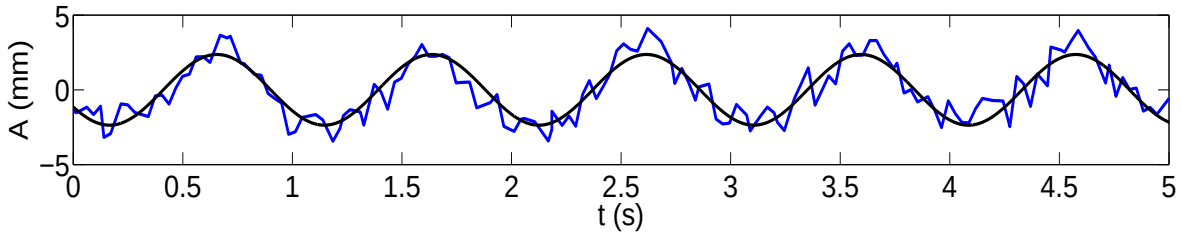

Figure 6.69: Case 2: Thin plate raw and estimated trajectories with Kinect ($f_0 = 1$ Hz)

Table 6.22 reports the estimated frequency and the deflection of the Plate 7's motion derived from the Kinect. Their absolute accuracies are also reported by calculating the

deflection and loading frequency differences between the LDS and the Kinect LC-RC. The absolute accuracies are at half-millimetre level. Table 6.23 shows the STDs of the estimated deflection and loading frequencies. The Kinect LC-RCs have an ability to obtain high measurement accuracy and precision for measuring small dynamic deflection when the loading frequency is 1 Hz but subject to the instability problem.

Table 6.22: Experiment II: Estimated frequency and deflection with Cam 1 (f_0 = 1 Hz)

Dates	TNC	f_0 (Hz)	A (mm)	f_0 (Hz)-LDS	A (mm)-LDS	Δf_0 (Hz)	ΔA(mm)
Day 8	337000	1.0213	2.63	1.0224	2.59	-0.0009	0.04
Day 9	395500	1.0207	2.36	1.0211	2.61	-0.0004	-0.25

Table 6.23: Experiment II: Standard deviations with Cam 1 (f_0 =1 Hz)

Dates	TNC	σ_{f_0} (Hz)	σ_A (mm)
Day 8	337000	0.0015	0.0768
Day 9	395500	0.0013	0.0607

6.3.5.3 Data analysis of a Kinect range camera: 3 Hz

The Kinect was used to capture when the concrete beam was subjected to periodic loads with 3 Hz motion frequency as well. Therefore, the data analysis of Kinect was conducted too in this thesis. Figures 6.70, 6.71 and 6.72 show the raw and estimated trajectories with 3 Hz loading frequency.

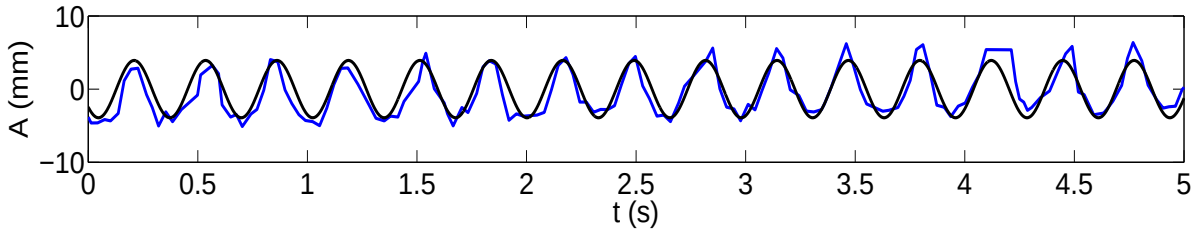

Figure 6.70: Case 1: Thin plate raw and estimated trajectories with Kinect (f_0 =3 Hz)

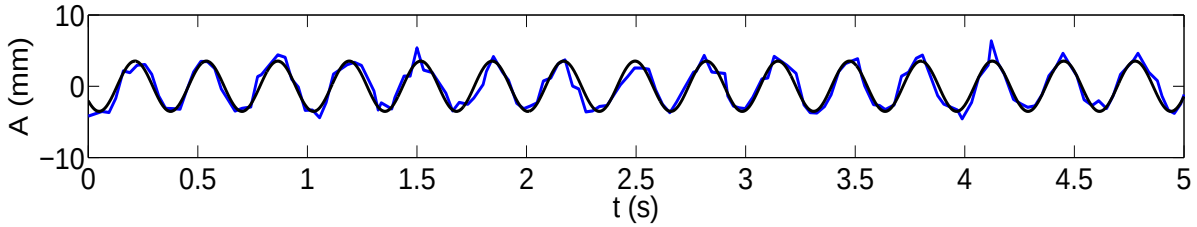

Figure 6.71: Case 2: Thin plate raw and estimated trajectories with Kinect (f_0 =3 Hz)

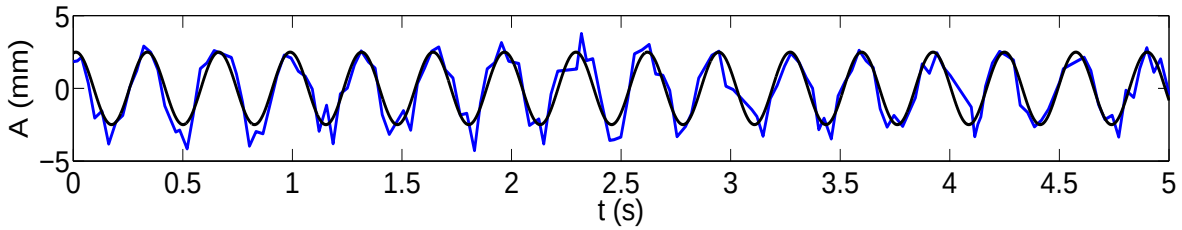

Figure 6.72: Case 3: Thin plate raw and estimated trajectories with Kinect (f_0 =3 Hz)

Table 6.24 shows the estimated frequencies and maximum deflection with the Kinect. Even though the raw data derived from Kinect are stable in this case, the absolute accuracies of the concrete deflection deflections are sensitive. Table 6.25 reports the STDs of the deflection and recovered frequencies of the dynamic concrete beam. The STDs of the estimated deflection are less than 0.2 mm. However, high estimated deflection precision does not imply high absolute accuracy. The STDs of the recovered frequencies are less than 0.01 mHz. The Kinect LC-RCs did not meet the requirements of measuring the small deflection of the dynamic concrete beam.

Table 6.24: Experiment II: Estimated frequencies and deflection with Cam 1 (f_0 =3 Hz)

Dates	TNC	f_0 (Hz)	A (mm)	f_0 (Hz)	A (mm)-LDS	Δf_0 (Hz)	ΔA (mm)
Day 7	332900	3.0682	3.92	3.0684	2.59	-0.0002	1.33
Day 8	391000	3.0669	3.52	3.0687	2.62	-0.0018	-0.90
Day 10	677400	3.0681	2.49	3.0675	2.64	0.0006	-0.15

Based on the results and analysis above, the fluctuating measurement is seemingly unpredictable and this indicated low sensitivity of Kinect LC-RCs. As a result, Kinect LC-RCs

Table 6.25: Experiment II: Standard deviations with Cam 1 (f_0 =3 Hz)

Dates	TNC	σ_{f_0} (Hz)	σ_A (mm)
Day 7	332900	0.0016	0.1293
Day 8	391000	0.0023	0.0982
Day 10	677400	9.81e-004	0.0629

can not be used for the high accuracy deflection measurement unless the instability problem is solved.

6.4 Summary

First, the simulation analysis for dynamic loading test has been conducted to simulate motion artefacts of the TOF-RCs in this chapter. Four different SFs were used for simulation data analysis. When the ideal motion frequency was 1 Hz, the motion artefacts do not affect the measurement accuracy significantly. However, 10 Hz SF is not enough to meet the accuracy requirement with 3 Hz motion frequency.

Then, this chapter has presented the quantitative and qualitative aspects of the dynamic beam deflection measurement using the different range cameras such as TOF-RCs and LC-RCs. The potential of SR4000 TOF-RCs has been investigated by deploying this sensor to detect small displacement of the concrete beam based on load control. The concrete beam deflection measurement has been made with half-millimetre accuracy and high measurement precision using SR4000 TOF-RCs with different SFs and different modulation frequencies. Higher precision measurements were obtained when the TOF-RCs were set at a higher MF. A lower SF also leads to higher measurement precision.

The concrete beam deflection measurements have been made with half-millimetre accuracy with the ideal loading frequencies 1 Hz and 3 Hz by using SR4000 TOF-RCs. The TOF-RCs are very sensitive to measure small dynamic deflection of the concrete beam. TOF-RCs can be used to perform 3D deflection measurements.

A Kinect LC-RC was also used for the dynamic deflection measurement in this section as well. Half-millimetre accuracy could be achieved sometimes. The range measurements of Kinect LC-RCs are unstable.

Chapter 7

Conclusions and recommendations

7.1 Conclusions

The thesis mainly focused on the development of new algorithms to measure the deflection of a concrete beam when it was subjected to periodic loads, which is called a fatigue load test. Three types of optical sensors were used to measure the concrete beam deflection during the fatigue loading test: SR4000 TOF-RCs, Kinect LC-RCs and LDSs. LDSs were used as the benchmark to evaluate accuracy of the RCs.

Different automatic methods to extract the thin plates for the SR4000 TOF-RCs and the Microsoft LC-RCs have been investigated in this thesis. First, the thin plate 3D point cloud was extracted automatically from the 3D point cloud of the experiment scene based on 2D and 3D image processing techniques, which was applied for the SR4000 TOF-RCs. Second, a real-time thin plate extraction system for SR4000 TOF-RCs has been developed in this work. The system was utilized to record the concrete beam dynamic deflection in real time. It paves a road for analyzing the concrete beam behaviour in real time. Third, this thesis proposed a new method with 2D and 3D image processing algorithms to automatically extract the 3D point cloud of the thin plates for the Kinect LC-RCs.

According to the concrete beam motion analysis by using the simulation data derived based on the TOF-RC measurement principle and the real data derived from the SR4000 TOF-RCs, It can be concluded that the motion artefacts do not influence the measurement accuracy significantly when loading frequency is 1 Hz and SF is 10 Hz, 20 Hz, 30 Hz or 40 Hz. However, when the loading frequency is 3 Hz, the absolute accuracies of simulated motion deflection under SFs of 20 Hz, 30 Hz and 40 Hz are of half-millimetre level which is sufficient for deflection measurements. The motion artefacts have been reduced by setting a

higher SF.

The range measurement precision of a SR4000 TOF-RC has been assessed by analyzing range measurement of the top surface of the concrete beam at zero-load state. It can be concluded that the higher modulation frequency is set, the higher range measurement precision will be obtained; the lower SF is set, the higher range measurement precision will be achieved.

The results from the real data from Experiment I have indicated that the amplitudes of the periodic motion can be recovered with half-millimetre accuracy when the 3 Hz target motion is sampled at 20 Hz, 30 Hz and 40 Hz with 31 MHz modulation frequency. However, When the 1 Hz target motion is sampled at 10, 20, 30 and 40 Hz with 31 MHz modulation frequency, the concrete beam deflection can be recovered with half-millimetre accuracy. When the modulation frequency is 29 MHz, the best SF is 20 Hz to keep the error under half-millimetre for 3 Hz loading frequency. However, for 1Hz loading frequency, the SFs should be 20 Hz to keep the measurement error under the half-millimetre. In conclusion, the use of TOF-RC in dynamic vertical deflection measurements in this thesis has shown that even though the coarse absolute accuracy range camera with ± 10 mm, can achieve half-millimetre accuracy for dynamic deflection measurement.

By analyzing the vertical deflection of the concrete beam during Experiment I, the best SF is 20 Hz, in order to keep the absolute accuracy under the half-millimetre. Therefore, in Experiment II, 3D motion trajectories of the concrete beam subjected to 1 Hz and 3 Hz periodic loads have been measured using the TOF-RC when the SF was set at 20 Hz. Based on the results and analysis from Experiment II, first, the TOF-RC can be used to track the properties of the concrete beam over time. Second, the TOF-RCs have the ability to track the 3D motion trajectories. The deflections and frequencies of the 3D motion of the concrete beam can be recovered at a high level accuracy. The TOF-RCs in the vertical and longitudinal displacement analysis have a better performance than the lateral displacement

analysis. So, the use of TOF-RC in dynamic vertical, longitudinal and lateral displacements has shown that the TOF-RC has the capability of measurement 3D deflections. The TOF-RCs have the capability to estimate the amplitudes of the target motion with small deflection. Third, by analyzing the dynamic motion amplitudes of the concrete beam for all thin plates along the length of the concrete beam has shown that wide coverage is a selling feature of TOF-RCs.

The vertical deflection was also measured using a Kinect light coded range camera. According to the results and analysis from Experiment II, the raw data derived from the Kinect LC-RCs were unstable. The instability problem of the Kinect LC-RCs was unpredictable. Therefore, It can be concluded that the depth measurements of Kinect are not stable, which is not sufficient to meet the half-millimetre accuracy for the deflection measurement. Additionally, the unstable and unpredictable problem of the raw measurement derived from the Kinect LC-RCs indicates that the Kinect LC-RCs have low measurement precision. As a result, the Kinect LC-RCs can not be used for high accuracy deflection measurement unless the instability problem is solved.

7.2 Recommendations

In this thesis, most of the analysis focuses on the thin plates since the top surface of the concrete beam were occluded by the spread beam. However, the top surface of the concrete beam is still very useful to analyze the beam deflection through reconstructing the whole top surface of the concrete beam. However, due to the limited field of view of the range cameras, multiple range cameras should be used to cover the complete top surface of the concrete beam. Therefore, the registration of multi-camera data is a promising for future work and then the use of the concrete beam itself for analyzing the deflection is another future work. The TOF-RC is capable of the surface reconstruction with acquired 3D point cloud. The acquired 3D point cloud can provide highly accurate surface models of the deflection objects.

In addition, the top surface of the concrete beam can be recovered by using the mathematical model of the beam deflection derived in Gordon and Lichti (2007).

In Experiment II, real time extraction of the thin plates allowed detection of the concrete beam deflection behaviour in real time. During the experiment, the centroids of the thin plates were recorded in real time. However this is not real time monitoring of concrete beam deflection. The Kalman filter extends the concept of least-squares to contain the knowledge of how the state vector behaves in time. In order to monitor the concrete beam deflection in real time, implementation of a Kalman filter is necessary in future work.

In Experiment II, a Kinect LC-RC was also used to capture the dynamic concrete beam data which were processed after the experiment. The Kinect LC-RCs include RGB images and depth images. However, since the relative orientation of the RGB image and depth image was not estimated, the depth image was just used to isolate the thin plates. Therefore, the relative orientation of the RGB and depth images is a bridge of two cameras, which is useful to segment the thin plate with 2D and 3D image process algorithm. Calculating the relative orientation of the two cameras is necessary in future work. In addition, the instability problem of the raw measurement of the Kinect LCs should be solved.

References

Andersen, M., T. Jensen, P. Lisouski, A. Mortensen, M. Hansen, T. Gregersen, and P. Ahrendt (2012, February). Kinect depth sensor evaluation for computer vision applications. Technical Report ECE-TR-6, Aarhus University.

Blackledge, J. (2005). *Digital image processing mathematical and computational methods*. Chichester, West Sussex: Horwood.

Bostelman, R. and J. Albus (2007). A multipurpose robotic wheelchair and rehabilitation device for the home. In *Proceedings of the IEEE International Conference on Intelligent Robots and Systems*, San Diego, California, USA, pp. 3348–3353.

Bostelman, R., T. Hong, R. Madhavan, and B. Weiss (2005). 3D range imaging for urban search and rescue robotics research. In *IEEE International Conference On System Safety, Security and Rescue Robotics*, Gaithersburg, MD, USA, pp. 164–169.

Cheney, W. and D. Kincaid (2007). *Numerical Mathematics and Computing*. Belmont: Thomson Brooks/Cole.

Chiabrando, F., R. Chiabrando, D. Piatti, and F. Rinaudo (2009). Sensors for 3d imaging: metric evaluation and calibration of a ccd/cmos time-of-flight camera. *Sensors 9*(12), 10080–10096.

Chow, J., K. D. Ang, D. D. Lichti, and W. F. Teskey (2012). Performance analysis of a low-cost triangulation-based 3D camera: Microsoft kinect system. In *International Archieves of the Photogrammetry, Remote Sensing and Spatial Information Science, XXII ISPRS Congress, 2012*, Volume XXXIX-B5, Melbourne, Australia, pp. 239–244.

Detchev, I., A. Habib, and M. El-Badry (2012). Image-based deformation monitoring of statically and dynamically loaded beams. In *International Archieves of the Photogrammetry,*

Remote Sensing and Spatial Information Science, XXII ISPRS Congress, 2012, Volume XXXIX-B5, Melbourne, Australia, pp. 6.

Dorrington, A., J. Godbaz, M. Cree, A. Payne, and L. Streeter (2011). Separating true range measurements from multi-path and scattering interference in commercial range cameras. In *Proc. of SPIE-IS & T Electronic Imaging*, Volume 7864, California, USA, pp. 1–10.

Fitzgibbon, A., M. Pilu, and B. Fisher (1999). Direct least square fitting of ellipses. *IEEE transactions on pattern analysis and machine intelligence 21*(5), 476–480.

Foix, S., G. Alenya, and C. Torras (2011). Lock-in time-of-flight (tof) cameraaas: a survey. *IEEE Sensors Journal 11*(3), 1–11.

Fraser, C. and B. Riedel (2000). Monitoring the thermal deformation of steel beams via vision metrology. *ISPRS Journal of Photogrammetry & Remote Sensing 55*(4), 1–10.

Freedman, B., A. Shpunt, M. Machline, and Y. Arieli (2012, 04). Depth mapping using projected patterns.

Fuchs, S. and G. Hirzinger (2008). Extrinsic and depth calibration of ToF-cameras. In *Computer Vision and Pattern Recognition, 2008*, Anchorage, USA, pp. 1–6.

Gonsalves, R. and J. Teizer (2009). Human motion analysis using 3d range imaging technology. In *26th Internation Symposium on Automation and Robotics in Construction*, Giorgia, USA, pp. 76–85.

Gonzalez, R. and R. Woods (2008). *Digital image processing*. Upper Saddle River, NJ, USA: Prentice Hall.

Gordon, S. and D. Lichti (2007). Modeling terrestrial laser scanner data for precise structural deformation measurement. *ASCE Journal of Surveying Engineering 133*(2), 72–80.

Heffernan, P. J. and M. A. Erki (2004). Fatigue behavior of reinforced concrete beams strengthened with carbon fiber reinforced plastic laminates. *Journal of Composites for Construction 8*(2), 132–140.

Herrera, C., J. Kannala, and J. Heikkila (2011). Accurate and practical calibration of a depth and color camera pair. In *14th International Conference on Computer Analysis of Images and Patterns*, Seville, Spain, pp. 437–445.

Jamtsho, S. (2010). Geometric modelling of 3D range cameras and their application for structural deformation measurement. Master's thesis, University of Calgary, Calgary, Canada.

Jamtsho, S. and D. Lichti (2010). Modeling scattering distortion of 3d range camera. In *International Archives of the Photogrammetry, Remote Sensing and Spatial Information Sciences*, Volume XXXVIII, Newcastle, UK, pp. 299–304.

Jia, W., W. Yi, J. Saniie, and E. Oruklu (2012). 3d image reconstruction and human body tracking using stereo vision and Kinect technology. In *Electro/Information Technology (EIT), 2012*, Chicago, USA, pp. 1–4.

Kahlmann, T., H. Remondino, and H. Ingensand (2006). Calibration for increased accuracy of the range imaging camera swissranger. *Remote Sensing and Spatial Information Sciences 36*(5), 136–141.

Khoshelham, K. and S. Elberink (2012). Accuracy and resolution of kinect depth data for indoor mapping applications. *Sensors 12*(2), 1437–1454.

Klette, R., K. Schluns, and A. Koschan (1998). *Computer vision there-dimensional data from images*. Singapore: Springer.

Lahamy, H. and D. Lichti (2010). Real-time hand gesture recognition using range cameras.

In *Internation Archives of Photogrammetry, Remote Sensing and Spatial Information Sciences*, Volume XXXVII, pp. 54–59.

Lahamy, H. and D. Lichti (2012). Towards real-time and rotation-invariant american sign language alphabet recongnition using a range camera. *Sensors 12*(11), 14416–14441.

Lange, R. (2000). *3D time-of-flight distance measurement with solid-state image sensors in CMOS/CCD-technology*. Ph. D. thesis, University of Siegen, Germany.

Lange, R. and P. Seitz (2001). Solid-state time-of-flight range camera. *IEEE Journal of Quantum Electronics 37*(3), 390–397.

Lange, R., P. Seitz, A. Biber, and S. Lauxtermann (2000). Demodulation pixels in ccd and cmos technologies for time-of-flight ranging. In *Sensors, Cameras and Systems for Scientific/Industrial Applications II, Proc. SPIE*, Volume 3965, San Jose, USA, pp. 1–12.

Li, Y. (2012). Hand gesture recognition using Kinect. In *Software Engineering and Service Science (ICSESS), 2012*, Beijing, China, pp. 196–199.

Li, Z. and R. Jarvis (2009). Real time hand gesture recognition using a range camera. In *Australian Conferenec on Robotics and Automation (ACRA)*, Sydney, Australia, pp. 1–7.

Lichti, D., S. Jamtsho, S. El-Halawany, H. Lahamy, J. Chow, T. Chang, and M. El-Badry (2012). Structural deflection measurement with a range camera. *Journal of Surveying Engineering 183*(2), 66–76.

Lichti, D. and C. Kim (2011). A comparsion of three geometric self-calibration methods for range cameras. *Remote Sensing 3*(5), 1014–1028.

Lichti, D., C. Kim, and S. Jamtsho (2010). An integrated bundle adjustment approach to range camera geometric self-calibration. *ISPRS Journal of Photogrammetry & Remote Sensing 65*(4), 360–368.

Lichti, D., X. Qi, and T. Ahmed (2012). Range camera self-calibration with scattering compensation. *ISPRS Journal of Photogrammetry & Remote Sensing 74*(0), 101–109.

Lindner, M. and A. Kolb (2006). Calibration of the intensity-related distance error of the pmd tof camera. In *Proceedings of the SPIE on Intelligent Robots and Computer Vision*, Volume XXV, Boston, USA.

Lindner, M. and A. Kolb (2009). Compensation of motion artifacts for time-of-flight cameras. In *Proc, Dynamic 3D Vision Workshop*, Volume 5742, pp. 16–27.

Lindner, M., I. Schiller, A. Kolb, and R. Koch (2010). Time-of-flight sensor calibration for accurate range sensing. *Computer Vision and Image Understanding 114*(12), 1318–1328.

Lottner, O., A. Sluiter, K. Hartmann, and W. Weihs (2007). Movement artefacts in range images of time-of-flight cameras. In *Signals, Circuits and Systems, 2007. ISSCS 2007. International Symposium on*, Volume 1, pp. 1 –4.

Maas, H. and U. Hampel (2006). Photogrammetric techniques in civil engineering material testing and structure monitoring. *Photogrammetric Engineering and Remote Sensing 72*(1), 39–45.

MESA-Imaging (2012). Sr 4000 user manual. `www.mesa-imaging.ch/dlm.php?fname...CD/SR4000_Manual.pdf`. [Online; accessed 06-June-2012].

Mutto, C., P. Zanuttigh, and G. Cortelazzo (2010). *Time-of-flight cameras and Microsoft Kinect*. New York, Heidelberg, Dordrecht and London: Springer.

Otsu, N. (1979). A threshold selection method from gray-level histograms. *IEEE Transactions on Systems, Man, and Cybernetics 9*(1), 62–66.

Papakonstantinou, C. G., M. F. Petrou, and K. A. Harries (2001). Fatigue behavior of RC beams strengthened with GFRP sheets. *Journal of Composites for Construction 74*(5), 246–253.

Park, H. and H. Lee (2007). A new approach for health monitoring of structures-terrestrial laser scanning. *Computer-Aided Civil and Infrastructure Engineering 22*(1), 19–30.

Piatti, D. and F. Rinaudo (2012). SR-4000 and CamCube3.0 time of flight (ToF) cameras: tests and comparison. *Remote Sensing 4*(4), 1069–1089.

Press, H., A. Teukolsky, T. Vetterling, and P. Flannery (1992). *Numerical Recipes in C*. New York: Cambridge University.

Primesense (2012). Primesense, Ltd. `http://www.primesensr.com`. [Online; accessed 06-Oct-2012].

Qi, X. and D. Lichti (2012a). Dynamic concrete beam deformation measurement with 3d range cameras. In *International Archieves of the Photogrammetry, Remote Sensing and Spatial Information Science, XXII ISPRS Congress, 2012*, Volume XXXIX-B5, Melbourne, Australia, pp. 239–244.

Qi, X. and D. Lichti (2012b). Monitoring dynamic concrete beam deformation with range cameras. In *FIG Working Week 2012, Knowing to Manage the Territory, Protect the Environment, Evaluate the Cultural Heritage*, Rome, Italy, pp. 1–13.

Rabbani, T., F. van den Heuvel, and G. Vosselman (2006). Segmentation of point clouds using smoothness constraint. In *ISPRS Commission V Synposium 'Image Engineering and Vision Metrology*, Volume XXXVI, Dresden, Germany.

Ray, S. and J. Teizer (2012). Real time construction worker posture analysis for ergonomics training. *Advanced Engineering Informatics 26*(2), 493–455.

Rohs, M. (2004). Real-world interaction with camera phones. *Lecture Notes in Computer Science*, 74–89.

Ronnholm, P., M. Nuikka, A. Suominen, P. Salo, H. Hyypp, P. Pntinen, H. Haggrn, M. Vermeer, J. Puttonen, H. Hirsi, A. Kukko, H. Kaartinen, J. Hyypp, and A. Jaakkola (2009). Comparsion of measurement techniques and static theory applied to concrete beam deformation. *Photogrammetric Record 24*(128), 351–371.

Shahbazi, M., S. homayouni, M. Saadatseresht, and M. Sattari (2011). Range camera self-calibration based on integrated bundle adjustment via joint setup with a 2d digital camera. *Sensors 11*(9), 8721–8740.

Whiteman, T., D. Lichti, and I. Chandler (2002). Measurement of deflections in concrete beams by close-range digital photogrammetry. In *Proceedings of Joint International Symposium on Geospatial Theory, Processing and Applications*, Ottawa, Canada. CD-ROM.

Xia, L., C. C. Chen, and J. Aggarwal (2011). Human detection using depth information by Kinect. In *International Workshop on Human Activity Understanding from 3D Data in conjunction with CVPR*, Colorado, USA, pp. 15–22.

Ye, J., G. Fu, and U. Poudel (2011). Edge-based close-range digital photogrammetry structural deformation measurement. *Journal of Engineering Mechanics 137*(7), 475–483.